Advancing High-Resolution Measurement Systems for Ocean Engineering

PhD Thesis

Yi Huang

Department of Naval Architecture, Ocean and MarineDelay or removal of aneurysm formation Engineering

University of Strathclyde, Glasgow

August 29, 2025

This thesis is the result of the author's original research. It has been composed by the author and has not been previously submitted for examination which has led to the award of a degree.

The copyright of this thesis belongs to the author under the terms of the United Kingdom Copyright Acts as qualified by University of Strathclyde Regulation 3.50. Due acknowledgement must always be made of the use of any material contained in, or derived from, this thesis.

Abstract

Water waves are a ubiquitous and profoundly complex natural phenomenon, manifesting in diverse forms across rivers, coastal regions, and the open ocean, as well as in engineered environments such as wave flumes and offshore structures. Their pervasive presence underpins a multitude of scientific, engineering, and everyday phenomena, making them a subject of enduring fascination and practical importance. Even on a smaller scale, the gentle propagation of ripples across a pond or the rhythmic oscillations within a home aquarium serve as reminders of the intricate interplay between gravitational forces, fluid motion, and boundary interactions.

However, water waves do not exist in isolation. Their behaviour is profoundly influenced by interactions with currents, wind fields, and submerged or floating structures, resulting in a rich diversity of wave forms, frequencies, and amplitudes. This complexity necessitates a nuanced understanding of fluid-structure interactions, which is critical for a wide range of applications. In maritime operations, for example, the safety and performance of vessels depend on accurate predictions of wave-induced loads and motions. Similarly, in coastal ecology, wave-driven sediment transport and hydrodynamic exchange processes are fundamental to habitat formation and ecosystem resilience. In the realm of offshore renewable energy, the coupling between waves and energy-harvesting devices directly impacts power generation efficiency and structural survivability. To address these challenges, researchers have developed a plethora of wave measurement and monitoring techniques, spanning from laboratory-scale experiments to open-ocean deployments. Yet, despite these advancements, many existing methods struggle to capture fine-grained, multi-dimensional data—essential for contemporary engineering tasks such as optimising wave energy converters, designing wave-manipulating metamaterials, or validating numerical models.

It is within this context that this thesis presents the development, demonstration, and application of a high-resolution stereo-vision system for measuring water waves and analysing wave–structure interactions in controlled laboratory environments. A comprehensive literature review is first undertaken, examining both intrusive and non-intrusive wave measurement techniques—-from conventional resistance probes and acoustic sensors to advanced optical methods–while identifying persistent limitations in spatial resolution and the potential for disturbing the wave field. To address these shortcomings, the research introduces a novel camera-based

methodology that leverages triangulation and Direct Linear Transformation (DLT) to reconstruct three-dimensional free-surface elevations with exceptional precision. Particular emphasis is placed on mitigating reflective artefacts and ensuring rigorous optical calibration, thereby enhancing the reliability and accuracy of the measurements. Through this work, the thesis aims to contribute a robust and versatile tool for advancing the study of water waves, with implications for both fundamental research and applied ocean engineering.

Experimental investigations are conducted across desktop-scale and moderate-sized wave flumes, demonstrating the system's capability to capture intricate hydrodynamic phenomena with high fidelity. Tests involving metamaterial structures reveal the system's ability to detect subtle distortions or enhancements in wave amplitude and phase, providing insights into wave manipulation mechanisms. Observations of a wave energy converter's motion further validate the stereo-vision system's reliability, with results corroborated by comparisons to standard instrumentation, including commercial motion-tracking devices. Comparative analyses with conventional tools, such as calibration targets, underscore the versatility, precision, and robustness of the proposed methodology.

While these experiments are confined to laboratory settings, the findings suggest that further advancements could enable the system's deployment in more challenging environments, such as offshore testing sites or real-time monitoring of vessel wakes. Additionally, integrating the system with digital twins or numerical solvers could facilitate detailed comparisons between measured wave fields and advanced simulation outputs, thereby refining both experimental designs and theoretical models. Future work may focus on enhancing data handling capabilities, particularly through real-time image processing using dedicated hardware, as well as refining camera calibration techniques under variable lighting conditions. By providing a non-intrusive, precise, and adaptable means of capturing water surface dynamics as well as tracking moving objects, this thesis lays a robust foundation for more informed research and innovation across coastal, marine, and offshore engineering disciplines.

Contents

List of Figures

List of Tables

Acknowledgements

Upon the end of my PhD years, it's important to look back and appreciate those who offer help and guidance along the way.

Heartfelt gratitude is extended to Dr Laibing Jia for unwavering guidance and scholarly insight, which proved central to the direction of this doctoral research. Equal appreciation is owed to Dr Saishuai Dai, whose constructive advice and leadership at the Kelvin Hydrodynamics Laboratory established productive avenues for experimental investigation. Sincere thanks are also conveyed to Dr Weichao Shi for providing the first research-assistant opportunity and for granting the resources and laboratory time necessary to conduct an inaugural particle-image-velocimetry experiment.

Acknowledgment is directed to the Department of Naval Architecture, Ocean & Marine Engineering and the University of Strathclyde for cultivating a supportive academic environment and providing essential resources. Further recognition is given to Dr. Guangwei Zhao, Mr. Wenxuan Xia, Dr. Yihan Liu, Dr. Momchil Terziev, and Dr. Roberto Ravenna, whose companionship and readiness to share expertise enriched the research process.

A special tribute is paid to Alice Li for the steadfast encouragement that underpinned this effort. Her kindness and belief in the research served as a vital source of endurance. In addition, sincere thanks are reserved for Mr. Steven Black, Mr. Grant Dunning, Mr. Bill Wright, and Mr. Martin Dowling of the Kelvin Hydrodynamic staff, whose technical assistance proved indispensable in finalizing the experimental work. Their dedication and collective efforts made a profound impact on the outcomes of this study.

Chapter 1

Introduction

Water waves, from tranquil shores to turbulent seas, are central to coastal engineering, environmental science, and maritime operations. Their dynamic behaviour and interactions with structures, floating or submerged pose significant challenges, from predicting wave forces and managing coastal erosion to designing floating infrastructure and tracking marine debris. Despite their ubiquity, the complexity and sensitivity of waves make them difficult to observe and analyse with precision. Although diverse wave measurement techniques have been developed, persistent limitations in spatial resolution, measurement coverage, and invasiveness significantly restrict their effectiveness in complex marine environments. This thesis addresses these challenges by advancing the precision and scope of water wave measurement, as outlined in the following sections.

1.1 Motivation and Challenge

Measuring water wave elevation with sufficient resolution and accuracy is crucial in ocean engineering research. It enables researchers to study water waves under various forms of external effect, including, but not limited to, floating structures, underwater structures, and self-propelled vessels.

Despite the availability of various water surface measurement techniques—both intrusive and non-intrusive—limitations persist when high spatial and temporal resolution are required. Intrusive methods, such as resistance-type wave gauges, may disturb natural wave patterns and potentially alter the phenomena being studied. Although these techniques typically yield precise data, their impact on the wave environment may render them unsuitable for certain research applications. In contrast, non-intrusive methods, including ultrasonic wave probes and slope-measuring laser water wave gauges, can measure wave elevations without physical contact. However, these methods may experience limitations in resolution and accuracy due to environmental factors, such as water surface reflections and blind zones, as well as equipment-related issues, including calibration and maintenance challenges. Additionally, non-intrusive

techniques often necessitate complex data processing to interpret measurements accurately, introducing another potential source of error (Lange et al. (1982); Gomit et al. (2022)).

Detailed measurements of water wave with high accuracy and resolution allow for a deeper understanding of wave dynamics and more crucially, it's interactions with structures in the applications of wave energy convertors deployment, coastal erosion prevention, or marine infrastructure monitoring and assessment. Such understanding could pave the way for further optimization of wave energy or coastal protection systems, more quantitative prediction of sediment transport and more robust validation of computational fluid dynamics models.

While the interest and application in measuring wave elevation with high resolution and accuracy are great, several challenges persist in this field especially when it comes to recreate a whole water surface instead of using point-based intrusive/non-intrusive equipment.

The challenges one faced when developing a comprehensive high accuracy stereo wave measurement system could be summarized from a few perspectives.

On the technical front, developing systems that maintain precision in harsh marine environments while also ensuring accurate camera positioning and calibration is difficult. Many methods assume an ideal camera distance, but practical scenarios often lead to calibration errors, particularly in large-scale applications (Jähne et al. (1994); Zhang and Cox (1994); Tropea et al. (2007)).

When it comes to environmental factors, highly variables in wave dynamics due to other environmental factors such as temperature and water depth can complicate data collection and analysis. The exceptionally low reflection rate for light of the water surface can make it difficult to capture and then extract water wave features, especially when dealing with light attenuation and reflection issues(Cox (1958); Keller and Gotwols (1983); Moisy et al. (2009)).

Regarding instrumentation, designing and fabricating measurement instruments that are both reliable and cost-effective, while ensuring that calibration processes are thorough and adaptable to different measurement scenarios, including the use of stereo cameras. The calibration of stereo-vision systems is complex, especially in large-scale or field measurements where traditional calibration techniques are impractical(Chatellier et al. (2013); Cox (1958)).

For data analysis, processing large volumes of high-resolution data is computationally intensive and requires advanced hardware and compatible software. Methods that estimate the surface gradient and integrate it to obtain the elevation face challenges in accurately measuring changes in mean elevation or waves with wavelengths larger than the field of view. The integration step can lead to inaccuracies if the reference height is unknown or if the surface features change dynamically (Moisy et al. (2009); Fouras et al. (2008)).

Last but not least, it's of great significant to ensure compatibility and integration with existing measurement framework, especially while overcoming challenges related to data standardization and interoperability between different systems and technologies. The spatial resolution of an optical method is influenced by the camera resolution, field of view, and the specific measurement technique used (Chatellier et al. (2013)).

Despite these challenges, advancements in measurement techniques continue to improve our ability to capture accurate wave elevation data. The development of new methodologies that combine the strengths of various existing methods while mitigating their weaknesses is crucial.

In summary, despite notable progress in the domain of water wave measurement, numerous technical, environmental, instrumentation, analytical, and integration-related challenges persist, particularly when aiming for comprehensive, high-resolution surface reconstruction using stereo camera systems. The need for improved precision, adaptability, and reliability in wave elevation measurement methodologies remains critical, particularly for accurately capturing complex wave-structure interactions in diverse marine environments. Addressing these challenges requires the development and refinement of advanced measurement techniques that effectively integrate state-of-the-art optical and computational technologies. The following chapters of this thesis undertake a detailed exploration of these advancements, with the objective of overcoming current limitations and significantly enhancing our understanding and management of wave dynamics and their impacts.

1.2 Literature Review

Within the following section, a deeper examination of the current state of the art in water wave measurement techniques as well as a basic principles of shallow water theory is undertaken. Established and emerging experimental methods for capturing free-surface dynamics are critically assessed, alongside the theoretical foundation in the analysis of shallow water flows. This synthesis lays the groundwork for understanding the experimental and theoretical challenges that underpin subsequent investigations into wave–structure interactions applications.

1.2.1 Freesurface Measurement

Within the scope of this thesis, the freesurface is defined as the interface between air and a liquid (water) while freesurface measurement is described as the measurement of the shape, either heights or slop of the water surface.

Measuring the free surface creates a time history of physical properties for a point or region of investigation on the free surface. Since the main interest of this thesis is water wave-structure

interaction on the free-surface formation, the main physical property measured would be the wave heights/surface elevation.

a. Intrusive Methods for Freesurface Measurement

Intrusive techniques acquire free-surface elevations by inserting sensors directly into the flow.

- **Point-Gauge Probe**: which visually measured the water surface height from the instrument scale (shown in Fig. 1.1 (c)).

- **Pressure-Based Manometer**: A flush-mounted or submerged pressure transducer records hydrostatic and dynamic pressure, from which depth is inferred. Calibration must correct for velocity and turbulence effects, yet the sensor's compact form minimises flow obstruction (Fig. 1.1 (b)).

- **Conductance (Resistance-Type) Wave Probe**: which measures electrical output—resistance for the former, capacitance for the latter—changes in response to the wetted portion of the probe, enabling an estimate of wave height (shown in Fig. 1.1 (a));
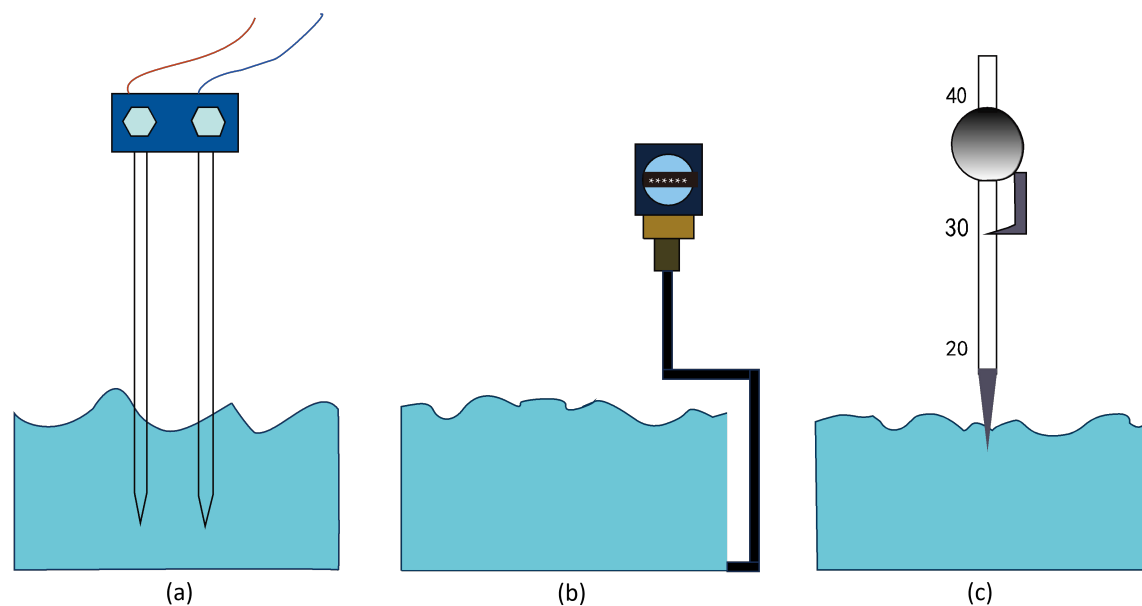
Figure 1.1: Illustration of Measuring principle of the three **intrusive** wave measuring methods with (a) resistance type wave probe, (b)submerged pressure sensor and (c) point gauge Rak et al. (2023)

A simpler but more manual option is the *point gauge probe*. This device lowers a needle or pointer until it just touches the water surface, allowing a visual reading on a graduated scale. Point gauges are commonly used in contexts such as measuring head losses in sewer junctions, where flows may be relatively slow or can be interrupted for measurement. Although inexpensive, they lack temporal resolution and can still disrupt small-scale wave behaviour.

Another intrusive approach uses *pressure-based manometers*, where small sensors are installed (often flush with the tank floor) to measure local hydrostatic and dynamic pressure. By linking water depth to changes in pressure, these devices estimate the free-surface profile without requiring vertical rods or wires penetrating the flow. Nonetheless, interpretation can be complicated by local velocity effects, turbulence, or fluid density fluctuations, so careful calibration is essential. In highly unsteady wave conditions, the pressure signal may only partially capture short-lived free-surface phenomena.

Of the various intrusive techniques for measuring free-surface elevations, *conductance* and *capacitance wave probes* are especially common in engineering laboratories. Both rely on submerged sensing elements to detect local changes in wave height. In a conductance (or resistance-type) probe, a high-frequency square-wave voltage is passed between two stainless-steel rods. The electrical current through the wetted region translates into a voltage reading proportional to wave elevation, assuming the rods remain consistently within their intended immersion depth. Although these probes are relatively simple to construct and calibrate, they can disturb the local flow when deployed in sensitive experiments, and multiple units may be needed to obtain spatial coverage.

Capacitance probes infer free-surface height by tracking changes in the dielectric properties of water: an insulated rod or wire acts as one plate of a capacitor, and variations in water immersion alter the total capacitance. Despite some similarity to conductance devices (notably in the single-point measurement principle), capacitance probes also share the drawback of intrusive mounting and only limited multi-point data gathering.

Intrusive devices, such as conductance (or resistance) wave probes, capacitance wave probes, pressure-based manometers, and point gauges, have featured prominently in laboratory free-surface measurements for many years, owing to their straightforward design and ease of fabrication. Conductance and capacitance probes both rely on a submerged sensing element—rods for conductance, an insulated wire or rod for capacitance—to convert the wetted length into an electrical signal representing wave height. Pressure-based manometers, in contrast, measure local hydrostatic or dynamic pressure at a submerged location and infer the free-surface elevation from that reading, though velocity effects and turbulence can complicate the relationship between pressure and water level. Point gauges offer a simple, visually read instrument, often used in slower-flow situations such as determining head losses in sewer junctions, where the operator lowers a pointer until it just contacts the surface.

All these methods reliably capture free-surface levels at specific points, yet they invariably introduce physical components into the wave field, potentially altering delicate wave phenomena.

Researchers must also position multiple sensors with care to prevent interference, an arrangement that becomes cumbersome when attempting high-resolution or large-area mapping. Although multi-point arrays are possible, the data density achieved still falls short of what modern non-intrusive approaches, for example optical or acoustic systems, can provide. Mechanical contact with the fluid in any of these intrusive methods risks distorting or damping local wave motion, making them less suitable for sensitive studies such as fine-scale wake flows or rapidly evolving wave fields.

Limitations of this nature motivate the continuing development of more comprehensive, non-intrusive wave measurement solutions. Approaches based on optical imaging or acoustic sensing can often capture richer detail without disturbing the fluid domain, delivering better spatial resolution and higher-frequency data at the cost of more advanced calibration requirements and potentially higher initial costs. Nonetheless, intrusive techniques remain valuable for many laboratory contexts where simple operation, robust calibration, and cost-effectiveness are paramount, and where the wave phenomena of interest are not unduly affected by the presence of small probes or pressure sensors.

b. Non-intrusive Methods for Freesurface Measurement

In addition to intrusive means of measuring water wave elevation, there are also numerous non-intrusive means of either point or grid measurement.

- **Ultrasonic Sensors** which sends out acoustic pulses to measure surface elevation via acoustic echo timing.

- **Wave Slope Optical Wave Gauges (WSOPG)** which determines wave slope using laser refraction at the air-water interface.

- **Wave Acquisition Stereo System (WASS)** which reconstructs 3D wave fields via synchronized camera arrays for open water during field tests.

Ultrasonic sensors, also known as acoustic displacement meters, shown in Fig.1.2a), work by detecting frequency changes in emitted sound waves as they move along a flow path. Flow velocity is calculated based on the speed of sound, which is approximately 1500 m/s in water. Ultrasonic sensors offer a frequency response of up to a few hundred Hz, compatable with even intrusive measurement device (Rodriguez et al. (1999)), but they are more susceptible to contamination from air or particles, making them more suitable for controlled laboratory conditions. However, their spatial resolution is limited due to their single-point measurement method and the size of the signal spot (instead of measuring a single dot, it's ultrasonic beam
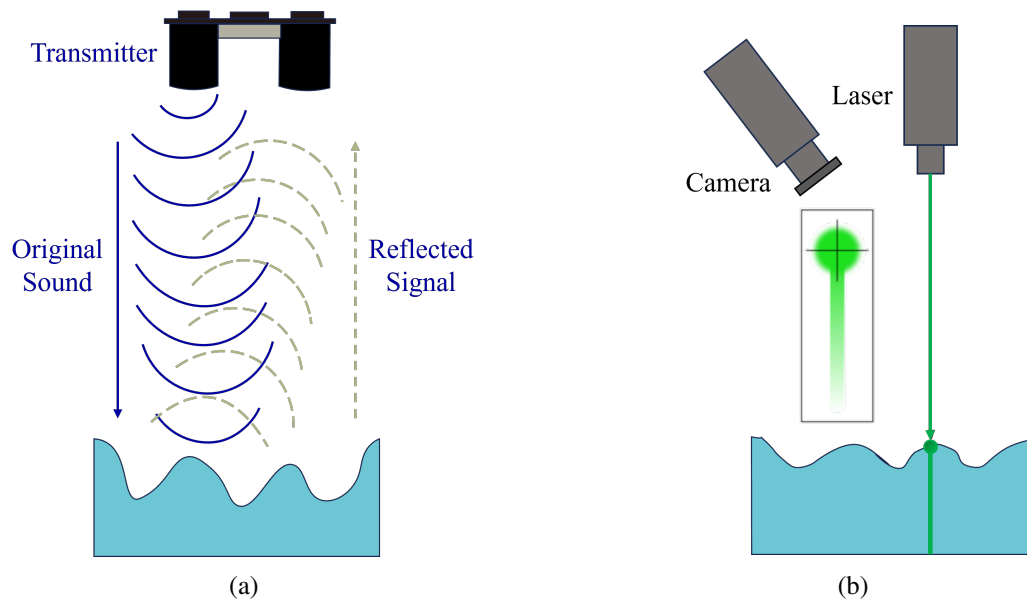
Figure 1.2: Illustration of Measuring principle of the two main **Non-intrusive** wave measuring method with (a) Ultrasonic wave prove and (b) Wave slope optical wave gauges system

hit a small area and reflect the average distance to that small area), along with the presence of a blind zone (usually 30 cm) where measurements near the sensor are not possible due to the transducer's switching time between transmitting and receiving modes. Additionally, ultrasonic distance meters are typically fixed, unlike laser-ranging devices, as the speed of sound is slower than light, limiting their ability to perform high-frequency measurements of free water surfaces.

Ultrasonic sensors perform well in two-dimensional flows with low-frequency oscillations but struggle in highly turbulent, aerated three-dimensional flows like spillways, where they produce aliased signals and fail to capture detailed time scales. In complex flows, they only provide average characteristics, and higher sampling rate instruments are preferred. Apart from application in ocean engineering, ultrasonic sensors have also been used to measure entrapped air in high-velocity flows, often in combination with high-speed imaging (Zhang et al. (2018)).

In addition to the well-established conventional means of non-intrusive water surface measurement, there are a few newer optical based measurement systems worth mentioning here.

For instance, Wave Slope Optical Wave Gauges (WSOPG) method measures wave slope by analysing laser beam deflection at the air-water interface. A submerged vertical laser refracts at the surface, with deflection angles captured by an aspheric lens-photodetector array. This method achieves sub-millimetre vertical resolution (0.1 mm) for capillary-gravity waves (Lawrence (2012)) with sampling rates up to 1 kHz, making it ideal for laboratory studies for capillary waves, especially in extrem short-wave study. Furthermore, since the absence of meniscus effect that may lead to hysteresis in probe type devices, minimal distortion should be expected.

7

However, WSOPG is inherently a single-point measurement tool, requiring multiple units for spatial coverage, as seen in Fig.1.3 which its utilization in fluid-structure interaction relatively less cost effective.
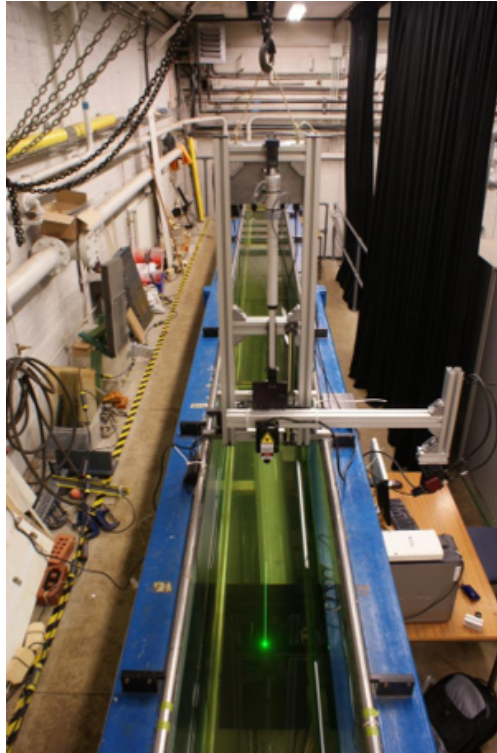
Figure 1.3: Optical Triangulation Wave Slope Gauge in use (Lawrence, 2012).

Calibration and maintenance further limit WSOPG's robustness. Variations in water properties (e.g., salinity, temperature) alter the refractive index, necessitating frequent recalibration to preserve precision. Mechanical instability—such as vibrations in floating platforms—can misalign the laser and camera, demanding rigid mounting systems.
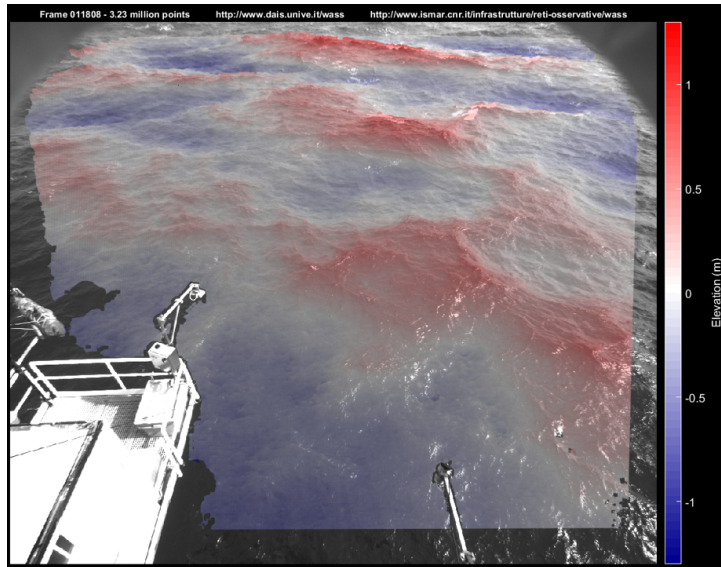
Figure 1.4: 3D point cloud result of the stereo triangulation superimposed to the one of the cameras' image of the stereo imaging system.(Bergamasco, 2017)

Similar to the WSOPG, the projection moiré method employs a single-camera system. How-ever, it combined the single camera system with the projection of a structured, sinusoidal fringe pattern onto the water surface. Two images are acquired—one of a reference plane and another of the deformed interface—whose combination produces a moiré pattern. The phase shifts observed in the moiré pattern are directly related to surface relief variations, allowing reconstruction of the full-field topography with a phase resolution typically ranging from 1/100 to 1/20 of a fringe (Lawrence, 2012). Although both techniques use a single camera, the projection moiré method offers a means to obtain spatially continuous measurements over extended areas. However, as with WSOG, careful calibration and control of environmental conditions are essential to maintain accuracy.

Both WSOPG and the moiré pattern method are capable of delivering high-accuracy measure-ments, point-based for WSOPG and surface-based for the moiré pattern method. However, an inherent limitation of these methods is their inability to be applied effectively in field studies, as both require tightly controlled laboratory environments. Due to this constraint, alternative methods must be explored for measurements in less controlled or outdoor settings.

The Wave Acquisition Stereo System (WASS) employs synchronised camera pairs and semi-global matching algorithms to generate three-dimensional wave reconstructions, shown in Fig.1.4. Spatial resolution of approximately 0.2 m can be achieved across swaths of up to 70 m Bergamasco (2017), which captures directional spectra and extreme wave events in oceanic settings. Advance version also includes automated motion compensation for ship-based data

collection Benetazzo et al. (2016) and open-source processing workflows. Challenges when deploying such measurement system include the requirement for large camera baselines (2 to 10 m), significant hardware requirement and accuracy limits of around ± 5 cm in storm conditions, making this approach less suitable for small-scale laboratory experiments Benetazzo et al. (2016).

A detailed comparison of the resolution, accuracy and capturing rate of the discussed intrusive and non-intrusive methods is provided in Table 1.1

Table 1.1: Comparison of Water Wave Measurement Methods(Masterton and Swan, 2008; Pfister and Gisonni, 2014; Guimarães et al., 2020)

Method	Typical Accuracy	Resolution	Sampling Rate
Resistance Wave Probe	± 0.5–1 mm	~ 0.1 mm	Up to 100 Hz
Point Gauge	± 1 mm (static) and 0.1 mm ideal	~ 0.1 mm	Static readings only
Ultrasonic Wave Probe	± 1–3 mm	~ 0.2–1 mm	10–50 Hz
Optical Wave Slope Gauge	$\sim 3\%$ slope error	Very high	> 100 Hz
Stereo Imaging (WASS)	± 10–50 mm	~ 20 mm (vertical)	10–30 Hz

Intrusive devices (e.g., resistance wave probes) continue to offer simplicity and low cost, remaining indispensable in many academic and industrial laboratories. However, their physical presence may interfere with delicate wave fields, limiting both measurement fidelity and spatial coverage. Non-intrusive methods (e.g., ultrasonic sensors) circumvent these drawbacks by capturing signals from a distance. Yet each non-intrusive approach brings its own challenges, including potential environmental interference and more sophisticated calibration demands. The Wave Acquisition Stereo System (WASS) is optimised for open-sea deployments, because its dense-matching algorithm relies on naturally occurring surface texture—white-caps, foam patches and wind-ruffled capillary waves—to identify point correspondences between the two cameras. In a laboratory flume such texture is absent, undermining the method's "remote and passive" appeal. In addition to its lighting requirement, WASS operates at only 10–20 Hz, while vertical RMS errors remain centimetric. These limits, acceptable for metre-scale gravity waves, are too coarse for the millimetre-level accuracy and multi-decahertz bandwidth required in the present study.

The choice of a stereo vision-based system in this thesis reflects a balance between versatility, cost-effectiveness, and adaptability to indoor and outdoor conditions. While Laser-based methods can deliver high-accuracy point based measurement, they often require refined optics, controlled

Table 1.2: Key features of intrusive and non-intrusive wave measurement methods.

Category	Strengths	Limitations
Intrusive		
	• Straightforward and cost-effective	• Risk of disturbing flow
	• Typically robust and simple to calibrate	• Limited spatial coverage unless using multiple probes
	• Well-established in lab contexts	• Physical mounts can complicate sensitive experiments
		• Reduced suitability for highly unsteady or aerated flows
Non-Intrusive		
	• Minimal disturbance to flow field	• Often more expensive in equipment and setup
	• Potential for higher data density	• Complex calibration and alignment
	• Suitable for sensitive or large-scale tests	• Environmental factors (lighting, turbidity, etc.) can degrade data
		• Some methods limited by beam attenuation or reflection angles

lighting, or specialised hardware to deal with reflections, attenuation, or complex ambient environments. In contrast, stereo vision relies on relatively standard camera equipment and image-processing algorithms, which can be configured for various scales and lighting conditions without incurring prohibitive expenses. Moreover, the adaptability of stereoscopic imaging makes it suitable not just for wave elevation measurements but also for other future endeavours, such as object tracking or automated docking, that may arise in broader marine and coastal engineering contexts.

In particular, *optical-based systems* stand out for their capacity to deliver detailed, two- or three-dimensional reconstructions of free-surface phenomena without contacting the fluid or requiring multiple expensive sensors to be installed. They can achieve high temporal and spatial resolution when properly illuminated and calibrated. While glare, specular reflection, and ambient lighting variations pose difficulties, careful design and algorithmic refinement can mitigate many of these issues. Given the complexity of modern wave–structure interaction research— where wave focusing, complex wakes, or short-lived transients are often of interest—such comprehensive, minimally invasive measurements become especially valuable. Consequently,

the following sections will focus on the state of the art in *optical measurement* techniques, with particular emphasis on stereo vision, as a promising and increasingly accessible route for detailed water wave analysis.

c. Stereo-Vision Based Water Surface Measurement

Stereo-vision methods involve capturing images from at least two perspectives to reconstruct the surface topography of fluids like water. These methods have wide application in solid mechanics for deformation measurements but face challenges when applied to fluid interfaces, particularly due to specular reflections from the water surface. To mitigate this, various light adaptations and surface seeding techniques are used.

Free-surface topography is commonly reconstructed through (i) stereoscopic matching with triangulation, based on precise camera calibration and epipolar constraints, and (ii) direct image-correlation techniques. Both approaches function in laboratory and field environments, provided reflections and correlation ambiguities are carefully mitigated. Stereo-vision offers the sub-millimetre accuracy of an optical wave-slope gauge while covering the broad spatial extent characteristic of the Wave Acquisition Stereo System (WASS). This dual capability supports highly resolved three-dimensional reconstructions in seeded, light-controlled laboratory experiments and, in field campaigns, exploits natural surface patterns—without artificial tracers or illumination—for wave and velocity measurements in natural or engineered water bodies.

In stereo-vision-based water surface measurement methods, *triangulation* is a fundamental technique used to reconstruct three-dimensional (3D) coordinates of points on a fluid surface from two-dimensional (2D) images captured by multiple cameras at different viewpoints. By leveraging the geometry of the camera setup and correspondences between images, triangulation allows for precise mapping of the fluid surface topology.

The core concept of triangulation involves identifying corresponding points in images taken from at least two different cameras positioned at known locations. Once these correspondences are established through image matching techniques, such as feature detection and correlation, each camera provides a line of sight—or a projection ray—from its optical centre through the image point into the 3D space. The intersection point of these rays represents the actual position of the point in the physical scene.

Mathematically, triangulation relies on the intrinsic and extrinsic parameters of the cameras, which are obtained through a rigorous calibration process. The intrinsic parameters include the focal length, principal point, and lens distortion coefficients, defining the internal characteristics of the camera. The extrinsic parameters describe the camera's position and orientation in a common coordinate system, effectively mapping the 2D image coordinates to 3D space (Soloff

12

et al., 1997).

Apart from traditional triangulation methods, the Direct Linear Transformation (DLT) method, developed by Abdel-Aziz et al. (2015), provides an innovative approach for photogrammetric data reduction that eliminates the need for fiducial marks or initial approximations of camera orientation parameters. This method is particularly beneficial for non-metric photography, though it is also applicable to metric photography. DLT simultaneously transforms comparator coordinates directly into object space coordinates, simplifying the data reduction process and making it more efficient.

Traditional methods typically involve a two-step process: transforming comparator coordinates to image coordinates, and then to object space coordinates, requiring calibration and iterative solutions. The DLT method bypasses this, offering a direct, linear solution that does not require initial guesses for unknown parameters. This makes it suitable for scenarios where camera orientation is not well-defined or fiducial marks are unavailable.

DLT solves the transformations using linear equations, thus eliminating the computational errors common in iterative approaches. Testing with fictitious data shows that DLT offers accuracy comparable to conventional methods but with fewer computational requirements and reduced execution time.

Both techniques aim to reconstruct accurate 3D representations of fluid surfaces but address different challenges within the stereo-vision framework. Triangulation excels in environments where precise calibration is possible, and camera parameters are well-defined. In contrast, DLT offers flexibility and computational efficiency in scenarios with limited calibration information.

Beyond computational techniques like triangulation and DLT, practical considerations are crucial for the successful implementation of stereo-vision methods in fluid surface measurements. One significant aspect is the selection of appropriate seeding particles for the fluid surface, which is essential for accurate feature detection and matching in the images.

A number of studies estimating velocity on the free surface using SPIV or LSPIV (Large Scale Particle Image Velocimetry) techniques provide examples of suitable particles for surface seeding, as seen in works by Fujita et al. (1998) and Weitbrecht et al. (2002). In particular, Weitbrecht et al. (2002) compare several particle types for LSPIV based on characteristics like density and agglomeration rate. They recommend using polypropylene particles because they have a slightly lower density than water and exhibit a lower tendency to agglomerate compared to other particle types.

Another crucial criterion is the contrast the tracer provides against the water surface. In field measurements—for instance, in rivers—the selection of tracers must also consider environmental

impacts. In this context, Chandler et al. (2008) highlight that choosing appropriate tracers and seeding methods is one of the key challenges. Their study tested the feasibility and accuracy of a digital photogrammetry system for measuring water surface elevation in a river. They used biodegradable packing chips made of starch that disintegrate within a few hours. Although they also experimented with leaves, sawdust, and wood chips, these materials suffered from a lack of contrast in the images.

Considering the methods discussed above, this thesis selects stereo-vision-based water wave measurement as the foundational method to develop bespoke techniques for various applications, which will be explored in the following chapters.

1.2.2 Principles of Shallow Water Theory

Different from that electromagnetic waves are transverse waves and acoustic waves are longitudinal waves, water waves involve a combination of both longitudinal and transverse motions.

In analogy to the transformations of permittivity and permeability of electromagnetic metamaterials, it requires the water depth and gravitational acceleration to be spatially varied along the path the water waves travel.

The latter is simply not feasible.(Zareei and Alam, 2015) Thus, majority of the researchers in this field design metamaterials that can manipulate water waves by focusing on the alternation of water depth.

There are several approaches towards water wave manipulation, but before diving into anything specific, a few background theories must be addressed first.

For incompressible and inviscid flow, conservation law of a fluid dictates that,

$$\nabla^2 \phi = 0, \tag{1.1}$$

$$\frac{\partial \phi}{\partial t} - \eta g - \frac{p}{\rho} - \frac{|\nabla \phi|^2}{2} = 0, \tag{1.2}$$

where ρ is the water density, ϕ is the velocity potential, p is the pressure, and the wave elevation is represented as η.

For shallow water condition, with long wave approximation (where the wavelength λ is much larger than any installed devices), the Navier-Stokes and continuity equation can be rewritten as

$$\nabla \cdot (h \nabla \eta) + \frac{\omega^2}{g} \eta = 0, \tag{1.3}$$

where ω stands for the wave frequency and h is for water depth.

The boundary condition at both the sea bed and the water surface can also be declared as,

$$\frac{\partial \phi}{\partial z} = 0 \quad \text{at } z = -h, \tag{1.4}$$

$$\frac{\partial \phi}{\partial z} = \frac{\omega^2}{g}\phi \text{ or } \frac{\partial^2 \phi}{\partial t^2} + g\frac{\partial \phi}{\partial z} \quad \text{at } z = 0, \tag{1.5}$$

$$\frac{\partial \phi}{\partial y} = 0 \quad \text{at } y = \pm b/2, \tag{1.6}$$

where b is the width of the water basin and h is the height of the channel.

In shallow water condition, water depth h is sufficiently smaller than the wavelength $h/\lambda \leqq$ $1/20$, the phase velocity (or group velocity) c:

$$c = \sqrt{gh} \tag{1.7}$$

Wave Numbers:

$$k = \frac{\omega}{\sqrt{gh}}, \tag{1.8}$$

$$k_x = \sqrt{\frac{\omega^2}{gh} - (\frac{n\pi}{b})^2}, \tag{1.9}$$

$$k_y = \frac{n\pi}{b}, \tag{1.10}$$

$$k_z = k, \tag{1.11}$$

where n represents wave mode number.

Before adventuring into the specific of water wave reconstruction as well as the investable discussion on the wave structure interactions in the following chapter, it is essential to accord special consideration to the pioneering research conducted by Rosales and Papanicolaou (1983) on linear waves in a rough-bottomed water channel. This study not only represented the initial endeavor towards the homogenization of the three-dimensional water wave problem but also established a foundational framework for subsequent investigations in the realm of metamaterials within the context of shallow water waves.

Rosales and Papanicolaou (1983) posited a set of assumptions pertinent to both the water channel and the waves, which remain applicable in the study of water wave metamaterials. These assumptions are as follows:

One core premise is that the water density is uniform throughout the channel. In addition, the flow is considered irrotational and inviscid, and any effects of surface tension or variable air pressure are disregarded. These choices ensure that the analysis remains focused on the essential

hydrodynamic behavior without additional complications.

The framework further assumes solitary waves that satisfy the shallow water condition, meaning that the wavelength is significantly larger than the channel depth. Under these circumstances, wave amplitudes remain much smaller than the depth, making it valid to treat the free surface as a minor perturbation. Finally, the channel bottom is characterized by subwavelength features. For instance, in a periodic bottom configuration, the length of one period is considerably smaller than the wavelength, which allows individual bottom cells to function effectively as subwavelength structures in the context of metamaterial design.

In their seminal work, Rosales and Papanicolaou (1983) embarked on the intricate task of nondimensionalizing all relevant quantities to analyse linear waves traversing rough-bottomed channels. Employing a meticulous process of nondimensionalization coupled with the application of a unified scaling methodology, they successfully derived a modified version of the Korteweg-deVries (KdV) equation. This equation adeptly governs wave elevation and showcases the mathematical finesse of their scaling and expansion techniques. However, translating these mathematical manipulations into physically intuitive interpretations presented considerable challenges due to the complex handling of intermediate mathematical constructs.

Notwithstanding these complexities, the foundational assumptions and groundbreaking methodologies adopted by Rosales and Papanicolaou (1983)—from ensuring the stability of water density and the irrotational, inviscid nature of flow, to omitting the effects of surface tension and air pressure variability, and focusing on solitary waves under shallow water conditions with minimal wave amplitudes relative to channel depth, as well as accounting for subwavelength-scale features of the rough bottom—have left an indelible mark on the field. Their analytical rigour has not only paved the way for the application of metamaterial principles in the manipulation of shallow water waves but also spurred a plethora of research initiatives aimed at leveraging the transformative capabilities of metamaterials across various wave domains. The enduring legacy of their work underscores its crucial role in advancing our understanding and capabilities in water wave manipulation with metamaterials, thereby marking a significant milestone in the ongoing exploration of wave dynamics.

1.3 Uniqueness of Water Surface Measurements and Challenges

1.3.1 Uniqueness of Water Surface Measurements

Measuring the water surface is a complex task due to the inherent characteristics and behaviors of water bodies. Several factors contribute to the uniqueness and difficulty of obtaining accurate measurements, which are crucial for applications in ocean engineering.

Firstly, the dynamic nature of water surfaces presents significant challenges. The water surface is exceptionally dynamic, constantly changing due to a multitude of environmental influences. Wind is a primary factor, generating waves and ripples that vary in size and frequency. These wind-induced waves can range from small capillary waves to large swells, each affecting the surface differently. Tides introduce cyclical changes in water levels, particularly in coastal areas, causing periodic rises and falls that can significantly alter the surface profile over time. Currents, both surface and subsurface, contribute to horizontal water movement, affecting the distribution of wave energy and the formation of surface patterns. Capturing accurate measurements in such a fluctuating environment requires instruments that are sensitive and responsive enough to detect rapid changes while also being robust against noise and irrelevant fluctuations.

Secondly, the reflective properties of water pose significant challenges for measurement techniques, especially those relying on optical methods. The water surface acts as a mirror, reflecting not only direct sunlight but also ambient light from the sky and surrounding environment. This reflectivity can lead to glare, reducing the contrast and visibility of surface features in optical images. High-intensity reflections can saturate camera sensors, resulting in loss of detail and data inaccuracies. Additionally, the specular nature of water reflections means that the angle of observation significantly affects the amount of reflected light detected by a sensor. Small changes in sensor orientation can lead to large variations in measured brightness, complicating the calibration and interpretation of optical data.

Thirdly, surface tension and capillary waves further complicate measurements at smaller scales. Surface tension causes the formation of capillary waves—small, short-wavelength ripples that propagate across the water surface. These waves are highly sensitive to disturbances like wind gusts or raindrops, leading to rapid and unpredictable changes in surface texture. Measuring these fine-scale features requires high-resolution instruments capable of capturing minute variations. However, capillary waves can introduce noise into measurements, especially in techniques like radar altimetry or optical imaging. For example, radar signals may scatter off capillary waves unpredictably, leading to inaccuracies in surface elevation data. Optical methods might struggle to resolve individual capillary waves due to their small size and rapid movement, necessitating advanced imaging techniques and data processing algorithms.

Lastly, wave-structure interactions add complexity to surface measurements. The interaction between water waves and structures, both natural and artificial, can disrupt wave patterns, creating areas of turbulence, reflection, or diffraction. Natural features like rocks, coral reefs, and vegetation, as well as man-made structures such as piers, breakwaters, and offshore platforms, alter local wave dynamics and introduce additional variables into the measurement environment.

These interactions can produce phenomena like standing waves, wave breaking, or vortex formation, which are challenging to measure accurately. Instruments must distinguish between wave motions caused by external environmental factors and those resulting from interactions with structures, requiring careful placement and calibration of sensors.

1.3.2 Illumination Challenges in Laboratory and Field Measurements

A fundamental distinction between laboratory and natural lighting conditions lies in the type of illumination source. Laboratory experiments typically utilise point light sources, whereas natural lighting predominantly originates from area light sources. This difference significantly influences illumination uniformity, reflection characteristics, and consequently, measurement accuracy in laboratory versus field environments.

In laboratory measurements, controlled illumination is an advantage, allowing manipulation of lighting conditions to suit experimental needs. However, achieving uniform illumination across the entire water surface remains challenging. Reflections from tank walls, equipment, and the water surface itself can create uneven lighting, leading to shadows and bright spots that affect measurement accuracy. To mitigate these issues, researchers often use diffused lighting systems or position light sources strategically to minimize reflections and shadows. Artificial lighting is commonly employed to maintain consistent illumination, but it can introduce problems such as glare and hotspots. High-intensity lights may reflect off the water surface at certain angles, causing glare that interferes with imaging sensors. Hotspots—areas where light intensity is significantly higher than the surrounding regions—can result from improper positioning of light sources or inadequate diffusion. Maintaining consistent lighting conditions throughout an experiment is essential for obtaining reliable and repeatable results. Variations in illumination can lead to discrepancies in measurements, particularly in time-series data where changes might be misinterpreted as physical phenomena rather than artifacts of lighting.

In field measurements, challenges are even more pronounced due to natural lighting variability. Field measurements are subject to the variability of natural lighting, which can change rapidly due to weather conditions, time of day, and seasonal variations. Cloud cover can fluctuate, altering light intensity and quality within minutes. The angle of the sun changes throughout the day, affecting the direction and harshness of shadows. Seasonal shifts impact the length of daylight hours and the sun's trajectory, introducing long-term variations in lighting conditions. Direct sunlight can produce intense glare on the water surface, overwhelming optical sensors and obscuring important features. Glare can cause saturation in images, where portions of the data contain no usable information due to excessive brightness. Conversely, shadows from clouds,

terrain, or nearby structures can create areas of low illumination, reducing contrast and making it difficult to detect surface features. The dynamic environment of the field setting, with fluctuating environmental conditions, makes standardizing and controlling illumination virtually impossible.

Adapting to variable field conditions requires a combination of hardware solutions and data processing techniques. Polarizing filters are a common tool for reducing glare by blocking certain orientations of reflected light. Neutral density filters can help manage overall light intensity without affecting the balance of colours or wavelengths. Additionally, selecting equipment with high dynamic range capabilities allows sensors to capture details in both bright and dark areas simultaneously. On the data processing side, algorithms can adjust for lighting variations by normalizing brightness levels, enhancing contrast, or correcting colour balance. Techniques such as high dynamic range (HDR) imaging combine multiple exposures to capture details across a wider range of light intensities. Machine learning approaches are also being developed to identify and correct for specific types of lighting artifacts. These adaptive strategies enhance the quality and reliability of field measurements but also add complexity to the measurement process, requiring careful calibration and validation to ensure that corrections do not introduce new errors or biases into the data.

1.4   Research Aims and Objectives

In this thesis, an innovative high resolution water wave measurement systems would be introduced in great detail with its performance benchmarked for different test scenario. Benchmarks would validate the three axis accuracy and limitation of the proposed measurement system, and further evaluate the measurement system's capability in various lab or real world application. One major application of this measurement system would be to rapidly validate and evaluate the performance of water wave metamaterial. For this ends, several basic underwater structure designs are tested in different condition and further applications of the stereo camera measurement apparatus are also presented and discussed. The applications included in this thesis apart from the water wave metamateiral are movement tracking of innovative wave energy converter, motion caption of the autonomous ship docking and ship wake measurement.

As we conclude Chapter 1 , it is important to outline the specific aims and objectives that will guide this research. The overarching goal is to contribute to advancements in ocean engineering through the development and application of high-resolution water wave measurement systems. The following aims and objectives are established to ensure a thorough investigation into this area.

Aim 1: Design and develop a high-resolution water wave measurement system utilizing ad-

vanced technologies such as stereo cameras.

Aim 2: Evaluate the accuracy and reliability of the developed measurement system in both laboratory and field settings.

Aim 3: Apply the developed measurement system to study wave interactions with various structures, including floating and underwater objects.

Aim 4: Explore the potential applications of the measurement system in monitoring the dynamics of wave energy converters.

To achieve these aims, the following specific objectives have been identified:

Objective 1: Conduct a comprehensive literature review on existing water wave measurement techniques to identify their strengths, limitations, and gaps in capability. This foundational analysis will contextualise the necessity of the proposed stereo camera system, particularly for capturing non-linear wave phenomena and operating in challenging environments such as turbid water, thereby justifying its novel contribution to the field.

Objective 2: Develop and calibrate a stereo camera-based measurement system to translate stereo-photogrammetry principles into a functional prototype. The system will resolve sub-centimetre wave features while addressing critical challenges such as light refraction and camera synchronisation. Calibration against known wave parameters (e.g., amplitude, wavelength) will ensure metric accuracy, laying the groundwork for reliable field deployment.

Objective 3: Perform laboratory experiments under controlled conditions to validate the system's robustness, with a focus on illumination challenges and data accuracy. By isolating variables such as lighting and wave frequency, these experiments will quantify operational limits and refine hardware/software configurations, ensuring consistent performance in both laboratory and real-world scenarios.

Objective 4: Analyse collected data to assess the system's capability in (i) capturing complex wave interactions with underwater structures (e.g., wave scattering) and (ii)tracking the motion of a prototype wave energy convertor model. This analysis will demonstrate the system's practical value in marine engineering applications, bridging theoretical innovation with real-world utility. Outcomes will inform safer infrastructure design and validate the system's superiority over conventional measurement methods.

These aims and objectives provide a structured framework for the research, ensuring a systematic exploration of high-resolution water wave measurement systems. By addressing both the development of new technologies and their practical applications, this work aims to make

significant contributions to the field of ocean engineering.

1.5 Outline

The contents of these chapters are:

Chapter 1 laid the foundation and demonstrate the potential of stereo vision camera implementation in wave capture capabilities. Previous researches on the deigns and the effect of water wave metamaterial as well as their inspiration are also discussed and reviewed in great length. The research objects are also given in this chapter.

Chapter 2 described a novel experimental setup for accurate water wave measurement. It includes a desktop wave flume with a controlled wave maker and a stereo camera system using the Direct Linear Transform method for precise 3D surface reconstruction. The validated system enables advanced studies of wave interactions with structures, enhancing research in ocean engineering. This Chapter addresses Objective 1 and 2 by presenting the detailed design process and experiment procedures.

Chapter 3 examined the influence of wave frequency, amplitude, and water depth on the effectiveness of different metamaterial designs in manipulating wave propagation. The experimental system is employed to capture and analyse complex wave-structure interactions, providing insights into the underlying hydrodynamic mechanisms. This Chapter builds on the foundation laid in the previous chapters and further address the Objective 3 and Objective 4.

Chapter 4 assess the performance of a scaled model of the ZOEX WEC. The system accurately captures the device's motion, enabling the estimation of power output and the analysis of its response to different wave conditions. and compares the performance of the developed stereo vision system against a well-established motion capture technology. The comparison highlights the system's strengths and limitations, identifying areas for potential improvement and further development. This Chapter addresses the Objective 4 by putting the proposed system against the commercial system to further demonstrate the robustness and versatility of the proposed system.

Chapter 2

Experimental Apparatuses and Measurements System

In the previous chapter, we established that stereo vision's potential in capturing high quality water surface. The following chapter introduces an advanced system for high-precision measurement of water waves, centred on a compact, desktop-scale wave flume capable of generating only a small number of wave crests per test. By aligning two industrial cameras equipped with tilt-shift lenses, the apparatus achieves enhanced focus control and reduced distortion over the measured region. A rigorous calibration regime, employing the Direct Linear Transformation (DLT), quantifies the system's performance and demonstrates an absolute measurement uncertainty on the order of tenths of a millimetre. These improvements mitigate the practical constraints imposed by the flume's limited length, thereby enabling detailed investigations of wave behaviour and interactions within a reduced physical domain.

2.1 Stereo Vision 3D Reconstruction Principles

2.1.1 Triangulation Principles

In conventional triangulation measurement methods, **epipolar geometry** is utilized to reconstruct spatial points from two-dimensional images, as suggested by Hartley and Zisserman (2004). Consider two cameras with principal points labelled as P_1 and P_2, respectively. A spatial point X is projected onto the image planes of the two cameras, resulting in image points x_1 and x_2. The points C_1, C_2, P_1, P_2, and X lie on the same plane, forming the **epipolar plane**, as depicted in Figure 2.1.

(a)	(b)
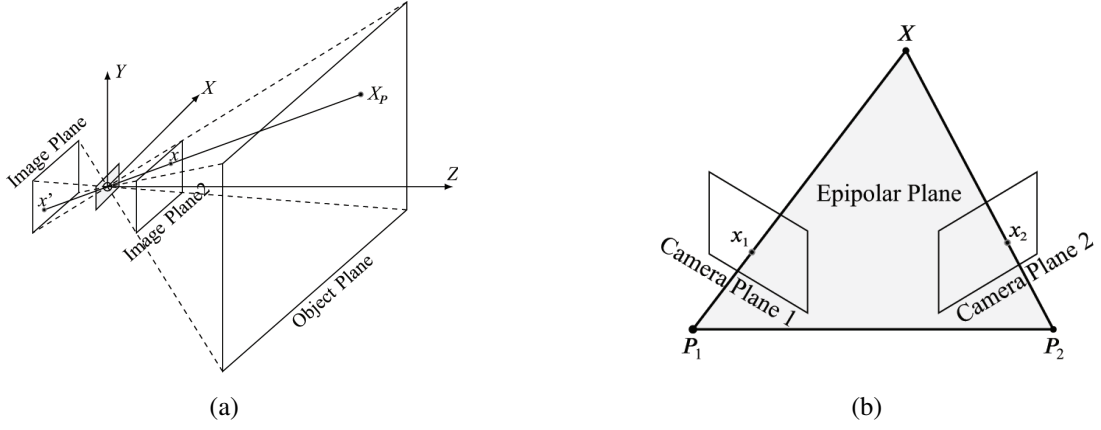
Figure 2.1: Illustration indicating the principle of triangulation (a) The pinhole model of a camera. The global coordinate system is fixed at the pinhole. (b) The epipolar geometry of a two-view stereo vision system. Zhao (2024)

The cameras are modelled using the **pinhole camera model**, which provides a reasonable approximation for lens-based cameras with medium and long focal lengths. In this model, the image is formed by projecting the spatial point X onto the image plane through a ray passing through the pinhole. An additional plane, symmetric to the pinhole image plane, is considered to obtain an upright image, corresponding to the planes C_1 and C_2 in Figure 2.1 (b).

Figure 2.1 (a) illustrates the global coordinate system fixed at the pinhole of Camera 1. Using homogeneous coordinates, the spatial point $X = (X, Y, Z, 1)^\top$ projects onto the two cameras as $x_1 = (x_1, y_1, 1)^\top$ and $x_2 = (x_2, y_2, 1)^\top$. Based on our camera model, the point projection relationship can be expressed as:

$$\begin{bmatrix} x \\ y \\ 1 \end{bmatrix} = \frac{1}{Z} \begin{bmatrix} f & 0 & 0 \\ 0 & f & 0 \\ 0 & 0 & 1 \end{bmatrix} \begin{bmatrix} X \\ Y \\ Z \end{bmatrix} \tag{2.1}$$

Here, f represents the focal length of the camera, defined as the distance between the image plane and the pinhole. The relationship between the image coordinates (x, y) and the pixel coordinates (u, v) is given by:

$$\begin{bmatrix} u \\ v \\ 1 \end{bmatrix} = \begin{bmatrix} \frac{1}{d_x} & -\frac{1}{d_x \tan \theta} & u_0 \\ 0 & \frac{1}{d_y \sin \theta} & v_0 \\ 0 & 0 & 1 \end{bmatrix} \begin{bmatrix} x \\ y \\ 1 \end{bmatrix} \tag{2.2}$$

In this equation:

- d_x and d_y are the pixel dimensions in the u and v directions, respectively.

23

- θ is the angle between the pixel axes.

- u_0 and v_0 are the coordinates of the principal point in pixel units.

The **intrinsic parameter matrix** K for the pinhole model is defined as:

$$\mathbf{K} = \begin{bmatrix} f_x & s & u_0 \\ 0 & f_y & v_0 \\ 0 & 0 & 1 \end{bmatrix} \tag{2.3}$$

where:

- $f_x = \frac{f}{d_x}$ and $f_y = \frac{f}{d_y}$ represent the focal lengths in pixel units along the camera's x and y axes, accounting for the projection transformation.

- $s = -\frac{f}{d_x \tan \theta}$ is the skew factor, accounting for any non-orthogonality between the pixel axes.

- u_0 and v_0 are the principal point offsets in pixel units.

The intrinsic matrix K encapsulates the camera's internal properties, such as focal length, principal point location, and pixel size.

To represent the cameras' positions and orientations in space, we introduce the **extrinsic parameters**, consisting of a rotation matrix R and a translation vector T. We fix the coordinate system of Camera 1 as the global coordinate system. The transformation from the global coordinate system to Camera 2's coordinate system is given by the extrinsic matrix:

$$\mathbf{E} = \begin{bmatrix} \mathbf{R} & \mathbf{T} \\ \mathbf{0} & 1 \end{bmatrix} \tag{2.4}$$

For the camera serves as the reference point for the stereo camera systme, in this case, Camera 1, since it is aligned with the global coordinate system, the extrinsic matrix is simply:

$$E_1 = \begin{bmatrix} I_{3 \times 3} & 0 \\ 0 & 1 \end{bmatrix} \tag{2.5}$$

The full projection equation that relates the spatial point X to its image point x in the camera is then:

$$\mathbf{x} = \mathbf{K} \cdot [\mathbf{R} \,|\, \mathbf{T}] \cdot \mathbf{X} \tag{2.6}$$

or, specifically for each camera:

$$x_i = K_i \cdot [R_i \,|\, T_i] \cdot X \tag{2.7}$$

where $i = 1, 2$ for the two cameras.

In light of the homogeneous coordinate system, each camera provides two independent equations from the projection relation. With two cameras, we have a total of four independent equations for the three unknown spatial coordinates of X. If the epipolar constraint is strictly satisfied, these four equations can be reduced to three.

In practice, we employ the **least squares method** to estimate the spatial point X by minimizing the reprojection error between the observed image points x_1 and x_2 and the projected points from the estimated X. This method accounts for measurement noise and leads to a more accurate reconstruction of the spatial point.

2.1.2 Direct Linear Transformation (DLT) Principles

Until this point, the calibration and reconstruction process relied on the Matlab stereo camera add-on, where the relative spatial location of the stereo cameras was calculated by detecting a check-board with known dimensions and using triangulation. This approach is conventional for 3D reconstruction and it was proved to be adequate even for measuring minor disturbances against a relatively large background.

The stereo camera calibration process, despite its widespread application, faces two significant challenges. First, its dependence on a third-party plug-in—the Matlab stereo camera add-on—limits the scope for refining the process to address subtle yet critical issues.

Second, it yields limited depth (Z-axis) resolutions, a drawback that is particularly significant for precise 3D reconstruction and the analysis of water wave propagation. Within the framework of the triangulation principle, standard calibration involves determining both intrinsic and extrinsic parameters by detecting a calibration board of known dimensions (typically a check-board), thereby calculating the relative spatial positions of the stereo cameras as well as the internal matrix of the camera characteristics such as focal length and lens distortion. Although this conventional approach is robust and capable of capturing minor disturbances against a large background, its depth resolution is approximately one or even two order of magnitude lower than that of its horizontal resolutions and is highly sensitive to the precise placement of the calibration board. To overcome these limitations, the Direct Linear Transformation (DLT) method is introduced, incorporating depth explicitly as a reference quantity during calibration and thereby enhancing the overall three-dimensional reconstruction capability.

To address these limitations and enhance three-dimensional measurement capabilities, an alternative calibration strategy, the Direct Linear Transformation (DLT) method, has been introduced. Originally proposed by Y.I. Abdel-Aziz and H.M. Karara (Abdel-Aziz et al., 2015), DLT methods offer a more robust and flexible solution, particularly regarding depth information. Unlike traditional stereo-camera methods that inadequately represent depth, DLT methods explicitly incorporate depth directions into the calibration procedure, providing comprehensive and balanced resolutions in all three spatial dimensions.

From the practical viewpoint, a key advantage of DLT calibration lies in its open, transparent, and linear formulation. Unlike the proprietary, often opaque third-party methods, DLT methods enable clear insight into the underlying mathematical algorithms. Researchers are thus free to verify each computational step involved, facilitating direct customisation, refinement, and troubleshooting tailored specifically for unique observations or challenging experimental environments.

Furthermore, the DLT method provides greater control over the calibration process. By enabling direct input and manipulation of calibration points, the system can be fine-tuned to achieve higher accuracy, which is particularly beneficial in irregular or complex environments where standard stereo camera models may not be sufficient.

In summary, the shift to the DLT method is motivated by the need for greater depth accuracy, transparency, customizability, and control in calibration and reconstruction processes. This approach aligns with the goals of the project, ensuring the system is both effective and adaptable to a wide range of applications.

The Direct Linear Transformation (DLT) method is rooted in the principles of projective geometry and linear algebra, and is a fundamental technique in fields like photogrammetry and computer vision for camera calibration and 3D reconstruction. It allows for the transformation of 2D image coordinates into 3D object space coordinates using a direct solution.

Mathematically, the relationship between image-plane coordinates (x, y) and object-space coordinates (X, Y, Z) is expressed by

$$
\begin{bmatrix} x \\ y \\ 1 \end{bmatrix} = \frac{1}{\lambda} \mathbf{P} \begin{bmatrix} X \\ Y \\ Z \\ 1 \end{bmatrix},
\tag{2.8}
$$

where $\mathbf{P}$ is the 3×4 camera projection matrix and λ is an arbitrary projective scale factor.

Every such matrix $\mathbf{P}$ obtained through Direct Linear Transformation (DLT) admits, up to

scale, the canonical factorisation

$$\mathbf{P} = \mathbf{K}[\mathbf{R} \mid \mathbf{T}], \qquad (2.9)$$

in which $\mathbf{K}$ is the intrinsic matrix of Eq. 2.3, and $\mathbf{R}, \mathbf{T}$ are the rotation and translation defining the camera pose of Eq. 2.4. Hence, DLT supplies, without further non-linear refinement, the same intrinsic and extrinsic parameters that iterative stereo-camera calibration yields.

The coefficients of $\mathbf{P}$ are found directly from a set of precisely surveyed **control points**. Solvability requires at least six non-coplanar control points whose object-space coordinates (X, Y, Z) and corresponding image-space coordinates (x, y) are known. With more than six points, an over-determined linear system results:

$$a_1 X + a_2 Y + a_3 Z + a_4 - x(a_9 X + a_{10} Y + a_{11} Z) = x, \qquad (2.10a)$$

$$a_5 X + a_6 Y + a_7 Z + a_8 - y(a_9 X + a_{10} Y + a_{11} Z) = y, \qquad (2.10b)$$

which can be written compactly as

$$\mathbf{A}\mathbf{L} = \mathbf{0}, \qquad (2.11)$$

where $\mathbf{A}$ collects the object–image coordinate pairs and $\mathbf{L}$ contains the eleven unknown elements of $\mathbf{P}$. The least-squares solution is conventionally obtained via singular-value decomposition (SVD), providing a numerically robust estimate of $\mathbf{L}$.

Consequently, DLT and classical stereo-camera calibration yield mathematically equivalent camera models; their distinction lies solely in the procedure used to estimate $\mathbf{P}$.

An important practical advantage of DLT calibration over conventional iterative stereo-camera calibration approaches lies in its intrinsically linear and direct estimation formulation. The absence of iterative nonlinear procedures simplifies the computational routine and ensures improved numerical stability. Additionally, it allows subsequent nonlinear refinements—through standard nonlinear least-squares methods such as the Levenberg–Marquardt (also known as the damped least-squares, DLS) algorithm—to further optimise the accuracy by minimising reprojection errors.

It is worth highlighting explicitly the direct connection and complementarity of DLT calibration with triangulation-based 3D reconstruction. The triangulation process, as discussed previously, reconstructs unknown spatial points by intersecting corresponding optical rays that originate from measured image points, utilising camera projection matrices. The DLT calibration explicitly provides these projection matrices, thereby facilitating accurate triangulation.

2.2 Stereo Camera Data Acquisition Set Up

2.2.1 The Cameras and Lens

Two monochrome industrial cameras (Daheng Image MER2-301-125U3M) are utilised to capture the water's surface elevation. With a resolution of 2048(H) pixels $\times$ 1536(V) pixels and a peak frame rate of 125 Frames Per Second (FPS) and within the scope of this project, the frame rate remain constant at 100 FPS, they strike an optimal balance between the frame rate and pixel density. The data would be transmitted directed to host computer's memory through high speed USB 3.0 cable before being saved to solid state hard-rives for inspection and post-processing.

Both cameras are equipped with tilt-shift lenses (Nikon 24mm f3.5D ED PC-E) instead of conventional wide-angle industrial lenses to ensure optimal control over focus and depth of field. The selection of tilt-shift lenses was driven by several key factors that contribute to improving the accuracy and precision of the captured data during the 3D wave reconstruction process.

Tilt-shift lenses offer the ability to manipulate the plane of focus independently of the camera's sensor plane, which is particularly advantageous in setups where the camera and the subject plane (in this case, the water surface) are not perfectly parallel to avoid the direct hit of the projector light. By adjusting the tilt angle of the lens, the tilt-shift lens introduces a rotation ($mathbfR_{tilt}$) about the camera's horizontal or vertical axis. Thus, we can ensure that the focus plane of both cameras aligns precisely with the projected pattern on the water surface while no large light spot is presented in the field of view to disturb both the contrast and focus of the images. This ensures that the entire area of interest, from wave crests to troughs, remains in sharp focus. This capability is essential when capturing dynamic surfaces such as waves, where small fluctuations in wave height need to be accurately recorded across a large field as shown in Fig.2.2.
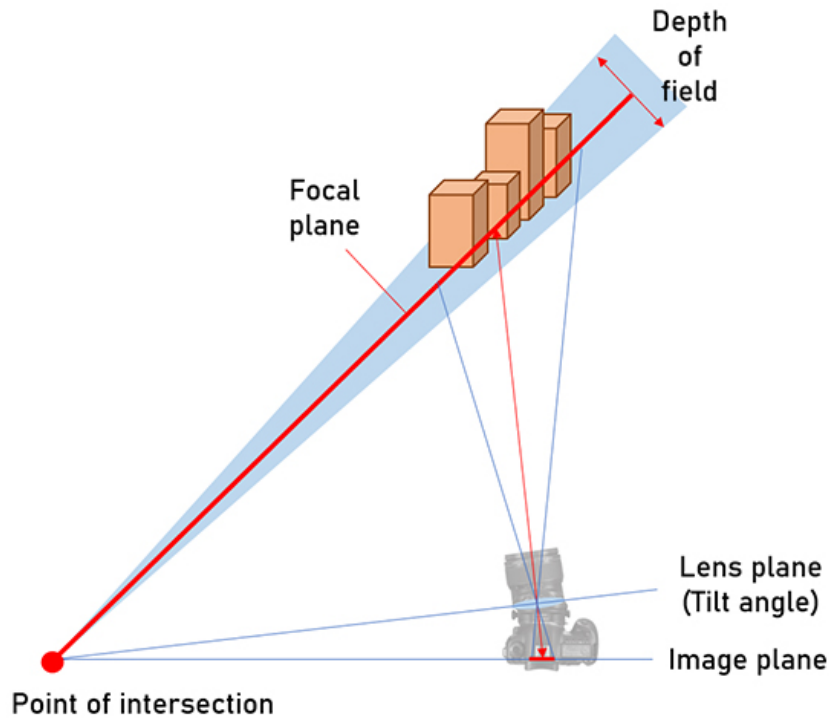
Figure 2.2: Illustration of the tilted lens principle where the tilted forward lens changes the plane of focus to forms a wedge shape, eliminating the requirement of the camera lens directly facing the target plane. SNAPSHOT (2020)

Furthermore, the use of tilt-shift lenses allows for an increased depth of field without relying solely on stopping down the aperture, which could lead to diffraction and a loss of image sharpness. The extended depth of field is crucial in this application, as it ensures that a larger portion of the wave surface remains in sharp focus, even when there are variations in wave height across the scene. This control over the focus plane is particularly important when dealing with dynamic, complex surfaces like water waves.

Another critical advantage of using tilt-shift lenses is their ability to minimize image distortion. Wide-angle industrial lenses tend to introduce barrel or pincushion distortion, which can degrade the accuracy of the 3D reconstruction process. Since accurate disparity mapping between the two cameras is vital for 3D surface reconstruction, any distortion in the captured images can result in errors in depth estimation. By using tilt-shift lenses, we minimize such distortions, ensuring that the captured images maintain their geometric fidelity and accurately represent the wave surface.

In addition to controlling distortion, the shift function of the lenses is used to avoid capturing direct light from the projector in the field of view of the cameras. Since the cameras and the projector are mounted on the same aluminum frame, reflections or direct light from the projector could cause glare or overexposure in the captured images. This could interfere with the 3D reconstruction process. By adjusting the shift of the lenses, we can exclude the direct light from

the projector, ensuring that the cameras only capture the reflected patterns on the water surface, resulting in clean, well-exposed images.

In addition to the two industrial cameras, we have also included two cinematic grade 4k cameras ZCam E2 to capture a larger region of interest in the later stage of the project. With a resolution of 3920(H) pixels x 2160(V) pixels (comparison shown in Fig.2.3) and a reliable frame rate of 60 FPS which is acceptable for capturing wave frequency up to 6Hz. It's also important to mention that we are able to retain the excellent tilt-shift lens using adapters. Given its use case in film making where multiple cameras were used to shoot one scene, Zcam synchronization can be handled internally on the camera body, without the need for external hardware or software development. Furthermore, power supply and data storage can also be handled by the camera body while external solutions are also available for specific use case.

Figure 2.3: A direct comparison of the cameras used for the measurement system where Left Hand Side is the Zcam E2 with its larger sensor and on the Right is the industrial camera Daheng Image MER2-301-125U3M

2.2.2   The Cameras Control Module

Prior to each test, the cameras' exposure time, frame rate, and digital gain are reset to session-based values using the MATLAB GenICam Toolkit, ensuring consistency. The cameras begin capturing images simultaneously the moment a signal is sent to the wave makers, ensuring that the entire experimental process, including the still water surface prior to wave generation, is fully captured for referencing and benchmarking.

Synchronization between the two cameras is essential for achieving high-quality reconstruction of the water surface. These cameras are triggered via hardware using their I/O cables connected to an Arduino NANO, which emits pulses at the same frequency as the frame rate, ensuring precise timing. Ensuring synchronization down to the millisecond level is critical

because any delay between the two cameras can significantly impact the accuracy of the disparity map and depth estimation.

The process of synchronizing stereo cameras typically involves aligning the trigger signal frequency with the frame rate. Images would only be captured once a pulse was sent from the arduous microcontroller with pre-determined gap that's normal twice the length of the camera exposure time to account for data transfer. This relationship ensures that the cameras remain synchronized throughout the data collection period, minimizing errors in the captured image sequences.

A key aspect of ensuring synchronization is minimizing the time difference between the trigger pulses received by each camera. The external trigger signal can be described by:

$$f_{\text{trigger}} = \frac{T_{\text{clk}}}{(ARR+1)(PSC+1),} \tag{2.12}$$

where T_{clk} is the clock frequency, ARR is the auto-reload register, and PSC is the prescaler. These parameters are adjusted to achieve the desired trigger frequency, which directly influences the synchronization accuracy. Properly configuring the trigger frequency ensures that both cameras capture images in sync, reducing potential errors in the reconstructed 3D surface.

Besides achieving synchronization through hardware and software configurations, external measures are employed to verify synchronization accuracy. A time display system, using an array of LEDs, is placed within the test zone to act as a visible 'timestamp' for each captured frame. This LED array showcases a binary-coded representation of time, where seconds and milliseconds are represented by distinct bits. The system provides a visual validation that the cameras remain synchronized, with preliminary results indicating synchronization precision up to the millisecond level.

Synchronization performance also depends on the baseline distance between the cameras, which directly influences the accuracy of the 3D reconstruction. Properly calibrating the stereo cameras, particularly with respect to intrinsic and extrinsic parameters, ensures that the system captures accurate depth information. The combination of precise synchronization, baseline distance, and camera calibration leads to high-quality reconstructions of the water surface, with minimal errors in depth perception.

2.2.3   Camera Focus Module

An essential aspect of camera control in our imaging system is ensuring optimal focus on the target plane. To achieve precise focusing, two cameras are set up to continuously capture images while computing real-time focus metrics that quantify image sharpness. This methodology facilitates

focus optimization by combining focus metric calculation and focus peaking visualization.

The two cameras, referred to as Camera 1 and Camera 2, are initialized with specific settings to suit the imaging requirements. Both cameras are configured with an exposure time of 6000 microseconds to control the amount of light entering the sensor, a gain of 10 to amplify the sensor signal without introducing excessive noise, and the trigger mode is disabled to allow continuous image acquisition without external triggering.

To quantitatively assess the focus quality of the captured images, the variance of the Laplacian method is employed. The Laplacian operator ($\nabla^2(\cdot)$) is a second-order derivative filter that highlights regions of rapid intensity change, effectively detecting edges within an image. The variance of the Laplacian provides a scalar value representing the overall amount of edge information, which correlates with image sharpness. Mathematically, the image sharpness metric or in this application, focus metric (F) derived from an image (I) is defined as the variance of the Laplacian-filtered image intensities:

$$F = \text{Var}\left(\nabla^2 I\right) = \frac{1}{MN} \sum_{i=1}^{M} \sum_{j=1}^{N} \left(\nabla^2 I(i,j) - \mu_{\nabla^2 I}\right)^2, \tag{2.13}$$

where $\nabla^2 I(i,j)$ is the Laplacian-filtered intensity value at pixel location $((i,j))$ of the greyscale image (I), $\mu_{\nabla^2 I}$ denotes the mean intensity of the Laplacian-filtered image, and M and N are the number of image rows and columns, respectively.

The computational steps involve capturing the greyscale image from the camera, applying the Laplacian filter to obtain $\nabla^2 I$, and calculating the variance of the filtered image. This focus metric is computed for each frame in real time for both cameras, providing continuous feedback on the focus quality.

To assist with manual focus adjustments, a visual aid known as focus peaking is implemented. Focus peaking highlights areas of the image with high spatial frequency content—typically edges—by overlaying them on the original image. This is achieved using edge detection algorithms, specifically the Sobel operator. The process involves applying the Sobel filter to the image to detect edges, resulting in an edge map E:

$$E = \sqrt{\left(\frac{\partial I}{\partial x}\right)^2 + \left(\frac{\partial I}{\partial y}\right)^2}. \tag{2.14}$$

The edge map is then superimposed onto the original image using a colored overlay (e.g., red) to highlight the edges. The combined image allows the operator to visually identify which areas are in sharp focus, aiding in manual adjustments.

The GUI updates in real time as images are captured and processed. This immediate feedback enables the operator to adjust the focus while observing both quantitative metrics and visual cues.

As demonstrated in Fig. 2.4, the program supports systematic evaluation of camera focus by clearly revealing shifts in sharpness when transitioning between near and far focal points. This approach ensures that the stereo-vison configurations maintain focus on the intended target.

| (a) | (b) | (c) |
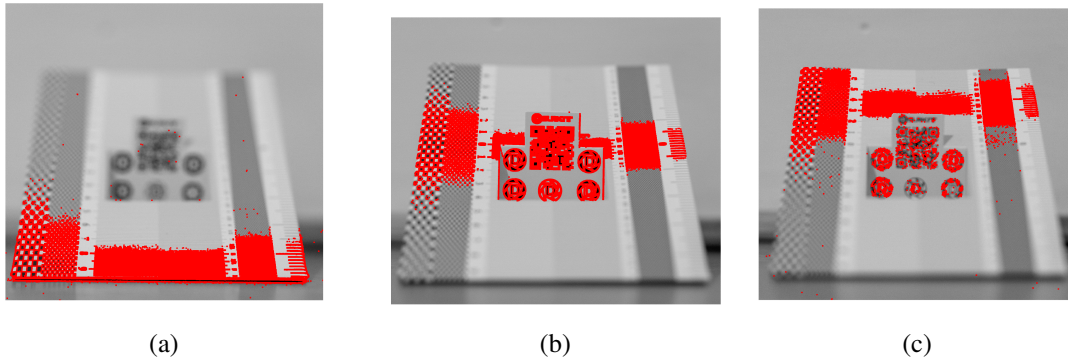
Figure 2.4: Demonstration of camera focus assistance in action when the focus plane of a single camera is move from (a) closer focus plane, (b) mid focus plane and (c) far focus plane where the red overlay indicating the area currently in focus.

The image acquisition and processing loop continues indefinitely until the operator decides to stop the manual focusing process, typically implemented with a key press event that breaks the loop. Upon termination, the video input objects for both cameras are stopped to cease image acquisition, and resources are cleaned up by deleting the video input objects and clearing associated variables.

In conclusion, the stereo camera data acquisition system is meticulously designed to capture high-quality images of the water surface for accurate 3D reconstruction. By utilizing high-resolution, high-frame-rate industrial cameras equipped with tilt-shift lenses, we achieve precise control over focus and minimize image distortion, which is essential for capturing the dynamic features of waves. The integration of cinematic-grade 4K cameras further expands the region of interest, enabling the capture of higher frequency wave phenomena. Precise synchronization between cameras is accomplished through hardware triggering and verified with a visual timestamp system, ensuring temporal alignment critical for accurate depth estimation. Real-time focus optimization techniques, including the variance of the Laplacian focus metric and focus peaking visualization, provide immediate feedback to the operator, facilitating precise manual adjustments. This comprehensive setup combines advanced hardware and software methodologies to meet the stringent requirements necessary for high-fidelity 3D wave reconstruction.

2.3 Desktop Size Wave flume

In any study in fluid mechanics with an experimental component, a wave flume is an essential component for observing interaction between water waves and structures. From the first experimental flume constructed by Reynolds (1883) to the latest circular wave basin in the FloWave Ocean Energy research facility of Edinburgh University, the core components of a wave flume has remind unchanged: a wave maker to generate controlled water wave predictably and repeatedly, a sensor system to measure the water surface elevation and an optional wave absorption component usually installed in the end of the flume. While most of the wave flume requires a stand-alone building to facilitate such as the one installed in Kelvin Hydrodynamic Laboratory which is 76 m × 4.6 m × 2.5 m, in this section, the designs and deployment of a desktop size wave flume is discussed.
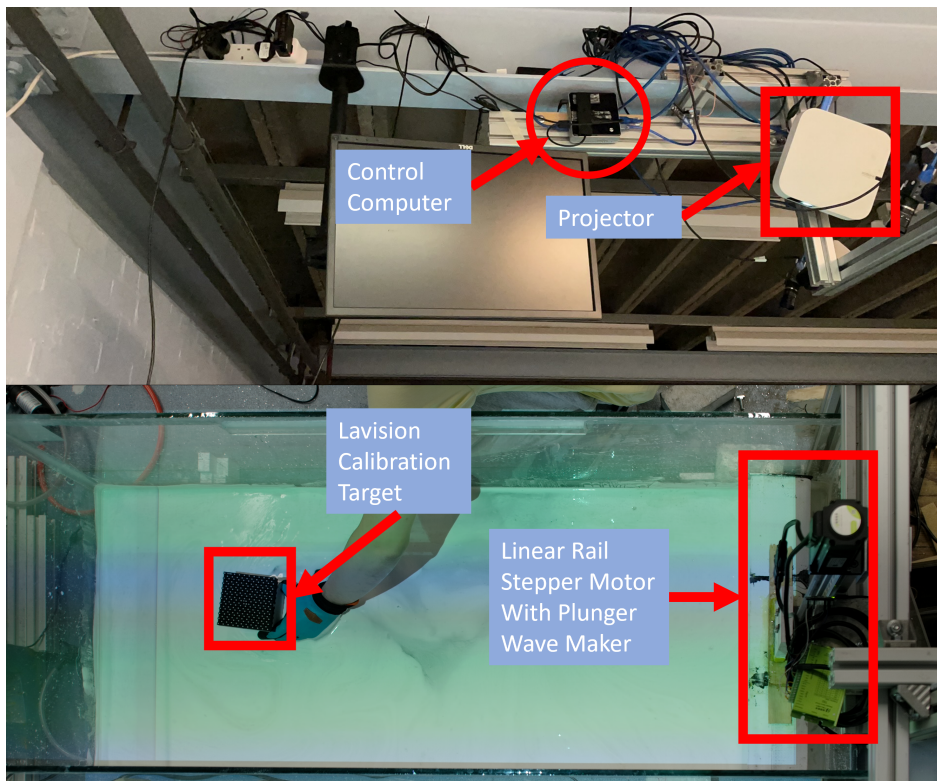
Figure 2.5: Experimental setup demonstrating the modified aquarium including the control computer, projector for illumination, the LaVison calibration target and the plunger type wave maker connect to a liner rail driven by a stepper motor. The water surface is seeded with microsphere glass bubbles.

2.3.1 Overview

The main body of the wave flume is a modified aquarium consist of 10 mm thick glass that is 1530 mm in length and 600 mm in width.

A projector (XGIMI Elfin) with a native resolution of 1280×720 pixels and cable of producing image 400 Lumes in brightness, is fixed over the tank to project patterns on the water surface.

The water surface is seeded with hollow microsphere glass bubbles (3M K20). The microbubbles have a average diameter of 60 μm and a density of 0.20 g/cm^3. They are floating on water forming a monolayer to enhance the reflective ratio of water surface. The microbubbles are sprinkled on the water surface generously to cover the entire surface then left to fully settle to provide optimal reflection ratio without any lump that may affect the water surface tension.

The patterns projected onto the water surface are captured by two global-shutter industry cameras (Daheng Mercury2 USB 3.0) at a frame rate of 125 frames per second (FPS) with a resolution of 1536×2048 pixels. Two cameras are controlled by Matlab and synchronised by another Arduino Nano board. The desktop wave flume is compact that no wave absorber module is placed at the right end of the flume body, which limited the experiment performable in the flume at the current stage. However, the absence of a wave absorber would raise the issue of wave refection and its impact, which would be addressed in the following section.

2.3.2 Stepper Motor Drive Plunger-Type Wave Maker

A plunger-type wavemaker is located at the left side of the tank. The plunger, with a right-angled isosceles triangle cross section, is 3D printed using a FDM printer (Anycubic Kobra Plus). To completely seal off the water section behind the wave maker and ensure the quality of the generated waves, an extra layer of silicone pad is added to both sides of the plunger, ensuring a tight fit in the gap between the side of the plunger and the side of the flume.

The theoretical capability of the plunger-type wavemaker is governed by the relationship between the motion of the plunger and the resulting wave characteristics. For a vertically oscillating plunger, the wave generation is primarily determined by the stroke of the plunger and its submerged depth. According to the theory of plunger-type wavemakers, developed for two-dimensional symmetrical models, the motion of the plunger creates surface waves that propagate outward from the source. These waves can be modeled by assuming ideal, incompressible, and irrotational flow, allowing the use of linearized surface wave theory, as suggest in Fig. 2.6.
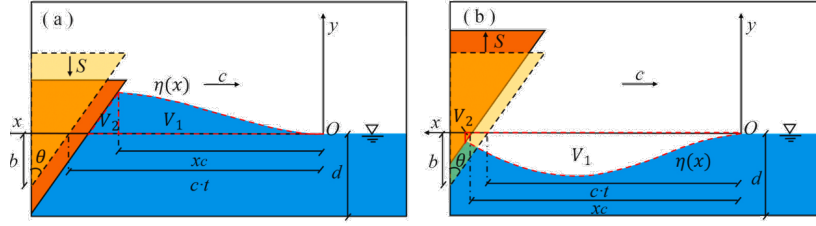
Figure 2.6: Illustration of the relationship between the inflow volume of the wedge and the wave volume: (a) wedge moving downward, (b) wedge moving upward.((Sun et al., 2021))

The vertical motion of the plunger leads to a displacement of the water surface, where the volume of displaced water is directly related to the wave amplitude. The relationship between the submerged volume of the wedge-shaped plunger and the wave generation is expressed by the mass conservation principle:

$$V_t - V_0 = V_1 + V_2 \tag{2.15}$$

where V_t is the volume of the plunger submerged at time t, V_0 is the initial submerged volume, V_1 is the volume of water displaced above the still water surface, and V_2 is the volume displaced below the still water surface Sun et al. (2021). This principle ensures that the generated waves maintain a consistent profile relative to the motion of the plunger. The wave amplitude H generated by the plunger is a function of the stroke S, wedge angle θ, and the wave profile. For example, for a linear wave, the profile can be described as:

$$\eta(x) = \frac{H}{2}\cos(kx + \phi) \tag{2.16}$$

where k is the wave number, H is the wave height, and ϕ is the phase angle. The wave height is constrained by both the plunger's stroke and the wedge angle θ, as described by the following relationship:

$$S^2 \cdot \tan\theta + Sb\tan\theta = \frac{H}{2k}\sin(kx + \phi) \tag{2.17}$$

This equation allows the calculation of the wave amplitude based on the plunger's motion. Moreover, the quality of wave generation depends on factors such as the wedge angle and the initial submergence depth of the plunger, with the ideal conditions occurring when the stroke and wave amplitude maintain a consistent ratio.

In addition to linear waves, the plunger-type wavemaker can generate more complex waveforms, such as Stokes fifth-order waves, solitary waves, and irregular waves such as sea-states governed by the JONSWAP spectrum. Each wave type imposes its own constraints on the motion

of the plunger, with the wave profile being governed by higher-order terms that account for nonlinearity in the wave shape. These factors contribute to the accuracy and quality of the generated waves, which are essential for replicating realistic ocean conditions in the wave flume.

The wavemaker is driven by a stepper motor while the motor itself is directly controlled by a Arduino Nano 33 BLE board using our in house script given that the built-in Arduino stepper motor library could only support linear acceleration.

In the design of the desktop wave flume, the choice of actuator is critical for achieving the desired performance characteristics. Among the options considered, the stepper motor, in conjunction with a linear guided rail, emerges as the most suitable choice. This configuration is capable of instantly achieving high velocities thanks to its high torque, while also maintaining exceptional precision in displacement. The precision afforded by this setup is further enhanced when the motor driver is equipped with micro-stepping capabilities, allowing for finer control over movement.

The chosen stepper motor for driving the plunger-type wave maker distinguishes itself from alternatives such as linear or servo motors, offering a balance of speed and accuracy that is ideally suited to the application's requirements. The specifications of the stepper motor used are detailed below:

Table 2.1: Specification of the Stepper Motor

Parameter	Value
Stepper Motor Type	Nema 23
Maximum Rotational Velocity	1500.00 rpm
Linear Displacement per Rotation	0.004 m/rotation
Maximum Linear Velocity	6.00 m/min (0.10 m/s)
Maximum Torque	190.00 Nm
Maximum Load Capacity	500.00 N
Micro-Stepping Range	1 to 32

It's worth mentioning that, the motor driver provide several micro-stepping options from one, 200 steps to finish one rotation to thirty-two, 6400 steps to finish one rotation.

In terms of motor capability, the NEMA 23 stepper motor is capable of driving the plunger at a maximum frequency of 6Hz with a plunger amplitude of 4mm, sufficiently covers the desired wave properties of the desktop wave flume.

Having established the hardware setup, the subsequent phase involves equipping the hardware with appropriate software. Specifically, a script is required to enable the stepper motor to execute movements in a sinusoidal pattern, adhering to predefined frequency and amplitude parameters.

There are primarily two methodologies one could employ to construct the script: the utilization of the tone function or traditional motor control techniques.

Tone Function Control Script

Tone function in Arduino board can generate a square wave of the specified frequency. While it's usually used to generate sounds with different electric components, being able to specify frequencies can be used in our advantage to generate sinusoidal velocity profile.

The main challenge in utilizing tone function is to calculate the correct frequency in each micro-step to realize the input frequency and amplitude.

Firstly, delay time (time-step) need to be calculated by dividing one period into pre-determined pieces,

$$f_{tone} = 2\pi A f \frac{P}{S} \sin(2\pi f t),$$ (2.18)

where A is the amplitude of the wave to be generated (mm), f is the wave frequency (Hz), P is the number of subdivisions per wave period, S is the total number of motor steps per unit amplitude (steps/mm) and t denotes time (s).

Note that the delay time in Arduino is in microseconds, (10^{-3} s) and must be a round number, making the time-step imprecise.

Since the whole movement was divided into pieces, the angle (the angular displacement in rad) in each individual piece i need to be calculated, The angular increment for each subdivision (θ_i) is computed as:

$$\theta_i = \frac{2\pi i}{P}, \quad i = 1, 2, ..., P$$ (2.19)

where i denotes the current subdivision number and P the total subdivisions per wave period.

With the given angle, the frequency (pulse per second) input for the tone function can be calculated,

$$n_{\text{pps},i} = A N_s f \sin \theta_i$$ (2.20)

where $n_{\text{pps},i}$ is the pulse rate command for subdivision i in steps per second.

Note that the A here is the input amplitude in steps. The PPS value serve two important functions:

- As the frequency input for tone function, which can translate to the required velocity profile where

$$v_i = \frac{n_{\text{pps},i}}{A N_s \pi}$$ (2.21)

  where v_i is the instantaneous plunger velocity (mm/s).

- Negative or positive PPS can be used to identify the required motor direction.

Conventional Motor Control Script

One alternative approach would be switching the tone function for conventional stepper motor control where the stepper motor would travel equal amount of distance in calculated given time as illustrated in Figure 2.7. The figure illustrates the ideal displacement of a stepper motor over time for a 0.52 Hz, 0.076 mm wave. Each motor rotation translates to 4 mm of vertical movement and is divided into 2000 steps. The main plot (a) shows the overall displacement against time, forming a broad "S"-shaped curve that splits into an upper and lower branch. The smaller subplots (b) and (c) provide zoom-in views of the top point—where the motor reaches its amplitude and changes direction, leading to the small gap (less than roughly 0.02 s)—and the starting point—where incremental step movement is clearly observed.
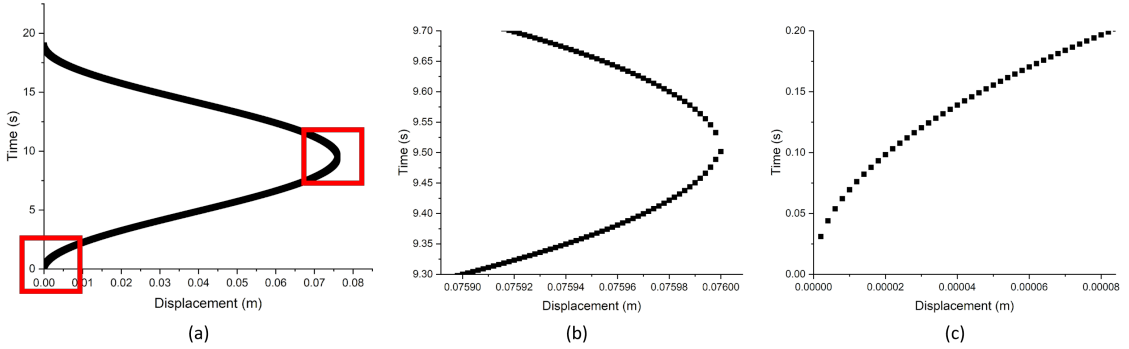
Figure 2.7: The ideal displacement of stepper motor against time with a 0.52 Hz 0.076 mm, wave, each rotation of the motor translates to 4 mm in vertical movement and is divided into 2000 steps where (a) is the overall displacement against time; (b) the zoom-in look at the top point of the motor movement;(c) the zoom-in look of the starting point of the motor movement.

The main challenge in this step is to calculate the assigned time for each individual micro-step. The equation for time is,

$$t_i = \frac{\arccos\left(1 - \frac{2i\Delta s}{A}\right)}{2\pi f}, \qquad \Delta s = \frac{1}{N_s}, \tag{2.22}$$

where t_i is the cumulative time at micro-step i in s, and Δs the linear travel per micro-step in mm.

Note that the frequency here is in rad/s and Time(i) is not the assigned time for step i but the accumulated time till step i. One more step is needed to calculate the time step,

$$\Delta t_i = t_i - t_{i-1}, \qquad t_0 = 0, \tag{2.23}$$

where Δt_i is the assigned dwell time for the i-th micro-step in s. Change of direction can be easily

achieved by changing the signal on direction pin of the Arduino once the amplitude is reached while keeping the time step calculation intact.

At each given number pieces, the error between Arduino calculated time-step and Arduino output time step (due to calculation time and various source of latency) can be considered quasi constant with less than two percent variation, making it possible to achieve better accuracy in frequency by taken the error value into account.

Comparison

Using the tone function is able to provide accurate output in frequency since the motor needs to travel different distance in the same time frame. However, it relies on selecting proper number of pieces to achieve accurate amplitude output. For instance, with small number of pieces and a large input amplitude, the output pieces will be significantly smaller than the input.

The conventional means, on the other hand, can provide accurate output in Amplitude since the motor now is required to travel the same distance in different calculated time step. To achieve acceptable output frequency (which directly results in velocity), the number of pieces (to finish one rotation) also need to tweaked based on the given amplitude. For instance, a small amplitude with high frequency input may need smaller number of pieces to jump start the acceleration while a large amplitude with low frequency input may required larger number of pieces to achiever smoother motion.

A Combined Method With New Components

With the new microcontroller Arduino NANO BLE 33 and its improved ARM based chipset (with clock speed 4 times the previous Arduino NANOs), better timing and stepping accuracy can be achieved.

The new script utilize the tone function for accurate frequency. With a improved understanding of both stepper motor and the tone function, it's also possible to achieved accurate amplitude. For instance, a set-up with a fixed 10 micro step ratio (2000 steps per rotation) and a 4mm step can yields the following equation:

$$\Delta x = n_{\text{pps}} \, t \, \frac{L_r}{N_r} \tag{2.24}$$

where Δx is the commanded displacement in a time slice in mmn_{pps} the applied pulse rate in steps per second, $L_r = 4$ mm the lead-screw travel per full rotation, and $N_r = 2000$ the micro-steps per rotation.

Thus, given the amplitude (in mm), frequency (in Hz) and timestep (in micro-second), the

tone output frequency (pulse per second) in one given time step can be calculated as:

$$n_{\text{pps},i} = A\,\Omega\,\frac{P}{\Delta s}\,\sin\!\left(\Omega\,\Delta t\,i\right), \qquad \Omega = 2\pi f \tag{2.25}$$

where Ω is the angular frequency in rad per second.

Extra Built-in Function: Wave Probe Calibration

In addition to driving the plunger in a sinusoidal motion, the stepper motor integrated into the system can also be repurposed to automate the wave probe calibration process, which is traditionally performed manually. This enhancement is achieved through a dedicated Arduino script, allowing for greater precision and repeatability in calibration.

The calibration process involves the stepper motor executing a controlled movement pattern. First, the motor moves upward in 13 discrete steps, with each step corresponding to a 4 mm displacement. This results in a total upward displacement of 52 mm from the starting position. Each step includes a movement phase lasting 2 seconds, followed by a 4-second pause during which data from the wave probe is collected and stored. This ensures sufficient time for the probe to stabilize and record accurate measurements.

After reaching the 52 mm mark, the motor reverses direction, moving downward in 26 steps to a position 52 mm below the starting point. Similar to the upward motion, each step consists of 2 seconds of movement followed by 4 seconds of data collection. Finally, the motor returns upward in 13 steps, bringing it back to the original starting position, thereby completing the calibration cycle.

The complete procedure would produce 53 data points to calculate the calibration factor linearly with higher accuracy than the manual procedure which would be used in chapter 4.

2.3.3 Wave–wall reflection and its mitigation

Given the fact that flume is only $L_{\text{tank}} = 1.53\,\text{m}$ long, a physical beach would consume too much of the optical field and is therefore impractical. In the absence of an effective wave absorption device, the reflection problem is therefore controlled through running limited number of wave for a test, controlled experiment length and subsequent numerical filtering.

An example of a 2 Hz wave moving across the desktop flume is shown in Fig. 2.8 by presenting an elevation time history of a horizontal row of markers. The thin black traces is the instantaneous profiles of every frame while the green and dark blue polyline is the crest and trough spline of the leading incident wave. The critical region of data acquisition is shown in blue shadow while the region most contaminated by the wall reflection is shown in shadowed red
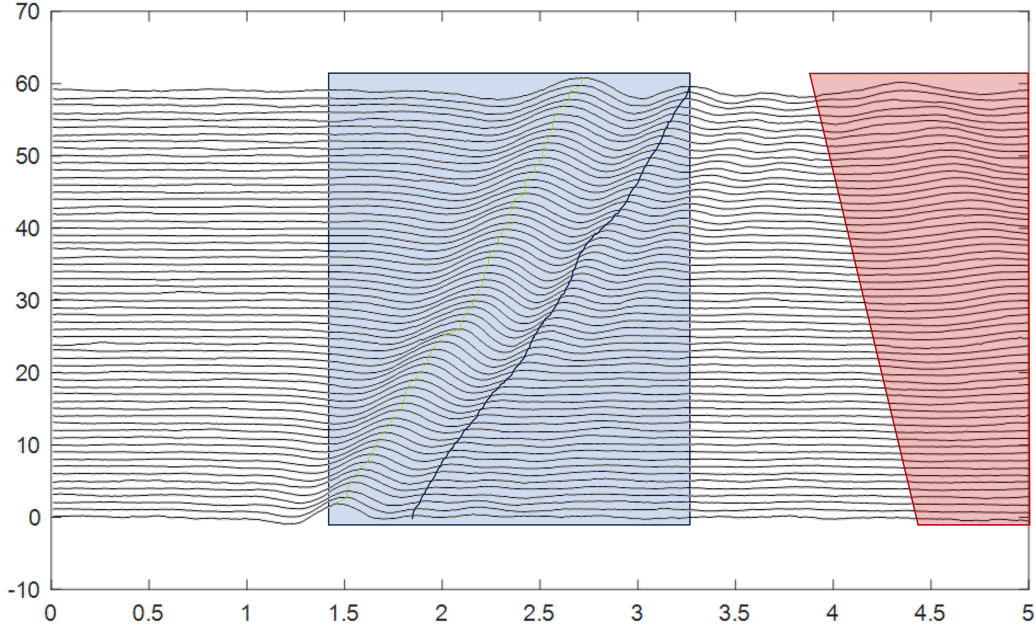
Figure 2.8: A slice of the wave time history data across the desktop flume in a 2 Hz wave, the critical region of data acquisition is shown in blue shadow while the region most contaminated by the wall reflection is shown in shadowed red.

The still-water depth is $h = 50\,\text{mm}$. In shallow water the common phase and group speed is

$$c = \sqrt{gh} = \sqrt{9.81 \times 0.05}\,\text{m}\,\text{s}^{-1} \approx 0.70\,\text{m}\,\text{s}^{-1}. \tag{2.26}$$

The fastest excitation used is $f = 2.0\,\text{Hz}$, thus,

$$T = \frac{1}{f} = 0.50\,\text{s}, \qquad \lambda = cT = 0.35\,\text{m}. \tag{2.27}$$

Only three crests are generated, giving an incident packet length

$$L_{\text{train}} = 3\lambda = 1.05\,\text{m}, \tag{2.28}$$

which is less than the stereo field of view $L_{\text{ROI}} = 1.20\,\text{m}$.

The leading crest reaches the downstream wall after

$$t_1 = \frac{L_{\text{tank}}}{c} = \frac{1.53}{0.70}\,\text{s} \approx 2.2\,\text{s}, \tag{2.29}$$

and then needs

$$t_2 = \frac{L_{\text{tank}} - L_{\text{ROI}}}{c} = \frac{1.53 - 1.20}{0.70}\,\text{s} \approx 0.47\,\text{s}, \tag{2.30}$$

to reach the upstream edge of the optical window. The reflection therefore first appears in the region of interest at

$$t_{\text{ref}} = t_1 + t_2 \approx 2.7\,\text{s}, \tag{2.31}$$

and fills it completely only at

$$t_{\text{full}} = t_{\text{ref}} + \frac{L_{\text{ROI}}}{c} \approx 4.4\,\text{s}. \tag{2.32}$$

The stereo record is limited to $t_{\text{rec}} = 5.0\,\text{s}$. Hence the fraction of stored frames containing any reflected energy is

$$\Gamma = \frac{t_{\text{rec}} - t_{\text{ref}}}{t_{\text{rec}}} = \frac{5.0 - 2.7}{5.0} \approx 0.46, \tag{2.33}$$

and the reflection occupies the whole optical field for only $5.0 - t_{\text{full}} \approx 0.6\,\text{s}$, which corresponds to less than twelve per cent of the integrated wave energy in the raw dataset.

Residual reflections present after t_{ref} are further suppressed by the phase-aligned superposition and neighbourhood repair method described in next section; such procedure eliminates most of the reflected amplitude without affecting the incident wave field.

2.4 Post-processing/3D Wave Measurement Module

The post-processing can be easily divided into three clear parts where a more detailed process is depicted in Fig.2.9:

1. Calibration of stereo-Camera system;

2. Perform 3D Reconstruction of water wave surface;

3. Presenting the reconstruction results.

2.4.1 Calibration Procedure

Accurate calibration of the stereo-camera system is essential for precise 3D reconstruction and measurement. The calibration process was conducted using MATLAB's Stereo Camera Calibrator app, which estimates the intrinsic and extrinsic parameters of each camera, as well as the relative orientation and position between them.

An alumina calibration target featuring a 12×9 checkerboard pattern with $15\,\text{mm} \times 15\,\text{mm}$ squares was employed. This high-contrast, precisely manufactured checkerboard is ideal for calibration because it provides a large number of identifiable feature points. The calibration target
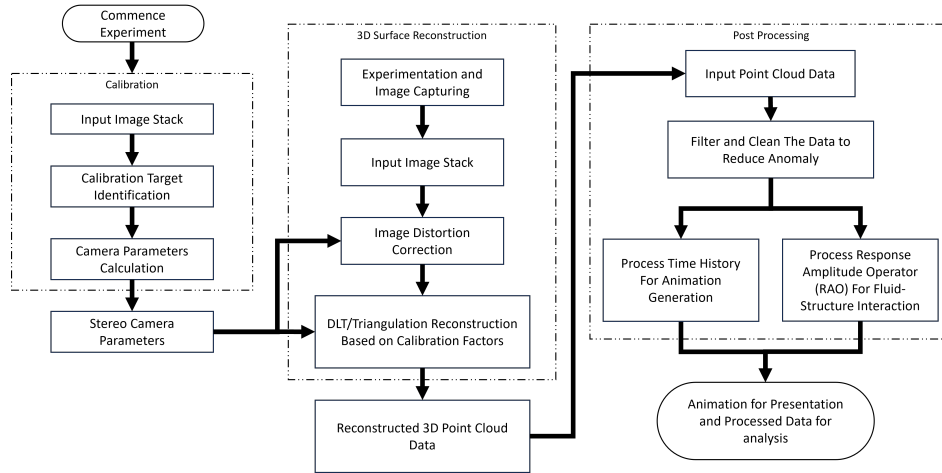
Figure 2.9: Workflow diagram illustrating the data flow of the proposed reconstruction process including the calibration process, 3D reconstruction steps, and subsequent post-processing.

was moved slowly throughout the overlapping field of view of both cameras—the mutual capture region to ensure comprehensive coverage of the operational volume. During this movement, slight rotations around the three axes were introduced. These rotations are critical as they present the checkerboard at different angles, enabling the calibration algorithm to better understand how the cameras perceive depth and perspective.

A total of 50 pairs of synchronized photographs were captured. Synchronization was crucial to ensure that each pair of images represented the same moment in time, thereby eliminating temporal discrepancies that could affect calibration accuracy. The cameras were configured to operate simultaneously, often using hardware or software triggers to achieve precise synchronization.

These image pairs were then processed using the Stereo Camera Calibrator. The software automatically detected the corners of the checkerboard in each image, a process that relies on edge detection and pattern recognition algorithms. Once the corners were identified, the software matched corresponding points between the left and right images. Using these correspondences, the calibrator computed the intrinsic parameters of each camera, such as focal length, principal point, and lens distortion coefficients. It also determined the extrinsic parameters, including rotation and translation vectors that describe each camera's position and orientation in space.

The calibration was performed prior to conducting any experimental tests to ensure that all subsequent measurements would be based on accurately calibrated camera parameters. This proactive approach is essential for experimental integrity, as any errors in calibration could propagate through the data analysis, leading to incorrect conclusions.

The outcomes of the calibration process included:

Intrinsic Parameters: These define how each camera maps 3D points in the world to 2D

points in an image. They include the focal length, optical centre (principal point), and lens distortion coefficients (radial and tangential distortions). Typically encapsulated by the calibration matrix

$$\mathbf{K} = \begin{pmatrix} f_x & 0 & c_x \\ 0 & f_y & c_y \\ 0 & 0 & 1 \end{pmatrix},$$

where f_x, f_y denote focal lengths, and (c_x, c_y) is the principal point. Lens distortion is often modeled by coefficients $\{k_1, k_2, p_1, p_2, \dots\}$ for radial and tangential effects.

Extrinsic Parameters: These describe the position (translation vector $\mathbf{t}$) and orientation (rotation matrix $\mathbf{R}$) of each camera relative to the world coordinate system or to each other. They consist of rotation matrices and translation vectors.

Stereo Parameters: These capture the relative rotation and translation between the two cameras, essential for depth perception and 3D reconstruction.

To evaluate the theoretical performance of the proposed triangulation algorithm, a comprehensive virtual experiment was conducted using Blender, an open-source 3D creation suite renowned for its high precision and versatility in modelling and rendering. The primary objective was to create a controlled environment where variables could be manipulated, allowing for an in-depth analysis of the algorithm's capabilities under ideal and near-ideal conditions.

The virtual set up consists of two cameras whose property from lens parameters and sensors size and resolution, a calibration target that's the same set up as the one used in the lab and an even light source similar to the light condition during tank calibration.

During the virtual calibration, to intimate the tank calibration procedure, the virtual calibration target would also move throughout the overlapped area of the stereo cameras in both plane axis, depth axis and also rotation around each axes. The post-processing process for the calibration can be best illustrated in Fig. 2.10. The calibration pattern is a checkerboard, and the detection process identifies the corners of the pattern within each camera's view. In the detected images, the corners are represented by green circles, while red plus symbols indicate the reprojection points. The reprojection points reflect the accuracy of the calibration algorithm in predicting the positions of the detected corners based on the camera model. In both camera views, the origin of the checkerboard pattern is indicated by the yellow square at the coordinate (0,0). This detection and reprojection comparison are crucial for evaluating the accuracy of the camera model.

After detecting the corners in both cameras, the 3D positions of these points are reconstructed in space. The 3D plot displayed in the upper right section of the figure illustrates the detected

(a)

(b)

(c)
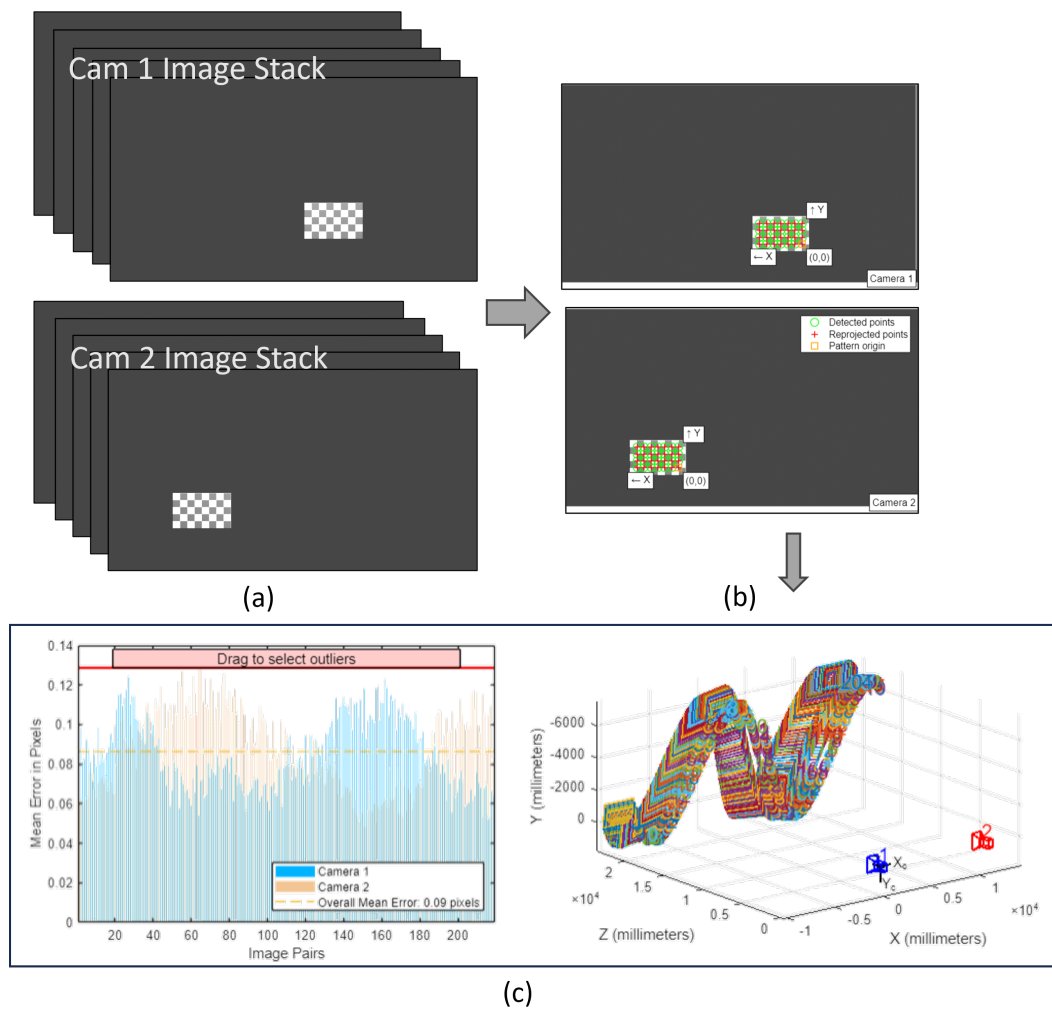
Figure 2.10: The post processing process of virtual stereo camera calibration and sample results where (a) illiterates the stereo image stacks, (b) represents the target identification of each individual frame and (c) the final calibration results demonstrating the movement of the checkerboard in the virtual space.

points' positions within a 3D coordinate system (X, Y, Z axes). The points from Camera 1 and Camera 2 are shown in blue and red, respectively. During the post-process, it's important to establish that throughout this thesis, the base of triangulation or the origin of the local coordinates system is fixed at Camera 1, which explains the spatial fluctuation presented in the transformed target trajectory from Camera 2. This plot provides a visual representation of the spatial accuracy of the detected and reprojection points. In this instance, the reconstruction follows a sinusoidal pattern, indicating a periodic or controlled variation in the pattern's spatial configuration.

Finally, the calibration process includes an error analysis of the reprojection accuracy. The bar graph in the lower right section of the figure shows the mean reprojection error for each image pair, with the mean error on the Y-axis and the image pair index on the X-axis. Camera 1's reprojection error is depicted in blue, and Camera 2's in beige. In contrast, the overall median error is represented by a dashed yellow line, which indicates an error of 0.0365 pixels. The results show that the calibration error for most image pairs is well below the acceptable threshold, confirming that the stereo camera system has been successfully calibrated.

In addition to virtual experiment setup lab environment calibration are also documented in the Fig. 2.11. Compared with the virtual calibration, the lab environment is subject to several uncertainties and potential errors.

Lab Environment Calibration Process Lab Environment Calibration Results
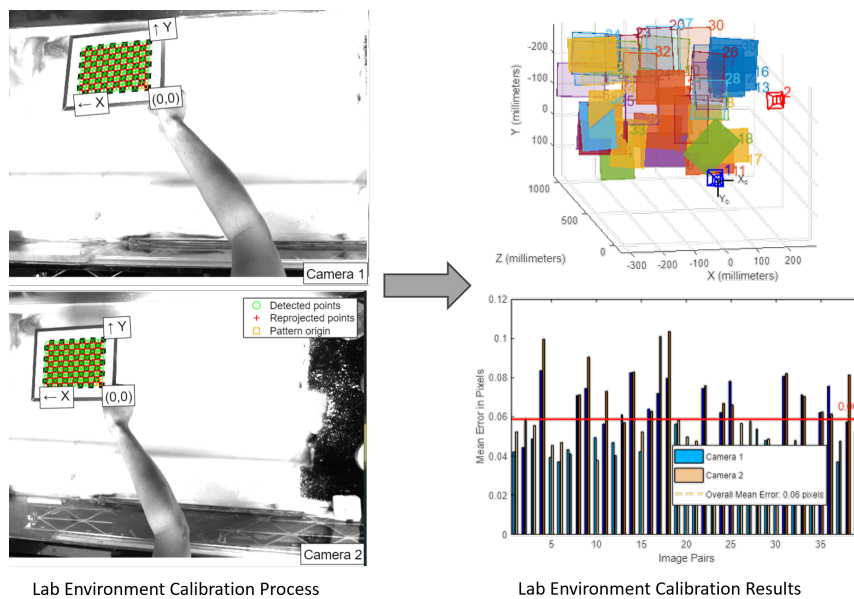
Figure 2.11: The post processing process of lab stereo camera calibration and sample result sets

Notably, the variance in reprojection error is slightly higher in the lab setup, with some image pairs exceeding the acceptable threshold of 0.06 pixels due to real-world noise and calibration inconsistencies. Nevertheless, the real-world calibration remains robust and accurate, confirming the efficacy of the proposed algorithm in both ideal and practical conditions.

The precise calibration of the stereo-camera system was critical for achieving accurate 3D reconstructions and measurements in this study. Utilizing MATLAB's Stereo Camera Calibrator app and a high-contrast alumina checkerboard target, the intrinsic and extrinsic parameters of each camera were successfully estimated. The calibration process was rigorously tested through both virtual experiments in Blender and real-world lab setups. The post-processing results, illustrated in Figures 2.10 and 2.11, demonstrated that while the lab environment introduced slight variances in reprojection error due to real-world noise and calibration inconsistencies, the overall calibration remained robust and accurate. The mean reprojection error stayed well below the acceptable threshold in both virtual and lab setups, confirming the effectiveness of our calibration procedure. These findings provide confidence in the reliability of subsequent experimental analyses using the proposed triangulation algorithm under both ideal and practical conditions.

2.4.2 Reconstruction Procedure

Conventionally, wave reconstruction employs the same checkerboard pattern used for system calibration (Fig. 2.12), offering structural simplicity. However, preliminary testing revealed an inherent compromise between spatial resolution and computational efficiency when using this approach.

As demonstrated in Fig. 2.12(c–d), low-density patterns enable faster processing (multiple frames/minute) but suffer from insufficient spatial resolution, while high-density grids require prohibitively long processing times (5 minutes/frame). This computational bottleneck rendered real-time monitoring and large-scale post-processing infeasible with available hardware (Zhao, 2024).

This limitation motivated the development of an optimised dot grid pattern (Fig. 2.13), featuring alternating parity in row/column counts (e.g., odd columns with even rows) to ensure unambiguous wave propagation detection. The grid's 27×50 resolution provides complete flume coverage while maintaining feature distinctiveness.

The revised methodology employs MATLAB's `imfindcircles` function, implementing a Circular Hough Transform (CHT) algorithm for robust marker detection. CHT operates by transforming image edge points into a parameter space where potential circles are identified through voting:

$$(x-a)^2 + (y-b)^2 = R^2 \tag{2.34}$$

Edge points (x_i, y_i) detected in the image contribute votes in the accumulator space (a, b, R).
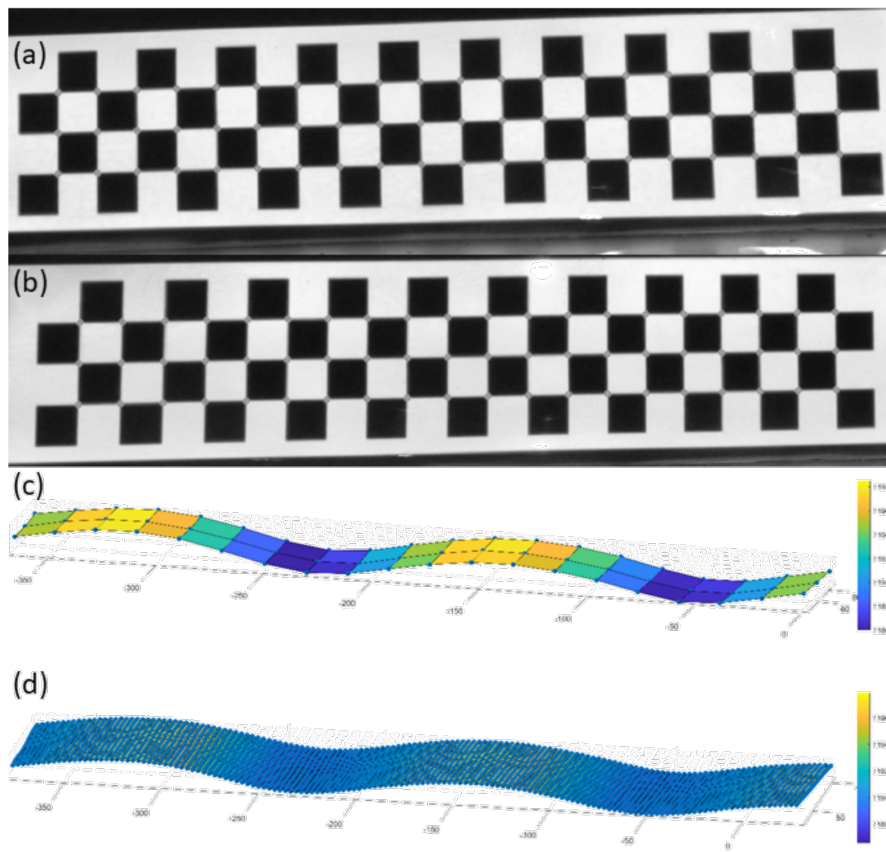
Figure 2.12: Wave measurement outcomes using checkerboard patterns: (a–b) Stereo images and detected feature points; (c) Low-density grid reconstruction; (d) High-density grid reconstruction with improved resolution (Zhao, 2024).
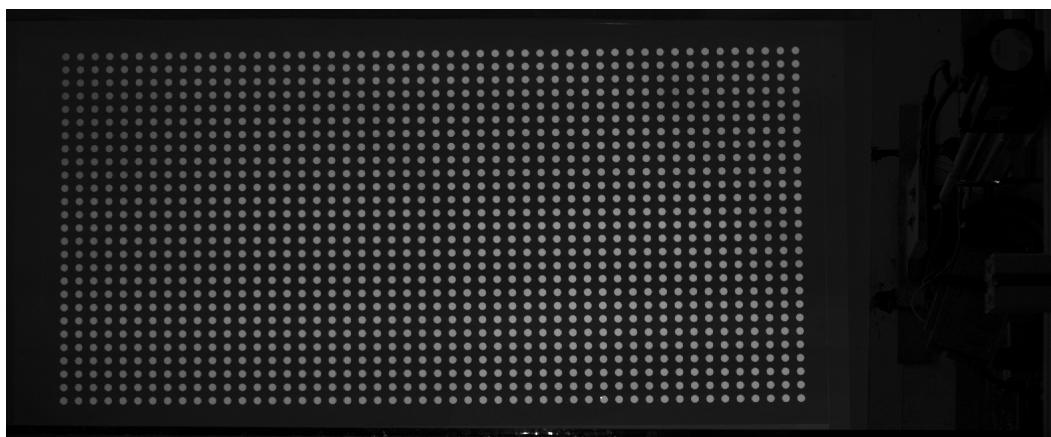
Figure 2.13: Operational dot grid projection covering the desktop flume with 27×50 resolution, enabling orientation-aware wave tracking.

The accumulator space is a three-dimensional space where each point represents a possible circle.

When many edge points vote for a particular set of parameters (a, b, R), indicating that many edge points lie on the circumference of a circle with those parameters, the algorithm detects a circle at that location with radius R.

One of the strengths of the Circular Hough Transform is its ability to detect circles even if they are imperfect or partially obscured, which would be of common occurrence when dealing with water surfaces with complex sub-optimal lighting control conditions.

In our context, this initial step yields two sets of 2D grid positions for each camera. When working with a pair of processed images, the code carries out triangulation using the local positions of the marker centres in each frame, in conjunction with the stereo camera calibration results. This step culminates in a 3D grid position, which represents the current state of the water surface.

In the post-processing of the 2D grid positions, several methodological steps are imperative to ensure accurate triangulation. Upon detection of the centres, there are preparatory measures to be undertaken:

- **Radius Consistency Check**: All markers are presumed to have a quasi-uniform radius. From the detected circles, the mean radius $\bar{R}$ is computed as:

$$\bar{R} = \frac{1}{N} \sum_{i=1}^{N} R_i \qquad (2.35)$$

  where N is the total number of detected circles, and R_i is the radius of the i-th circle. Any circle with a radius that deviates beyond $\pm 20\%$ of this mean (i.e., if $|R_i - \bar{R}| > 0.2\bar{R}$) is deemed inconsistent and is thus excluded from further analysis. This step is crucial to maintain data integrity and to pre-emptively address potential errors, especially those arising from visual anomalies such as dust on the water surface that could be mistakenly identified as a circle.

- **Elimination Based on Hough Metrics**: The Circular Hough Transform assigns a metric M_i to each detected circle, representing the confidence in the detection. Typically, the metrics exhibit a sharp drop-off beyond a certain threshold. By analyzing the distribution of the metrics, we determine a cutoff value M_{cutoff} at the drop-off point. Circles with $M_i < M_{\text{cutoff}}$ are discarded. This ensures that only high-confidence detections are used, and any falsely detected circles exceeding the predefined grid size are systematically eliminated.

- **Grid Alignment for 3D Triangulation**: Given the inherent sequence of the detection process, the 2D grid pairs need to be realigned for consistent 3D triangulation. Initially, the detected centres are grouped by their y-coordinates to categorize them into rows. This can be done by sorting the centres and grouping those with similar y-coordinates. Subsequently, within each row, the centres are organized by their x-coordinates to define the columns. Mathematically, for each centre (x_i, y_i), we define a row index r_i and column index c_i such that:

$$r_i = \text{Round}\left(\frac{y_i - y_{\min}}{\Delta y}\right) + 1, \quad c_i = \text{Round}\left(\frac{x_i - x_{\min}}{\Delta x}\right) + 1 \tag{2.36}$$

  where Δy and Δx are the average vertical and horizontal spacings between the grid points, and $y_{\min}$ and $x_{\min}$ are the minimum y and x values, respectively. The "+1" term ensures that indexing aligns with MATLAB's 1-based array indexing, correcting for the fact that MATLAB counts array positions starting at 1 rather than 0. This meticulous step accounts for potential discrepancies, especially since the detected grid may not be a perfect rectangle.

A notable consideration is the order of these steps. Specifically, the radius check is prioritized to address most errors upfront. Post this check, the predominant residual errors are due to either double detection (the repetitive identification of the same circle) or group detection (where a set of circles is inaccurately detected both individually and collectively).

It's expected that there would be missing target dots under particular experimental conditions, thus the final step of the reconstruction process focuses on compensating for these missing dots. By interpolating the positions of absent target dots based on the spatial arrangement of the detected ones around them, the system can maintain accuracy even when some targets are not captured due to experimental limitations.

Mathematically, missing grid points can be interpolated using neighbouring detected points. For example, if a grid point at position (r, c) is missing, its position can be estimated by averaging the positions of its neighbours:

$$(x_{r,c}, y_{r,c}) = \frac{1}{n} \sum_{(i,j) \in \mathcal{N}} (x_{i,j}, y_{i,j}), \tag{2.37}$$

where $\mathcal{N}$ is the set of neighbouring grid points (e.g., immediate adjacent points that have been detected), and n is the number of such neighbours.

By prioritizing the radius check and systematically addressing subsequent errors, the detection process becomes more robust and reliable across various experimental conditions.

Every de-trended, Gaussian-smoothed elevation record $\tilde{Z}(n)$ is copied and shifted by an integer number of camera frames to further reduced the effect of reflection,

$$D = \left\lfloor \frac{f_s}{f} \right\rfloor, \tag{2.38}$$

where $f_s = 100$ fps is the sampling rate and f the imposed wave frequency. With the lowest test frequency $f = 2.0$ Hz this gives $D = 50$. Up to three shifted copies—matching the three generated crests—are then superposed coherently,

$$Z_{\text{sup}}(n) = \sum_{m=0}^{M-1} \tilde{Z}(n + mD), \qquad M \leq 3, \tag{2.39}$$

so that forward-travelling waves add in phase while the wall-reflected packet, delayed by a round-trip of

$$\Delta n = \frac{2L_{\text{tank}}}{c} f_s, \tag{2.40}$$

appears with an opposing phase and is cancelled. Numerical tests show that the reflected amplitude in Z_{sup} is reduced to below five percent of its value in the raw trace, whereas the incident amplitude is conserved to within experimental uncertainty.

Any residual point anomalies—typically caused by transient glare or bubble interference—are removed by neighbourhood replacement. For a grid node (i, j) flagged as anomalous, the cleaned value is

$$Z_{\text{clean}}(i, j) = \frac{1}{N_n} \sum_{(p,q) \in \mathcal{N}_{i,j}} Z_{\text{sup}}(p, q), \tag{2.41}$$

where $\mathcal{N}_{i,j}$ denotes the surrounding 3×3 window and N_n the number of valid neighbours. This local mean substitution preserves surface continuity without importing energy from outside the immediate vicinity. Together, phase-aligned stacking and anomaly repair ensure that the elevation fields forwarded to the subsequent spectral and structural analyses are effectively free of wall-reflection artefacts.

2.4.3 Results Presentation

After the reconstruction, the next step is to visualize the water surface elevation by creating an animation for each wave condition. The sequence of generating frames for the animation can be summarised as:

- **Computation of Mean Grid Position**: For each axis, the mean grid position is computed using the initial 50 frames (0.5 seconds) as the reference data.

- **Iterative Generation of Surface Plots**: Surface plots corresponding to the grid positions are iteratively generated. Notably, each plot is derived from a set of five consecutive frames.

- **Window Averaging for Smooth Transition**: To mitigate abrupt discrepancies and ensure a smooth visual transition, the data from the aforementioned five frames is averaged prior to plotting.

- **Consistent Visualization Parameters**: Each figure produced adheres to a predetermined aspect ratio, viewing angles, and axis constraints to ensure consistent representation across the data.

- **Video Compilation**: Every individual visual frame, once generated, is stored in a video compilation.

In addition to animation, for each line in the grid parallel to the direction of wave propagation, a temporal surface (or a XTZ surface) is also generated to demonstrate the captured wave propagation. This is especially useful when analyzing the how the underwater structure interact with the surface waves a sequences of examples would be provided in the following chapters.

2.5 Validation of the Reconstruction Code

2.5.1 Static validation experiment

To ascertain the accuracy and reliability of the stereo camera set-up and the reconstruction code, it is crucial to conduct a validation of the processed results. This validation serves a dual purpose: it not just exposes the limitations of the current hardware and software but also verifies the robustness of the methodology for laboratory deployment.

Two types of validation tests were carried out multiples times. First is the reconstruction of a 3D calibration target and then the reconstruction of a still water surface which is a less extreme scenario more similar to water wave test conditions. The first validation process employed a LaVision 3D calibration plate, which is designed specifically for multi-dimensional strain experiments. The plate features a precise high-contrast dot pattern and two distinct vertical levels, separated by a 2mm step. The use of this calibration plate allows for accurate stereoscopic verification. The tilt-shift lens used in the stereo setup further enhances accuracy by eliminating the need for distortion correction, which is typically required in standard industrial lenses. By bypassing distortion correction, the system enables a more straightforward and accurate point mapping between the detected points and the pre-set grid.

To validate the accuracy of the reconstruction code, the calibration plate was captured 500 times, and the images were 3D-reconstructed using the stereo system. The reconstruction process involves comparing the detected points on the plate (represented as red dots) with the pre-set grid (green dots) based on the known layout of the calibration target, as shown in Figure 2.14.

(a)   (b)   (c)
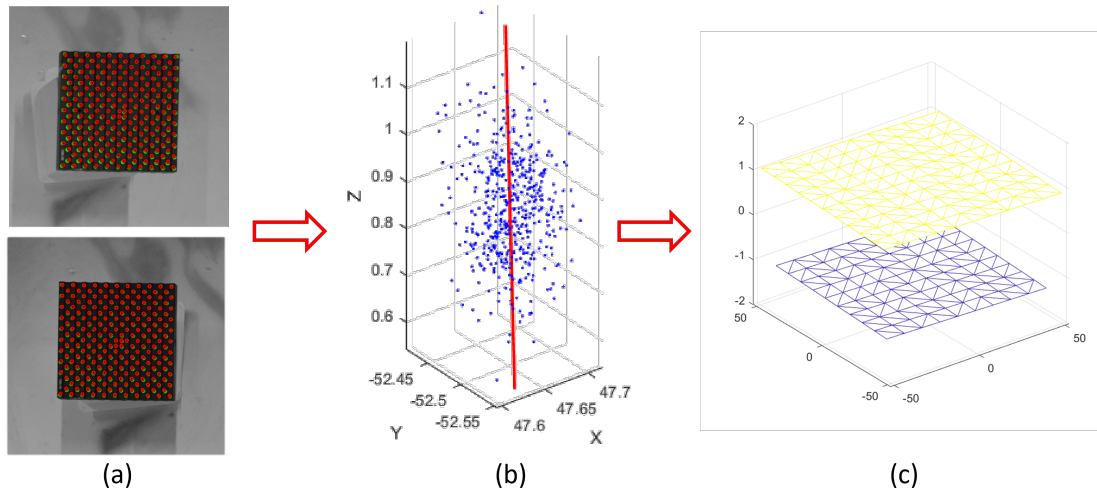
Figure 2.14: An overview of the validation process and results (a) La-Vision 3D calibration plate, (b) the reconstruction results of a single point on the edge of the higher level of the plate of the plate and the reconstruction results of (c) the whole plate with the two layers. The reconstructed results clearly demonstrates a ellipsoidal shape, suggesting tight accuracy in horizontal axes while suffering from a relatively poor vertical resolutions

The validation experiment demonstrated that the system performs exceptionally well in reconstructing points in the horizontal plane ($\mathbf{XY}$ plane), with a relative error of less than $\pm 0.05mm$. However, as expected in such a challenging scenario, the vertical axis ($\mathbf{Z}$ axis) exhibited an initial relative error of up to $\pm 0.25mm$. Through data averaging across the 500 frames and excluding outliers, the relative error in the vertical axis was reduced to approximately $\pm 0.065mm$, as seen in Fig. 2.14 (c), the averaged out results still distinguish the 2 mm gap between the top and bottom levels.

This setup and methodology provide a thorough test of the stereo system's capabilities. The extreme challenge of detecting such a small vertical difference (2mm) at a large distance (2 meters) highlights both the strengths and the limitations of the system.

Overall, this validation process confirms that the stereo camera setup and reconstruction code are robust and capable of achieving high accuracy, particularly in the horizontal plane, while some improvement in vertical depth resolution is required. This rigorous validation demonstrates the reliability of the system for use in laboratory environments, even under extreme testing conditions.

In addition to using the 3D calibration plate, the precision and reliability of the reconstruction code were put to test using a dataset of 500 frames capturing a static water surface. The calculated relative and absolute errors included metrics such as the surface's mean roughness, denoted by R_{ms}, and its mean curvature, represented by K. This process simulated a semi-testing condition, wherein no waves were generated, but the cameras remained positioned with the tank filled to its testing water level.
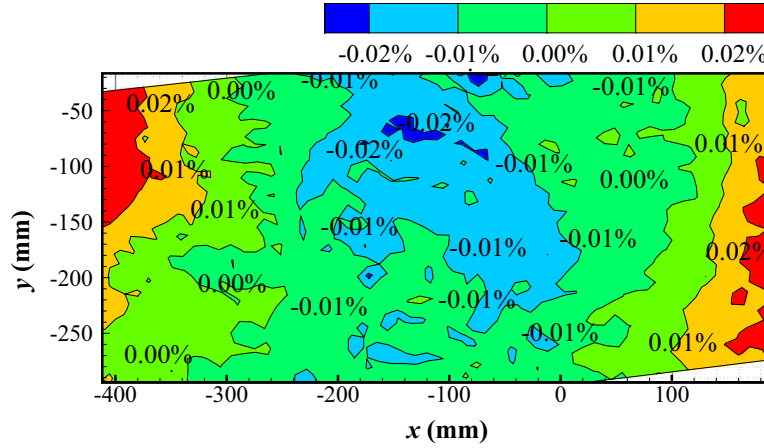
Figure 2.15: The contour of the reconstructed still water surface

Figure 2.17 shows the relative error of the reconstructed water surface normalised by the distance between the cameras and the water surface. The relative error is sufficiently small at a maximum approximately ± 0.02 %.

The surface mean roughness and mean curvature are also calculated. The surface mean roughness R_{ms} is calculated at 0.2 using the root mean square of the surface height deviations from the mean plane:

$$R_{\mathrm{ms}} = \sqrt{\frac{1}{N} \sum_{i=1}^{N} (z_i - \bar{z})^2}, \tag{2.42}$$

where z_i is the height of the i-th point on the reconstructed surface, $\bar{z}$ is the mean height of the surface, and N is the total number of points.

The effective mean curvature K is calculated using the average Gaussian curvature over the entire surface. For a surface defined by $z = f(x, y)$, the Gaussian curvature at each point is given by:

$$K = \frac{f_{xx} f_{yy} - f_{xy}^2}{\left(1 + f_x^2 + f_y^2\right)^2}, \tag{2.43}$$

where f_x and f_y are the first partial derivatives, and f_{xx}, f_{yy}, and f_{xy} are the second partial derivatives of f with respect to x and y. In this case, since the reconstructed surface is essentially flat, the partial derivatives are negligible, leading to an effective curvature K of approximately

zero.

With the use of a tilt-shifting lens that ensures the entire water surface is in focus, the majority of the error is located around the top left and bottom right corners of the captured water surface. However, their values are very small, at a level of 0.02% in relative error, and thus have a negligible effect on the overall reconstruction. The results effectively depict the flatness of the still water surface.

The measurement of two-level calibration plate and still water surface provide enough confidence in the stereo camera setup to continuing to the next phase of experiment.

Table 2.2 summarizes the mean reprojection error and the resulting spatial accuracies in both the virtual and the experimental environments.

Table 2.2: Comparative Accuracy in Virtual and Experimental Environments

Environment	Reproj. Error (px)	XY Acc. (mm)	Z Acc. (mm)
Virtual	0.0365	± 0.02	± 0.05
Experimental	0.056	± 0.05	± 0.065

In summary, the physical measurement approach exhibits only slightly higher reprojection errors and spatial uncertainties compared with the virtual calibration, which represents the theoretical limit of the method. This close alignment between experimental and simulated performance confirms the reliability of the stereo-vision system, demonstrating its suitability for precise free-surface reconstructions in laboratory settings.

2.5.2 Dynamic validation experiment

While the still water surface and LaVision 3D calibration target reconstruction results demonstrate the accuracy and robustness of the stereo camera set up in a static setting, it's also important to provide the validation in a dynamic setting against a known theoretical wave profile.

The solid sinusoidal wave profile is created in 3D modelling software Rhino with a wave length of 20π mm and an amplitude of 2π mm, the solid wave is extended in both horizontal direction to generate a solid wave surface as shown in Fig. 2.16a. To provide a flat base, the outer boundary of the wave profile surface (a 188.5 mm square) was extruded down to a reference plane 11 mm below the top plane.

The model was 3D printed and coated with a thin layer of reflective paint to enhance optical return while preserving geometry (Fig. 2.16b).

For motion, the solid wave profile was mounted on a linear rail driven by a stepper motor, enabling translation at constant speed. An Arduino Nano controlled the motor to maintain 10 mm/s. The stereo cameras were fitted with 70–200 mm zoom lenses and positioned at a
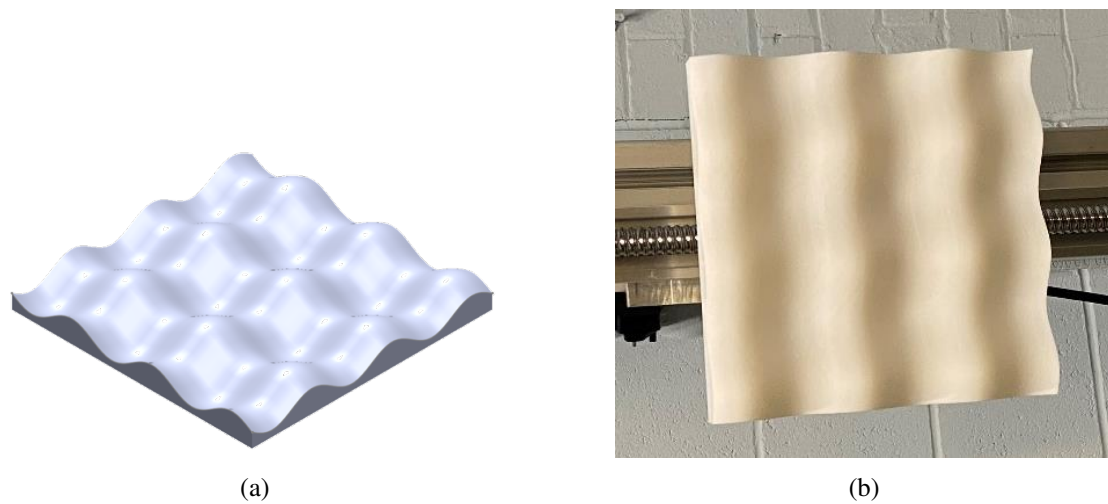
Figure 2.16: Solid sinusoidal wave profile model in (a) modelling software render and (b) 3D printed in deployment.

comfortable distance to minimise vibration coupling from the drive.
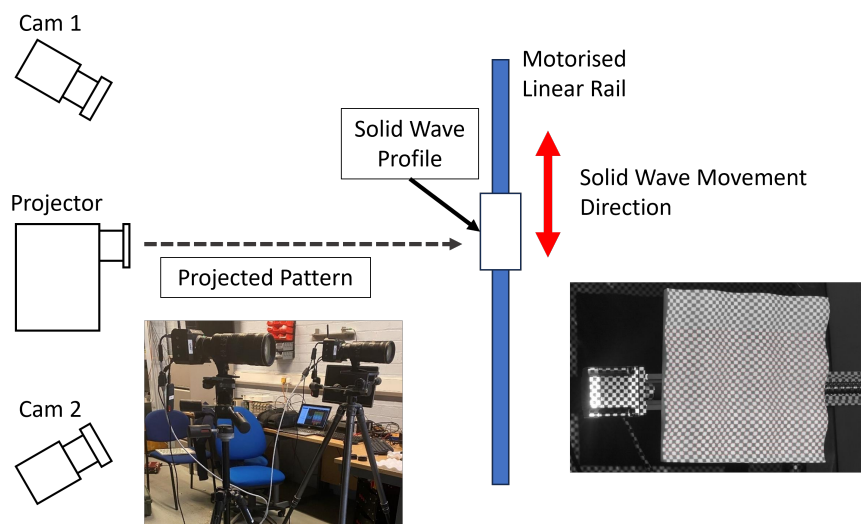
Figure 2.17: Experiment setup for the dynamic reconstruction of a solid sinusoidal wave profile with a snapshot of the projected pattern during experiment and the camera set-up.

Figure 2.18 shows a representative frame during translational movement, comparing theoretical points (solid black) with reconstructed measurements (open blue).

The results suggests a maximum deviation of ± 0.065 mm in horizontal XY plane, on par with the extreme static test conducted with LaVision 3D calibration target.

In the vertical direction, a maximum absolute deviation of ± 0.35 mm was observed (Fig. 2.19a). Given the amplitude $A = 6.28$ mm (wave height $2A = 12.56$ mm), this corresponds to $\approx 5.6\%$ of amplitude (i.e. $\sim 94\%$ accuracy).

To better quantify the performance of the stereo camera system in a dynamic situation,
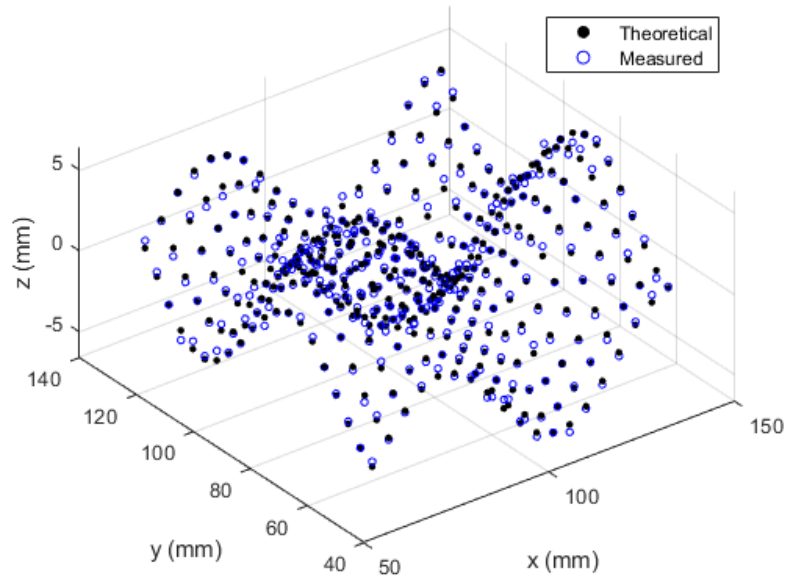
Figure 2.18: Experiment results withe the reconstructed solid wave (in hollowed blue dots) and its theoretical value (solid black dots).

especially in vertical plane in a temporal setting, a single dots on the projected plane was selected to track it's vertical movement along the solid wave profile as the solid wave model is moving along the target area at a constance velocity (10mm/s as mentioned above). As shown in Fig. 2.19c, the stereocamera can accurately capture the vertical movement of the projected point with maximum absolute deviation of 0.46 mm, which translates to a 93% overall accuracy rate for capturing a moving solid wave profile.

Taken together, the static and dynamic tests show that the stereo system achieves in–plane accuracies of order ± 0.05–0.065 mm and depth accuracies up to ± 0.35 mm under translation at 10 mm/s, while preserving the expected frequency content of a sinusoidal profile with amplitude 6.28 mm. The dynamic results are on a par with the static plate benchmark in XY and within 5–7% of amplitude in Z, which is adequate for the laboratory free–surface measurements targeted in this work. Residual depth sensitivity and peripheral degradation are consistent with the optical geometry and can be mitigated by modest temporal averaging and conservative cropping of boundary regions.

2.5.3 Comparison with conventional wave elevation measuring equipments

Direct, co-located validation against a resistance probe was not feasible in the desktop flume for the following reasons:

(i) *Intrusiveness and capillarity*: the 1–3 mm rods and their mount create local scattering and

(a)

(b)

(c)
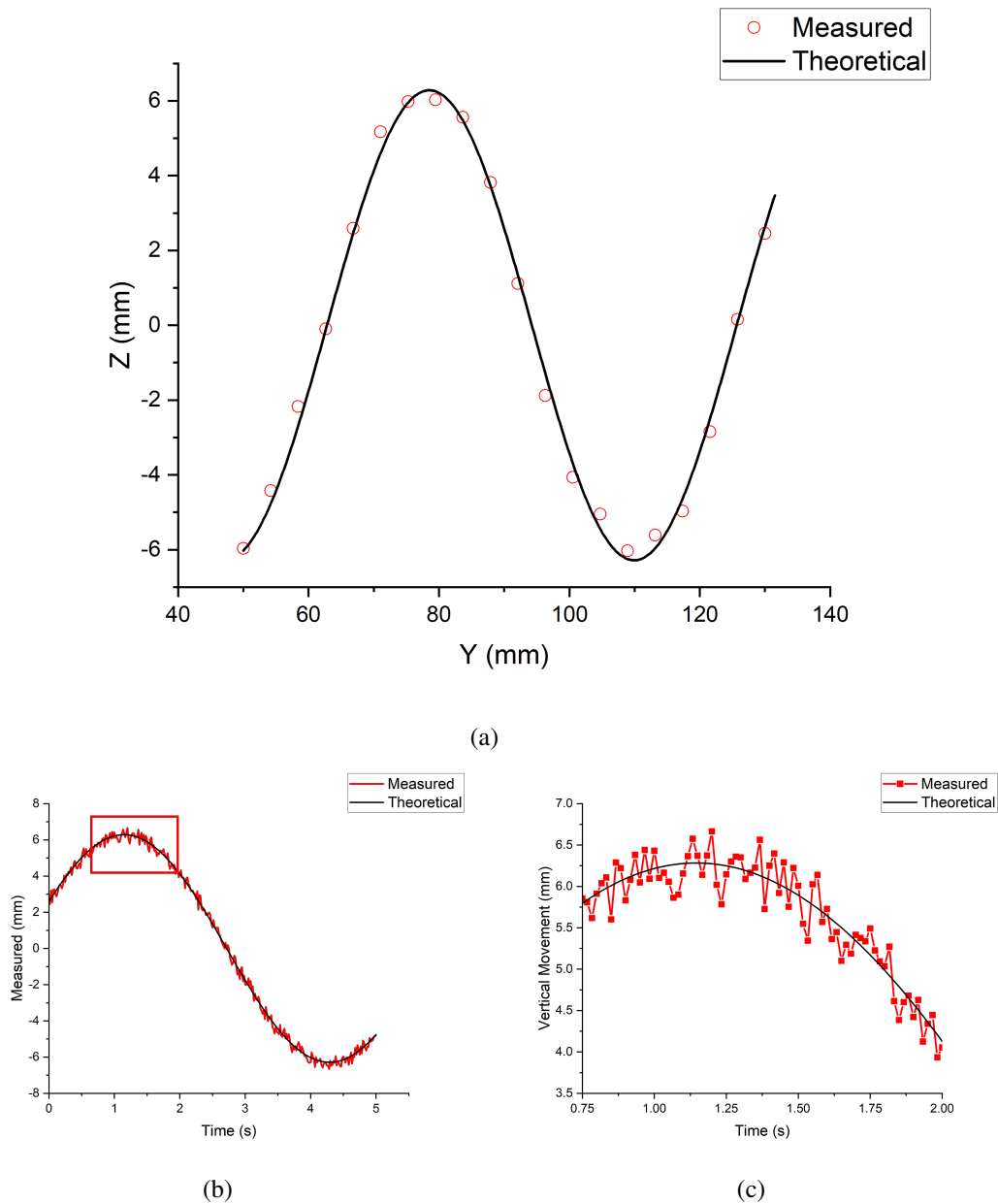
Figure 2.19: Solid sinusoidal wave profile model reconstruction results compared with theoretical model by (a) taking a line of points along the Y axis and plot their Z value to compare with theoretical model and (b) taking a vertical time history of single captured point as the solid wave profile is moving in the target area, with the zoomed-in view of the selected section within the red square in (c).

a meniscus whose bias is of the same order as the millimetre-scale elevations studied.

(ii) *Optical incompatibility*: the probe and leads introduce specular glare/occlusions that disrupt stereo correlation, while the micro-bubble tracer layer used to raise surface albedo adheres to the electrodes and destabilises the conductivity reading.

(iii) *Geometric constraints*: the narrow test section does not allow the probe to be placed with adequate wall clearance without entering the metamaterial field and perturbing it.

(iv) *Shallow regime*: test depths were $< 10\,\text{cm}$ with wave heights $< 3\,\text{mm}$; in this regime the probe's rod diameter and meniscus are $\mathscr{O}(\eta)$, so deployment would perturb the flow and bias the reading, making a valid comparison impractical.

Nevertheless, prior work has directly compared optical stereo-vision free-surface reconstructions with both resistance and ultrasonic wave probes under bench-scale conditions in the 3D compact wave tank of the Kelvin Hydrodynamic Laboratory with a water depth of 1.0 m. (Zhao, 2024).

Subsequently, a comparison of results obtained through these distinct measurement techniques revealed a satisfactory degree of concordance.

The resulting maximum absolute error was 0.384 mm, well within the 95% confidence intervals of the three instruments (resistance: ± 0.571 mm; optical: ± 0.205 mm; ultrasonic: ± 0.490 mm). At higher amplitudes, the largest discrepancy occurred between the ultrasonic probe and the optical method (0.91 mm), yet it remained below the combined 95% limit (1.061 mm). Importantly, the system-level error attributable to calibration and camera characteristics was bounded and showed no growth with wave height (shown in Fig. 2.20).

(a)   (b)
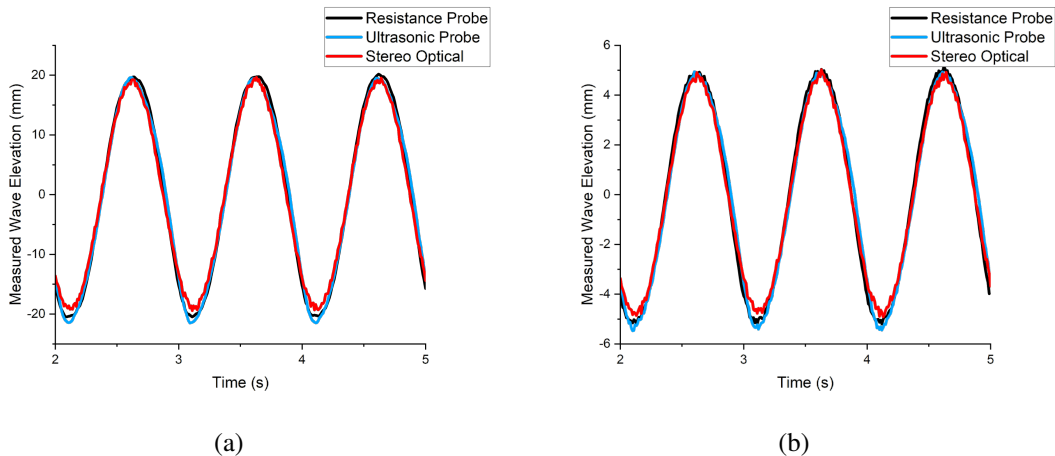
Figure 2.20: Direct comparison results processed from earlier work in (Zhao, 2024) conducted in the KHL 3D compact tank with a wave frequency of 1 Hz, an input amplitude of 20 mm in (a) and 5 mm in (b)

A more detailed error analysis of each measurement system is shown in Tab.2.3 including

the RMSE analysis of each physical values. Across all systems the period/frequency results are essentially identical with high temporal accuracy.

The stereo optical method performs on par with the conventional probes—showing a minor negative bias and an uncertainty comparable to the resistance probe.

Table 2.3: Comparison results of the three measurement systems with a Wave frequency of 1 Hz with an input amplitude of 20 mm (Zhao, 2024)

Mean Value and RMSE	Resistance Probe	Ultrasonic Probe	Stereo Optical Method
Period (s)	0.999	1.000	0.998
Period RMSE (s)	0.000	0.000	0.000
Frequency (Hz)	1.000	0.999	1.001
Frequency RMSE (Hz)	0.000	0.000	0.000
Amplitude (mm)	20.030	20.450	19.650
Amplitude RMSE (mm)	0.032	0.039	0.049

Additional tests with known moving distance were also conducted to further quantify the performance of the three measurement system, by measuring a series of known distance from 4.00 to 28.00 mm. As demonstrated in Tab. 2.4, the maximum absolute errors were 0.419 mm (ultrasonic), 0.185 mm (resistive), and 0.322 mm (optical).

Table 2.4: Different wave measurement set ups with a series of known distance (Zhao, 2024)

Known Distance (mm)	Ultrasonic Probe (mm)	Resistance Probe (mm)	Stereo Optical Method (mm)
4.00	4.42	4.05	4.24
8.00	7.65	8.10	8.10
12.00	11.82	11.89	11.84
16.00	16.21	16.18	16.14
20.00	19.92	20.03	20.10
24.00	23.81	23.98	24.03
28.00	28.33	28.18	28.32

In conclusion, the stereo optical method performs on par with the conventional probes and is suitable for deployment.

2.6 Quasi-Real-Time Preview Mode

While the current version of the reconstruction code is accurate and efficient enough for deployment, it lacks a real-time preview feature. Adding such a feature, a quasi-real-time mode, is critical for previewing or demonstrating the reconstruction process interactively.

This section describes the methods and modifications enabling a preview mode that operates at

10 frames per second (10 Hz), achieving a balance between processing speed and computational accuracy. The preview mode integrates a series of on-the-fly computations, reducing the reliance on post-processing and allowing for near-instantaneous feedback.

The quasi-real-time system diverges from the conventional method by directly processing frames as they are captured, rather than storing them for later. Using a dual-camera setup, the script initializes parameters, sets exposure times, and configures triggering protocols for synchronous frame capture. Each captured frame pair is subsequently processed to estimate the 3D positions of markers, providing an initial preview surface.

The first pair of frames undergoes a circular Hough transform, leveraging the `imfindcircles` function with a specified diameter range and sensitivity threshold. The Hough transform locates the circular markers by maximizing intensity gradients within a specified radius range, providing accurate marker centres. Mathematically, this detection process solves for circle parameters (x_0, y_0, r) that satisfy:

$$(x - x_0)^2 + (y - y_0)^2 = r^2 \tag{2.44}$$

where x and y are pixel coordinates, and r is the circle radius. This process establishes local origins and principal axes, which are essential for aligning subsequent frames.

To achieve the 10 Hz frame rate, subsequent frames avoid the computationally intense Hough transform, instead relying on binarization and morphological operations to extract marker positions. For each new frame pair, pixel values above the mean intensity are set to one (white), while lower values are set to zero (black), yielding a binary image. This binarization step can be described as follows:

$$B(x,y) = \begin{cases} 1 & \text{if } I(x,y) \geq \text{mean}(I) \\ 0 & \text{otherwise} \end{cases} \tag{2.45}$$

where $B(x,y)$ is the binarized pixel value, and $I(x,y)$ represents the original intensity. The MATLAB script further cleans the binary image through morphological closing to eliminate small gaps.

Elaborating further, the algorithm first singles out pixel values in an image exceeding the overall average.This action morphs the image into a binary format where luminous pixels depict regions where original image values surpassed the mean value. Subsequently, any minuscule voids introduced by the binarization are sealed using a morphological closing procedure. The next phase involves computing the centres of each luminous segment in the binarized image, converting this data into a 2D array primed for triangulation.

Each frame pair (comprising 1230 markers) requires approximately 0.08 seconds to process,

from image capture to surface mesh update, achieving the target preview rate of 10 Hz. This quasi-real-time approach provides a functional preview of water surface reconstructions in demonstrations or dynamic settings, where a swift overview is prioritized over absolute accuracy.

This approach to achieving a quasi real-time preview of water surfaces represents a harmonious compromise between computational speed and accuracy. The method is particularly apt for scenarios where a rapid preview or live demonstration is more crucial than granular detail.

2.7 Discussion on the Performance and Possible Further Improvement

In the previous section, various segment regarding the 3D water surface reconstruction code was discussed in detail. In the following section, the main focus will be turned to the performance of the reconstruction code in terms of computational load, how it compare with the other techniques used to measure the water surface elevation and what's the codes' limitation, potential used case, and future improvement.

Understanding the computational efficiency is crucial for predicting the code's performance for possible real-time application. . In its present form, the code is designed to handle high-resolution images at a rate of 100 FPS, posing substantial computational challenges. Processing a typical data set with 500 pair of frames each with 1230 projected markers using a custom-build workstation with AMD 5950x 16 core CPU and 96GB of high-speed DDR4 memory took roughly 600-700 seconds, which is a significant improvement compared with using projected checkerboard that can require up to 15 minutes per single pair of frames using a similar workstation.

Conventionally in the laboratory setting, the water surface elevation has been measured using various kinds of wave gauge utilizing different basic principle. A resistance based wave gauge or ultrasonic wave probe, for example, provide high temporal resolution with real time monitoring but has limited spatial coverage. Effort to overcome the gauges' spatial coverage would drastically increase the number of wave gauges, potentially crowding valuable test space. Intrusion of the water surface caused by closely placed resistance wave gauge may have a negative effect on the results.

In contrast, the stereo-camera-based approach captures the spatial dynamics of the water surface using simultaneous measurements of multiple points over a wide area, showcasing the intricate wave interactions and propagation patterns across the testing surface. Cost-wise, this method outperforms an array of ultrasonic probes and is unburdened by the typical 30cm dead-zone constraints.

It's also important to point out that while the previous section only demonstrated reconstruction results of a rectangle gird pattern, the stereo-camera can also seamlessly capture irregular grid pattern, making it suitable for measuring "complex" water surface both inside and outside a oscillating water column or slashing in a moonpool.

The stereo-camera technique is not devoid of limitations. One limitation of the current code lies in its reliance on the computational intensive of the Hough transform. The computational load, especially when searching for circles of varying radii or when the image resolution is large thus making it difficult to achieve real-time monitor.

Moreover, the code's current utilization of parallel computing requires large amount of random access memory (RAM), a data set of 500 pairs of frames need 45GB of high speed RAM to temporally store the data during processing thus the capture time is limited to under 10 seconds or 1000 frames pairs.

Beyond the laboratory setting, the reconstruction code holds potential for several applications. It can be adapted for monitoring natural water bodies, such as lakes or coastal areas, providing valuable insights into wave dynamics, shoreline erosion, or sediment transport. Additionally, with modifications, the code can be employed in industrial applications, such as monitoring liquid surfaces in storage tanks or assessing flow dynamics in open channels.

Transitioning the computational workload from CPUs to GPUs might alleviate processing bottlenecks. Such a transition could substantially elevate the code's performance, making it suitable for near-real-time applications or much larger data set.

Looking ahead, several improvements can be incorporated into the code. Implementing machine learning-based circle detection algorithms might offer more robust and efficient performance compared to the Hough transform that's in the current code. Additionally, by integrating adaptive algorithms, the system can re-calibrate in real-time, compensating for any drift or change in the camera positioning.

Furthermore, the code can benefit from implementing algorithms that can filter out or correct for ambient disturbances, like reflections or shadows. This would bolster the system's reliability in diverse lighting conditions, expanding its utility in outdoor or dynamic environments.

In conclusion, while the current version of the 3D water surface reconstruction code demonstrates promising performance, there remains ample room for enhancements. Embracing modern computational tools and techniques, continuous refinement, and drawing insights from real-world deployments will be essential in realizing its full potential.

2.8 Conclusion

In this chapter the development and validation of a novel experimental system for the investigation of water wave propagation, with particular emphasis on wave-metamaterial interaction has been explained in great detail . The system comprises a desktop-sized wave flume equipped with a stepper motor-driven plunger wave maker, a stereo vision system for 3D water surface reconstruction, and a streamlined calibration and data processing methodology.

The stereo vision system, which employs high-resolution industrial cameras with tilt-shift lenses, provides accurate and detailed measurements of water surface elevation, overcoming the limitations of traditional wave probes and optical shadowgraph techniques. These lenses offer superior control over focus and distortion, ensuring high-fidelity image capture crucial for accurate 3D reconstruction. The system's performance was rigorously validated through both virtual experiments, conducted using the Blender software package, and laboratory tests, demonstrating its accuracy and robustness even under challenging conditions.

Furthermore, the development of a quasi-real-time preview mode enhances the system's usability, allowing for immediate visualisation and feedback during experiments. This feature proves particularly valuable for demonstrating wave phenomena and facilitating rapid adjustments to experimental parameters.

Whilst the current system exhibits excellent performance, potential improvements have been identified, including the exploration of GPU-accelerated computation and the integration of machine learning algorithms for enhanced efficiency and accuracy. Such advancements will further solidify the system's position as a powerful tool for investigating water wave dynamics and metamaterial behaviour.

The experimental apparatus and measurement system described in this chapter provide a robust and versatile platform for the experimental investigations presented in the remainder of this thesis. The accurate and detailed measurements obtained through this system will enable a deeper understanding of water wave manipulation and the potential applications of metamaterials in coastal and offshore engineering.

Chapter 3

Rapid Demonstration of Water Wave Metamaterials in a Desktop-Scale Stereo Vision Measurement System

This chapter introduces a water-wave metamaterial demonstration system capable of rapid experimental assessment of designs, overcoming limitations of earlier methods through more accurate and comprehensive wave-field measurements. The current state of the art in metamaterial research and the role of desktop-scale apparatuses for swift demonstration are first outlined (Section 3.2). Experimental results are then detailed (Section 3.3), including two case studies: (i) interaction of a single wave with a channelled spherical-cut metamaterial under varying water depths, and (ii) exploration of basic geometric shapes to evaluate their focusing or refracting properties as candidate unit cells for future designs. The chapter concludes with a summary of the system's effectiveness and prospects for accelerated water-wave metamaterial development (Section 3.7).

3.1 Background

Metamaterials are artificially engineered materials designed to exhibit properties not found in naturally occurring substances. The term *metamaterial*, originating from the Greek word *meta*, meaning "beyond," was first used in the field of optics to describe artificial electromagnetic media crafted with structures on a sub-wavelength scale. These materials consist of arrays of small structures meticulously engineered to manipulate electromagnetic waves in ways that transcend conventional limitations. They offer optical qualities such as negative refraction, superlensing, and cloaking, controllable down to length scales smaller than the wavelength of light, making light appear to break conventional rules.

The initial breakthrough in metamaterials was the development of materials with a negative refractive index. In all known natural materials, incident and refracted light rays lie on opposite

sides of the normal line at the interface, following Snell's law with positive indices of refraction. Shelby et al. (2001) demonstrated that by constructing a device with square copper split-ring resonators and copper wire strips on fibreglass circuit boards, they could create a material where a microwave beam is refracted on the same side of the normal as the incident beam. This means the microwave bends in the opposite direction compared to how it would in natural materials, effectively exhibiting a negative refractive index. This finding showcases the capability of engineered materials to demonstrate properties not found in nature, ushering in novel technological opportunities.

The ability of metamaterials to control the propagation of electromagnetic waves has led to numerous applications. One notable application is *cloaking*, where metamaterial structures can guide light waves around an object, rendering it invisible to certain types of detection by redirecting the light around it (Pendry et al., 2006; Schurig et al., 2006). Another application is in *superlensing*, where metamaterials are designed to create lenses with resolutions beyond the diffraction limit, which is particularly useful in fields like microscopy and nanotechnology. Metamaterials are also used in microwave and antenna engineering to create compact and efficient antennas, and in energy-harvesting structures that efficiently convert electromagnetic radiation into usable electrical energy.

Fundamentally, metamaterials are distinguished by their capacity to control wave propagation through the precise design of their shape, geometry, size, orientation, and arrangement. The fundamental theories for designing optical metamaterials were proposed by Pendry et al. (2006) and Leonhardt (2006). Pendry et al. introduced a theory based on coordinate transformations of Maxwell's equations under the Galileo transformation, while Leonhardt proposed the *Optical Conformal Mapping* theory to simplify anisotropic properties, focusing on inhomogeneity. Both theories involve designing transformation media's constitutive parameters—permittivity and permeability—while keeping the governing equations of electromagnetic waves unchanged. With appropriately designed medium structures and properties, these constitutive parameters produce localized spatial variations that make waves propagate in a designed manner.

Early in 1967, Lighthill presented a visual summary of the different types of waves in fluids and their interrelationships, as shown in Fig. 3.1. This diagram illustrates that electromagnetic waves, acoustic waves, and water waves are all types of waves that propagate in fluids.

The success of optical metamaterials has inspired researchers to adopt similar design principles in other fields, such as acoustics and hydrodynamics. Acoustic metamaterials emerged around 2007 and have since seen a significant increase in research activity, with hundreds of papers published annually. However, the development of metamaterials for water waves is still in its
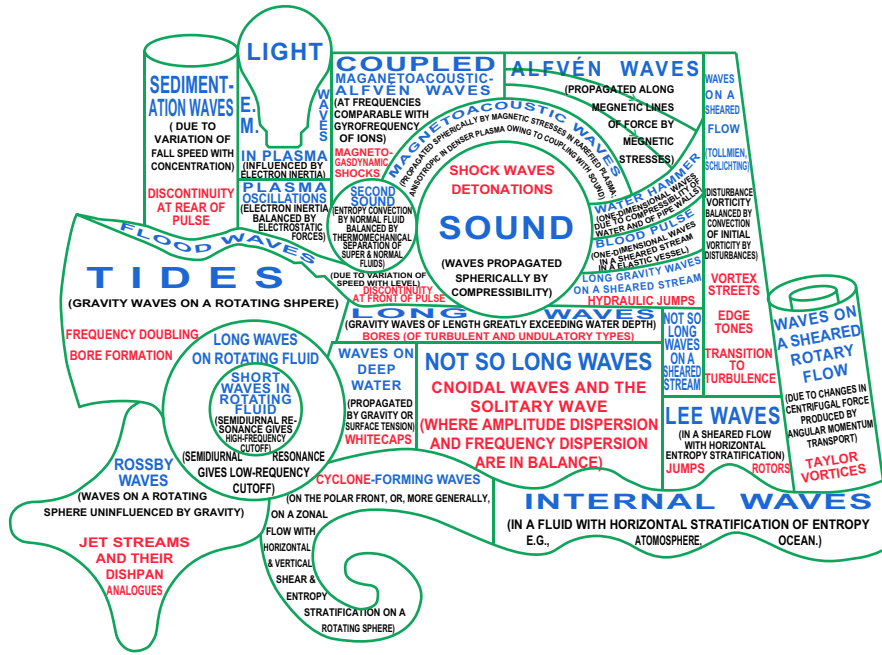
Figure 3.1: Waves in fluids. Blue labels are the names of the wave systems. Black text provides explanatory remarks on the waves. Red text highlights key effects of the wave systems' nonlinear properties (Lighthill, 1967).

early stages. Unlike electromagnetic waves, which are transverse, and acoustic waves, which are longitudinal, water waves involve a combination of both longitudinal and transverse motions. This unique characteristic presents challenges when applying general design principles to water wave metamaterials.

In analogy to the transformations of permittivity and permeability in electromagnetic metamaterials, controlling water waves would require spatial variation of parameters like water depth and gravitational acceleration along the wave path. While altering gravitational acceleration is not feasible (Zareei and Alam, 2015), researchers have nonetheless managed to design metamaterials that can manipulate water waves.

Researchers have proposed several approaches to design metamaterials that control the propagation of water waves. This chapter focuses on three principal methods:

- Using structured bathymetry to control the wave propagation speed and direction.

- Applying transformation optics principles to the design of water wave metamaterials.

- Utilizing the scattering cancellation method.

3.1.1 Structured Bathymetry

One approach is to use structured bathymetry to control wave propagation. In shallow water, the speed of surface waves can be controlled by varying the seabed topography, as indicated by the

dispersion relation for shallow water waves. Zou et al. (2019) demonstrated that a gradient depth profile on the bottom of a water channel can achieve broadband cloaking. Their design creates a gradient-index metamaterial that converts incident plane water waves into waveguide-trapped waves. The waves propagate mainly over the waveguide instead of a wider water surface and are converted back to plane waves at the end of the waveguide. This approach achieves cloaking without any structures on the water surface.
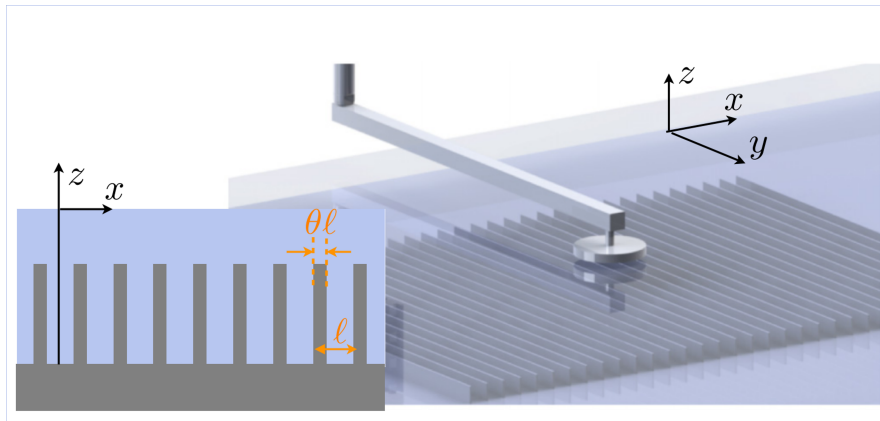
Figure 3.2: An illustration of a metamateiral design based on structured bathymetry to achieve reflectionless waveguide proposed and examined by Maurel et al. (2017)

By repeating this structure with alternating grooves and ridges at the bottom of the water, the metamaterial can function as a reflectionless bent waveguide. Berraquero et al. (2013) and later Maurel et al. (2017) developed a wave shifter using this kind of metamaterial and demonstrated its efficiency experimentally. Their design uses a structured bathymetry with subwavelength rapid abrupt fluctuations in depth to shift the water wave in the direction of the waveguide (illustrated in Fig. 3.2).

A theory based on multiscale homogenization of shallow water equations was developed by Marangos and Porter (2021) to find the effective water depth tensor components and predict complex wave propagation characteristics. This approach allows for the design of metamaterials that can control wave propagation through variations in water depth.

3.1.2 Transformation Optics Principles

Another approach involves applying transformation optics principles to design water wave metamaterials. These metamaterials are analogous to designs in the field of electromagnetic waves because they implement similar design principles. Zareei and Alam (2015) proposed a theory that requires only a change in water depth to achieve a nonlinear transformation for water waves, connecting transformation optics and shallow water waves. Farhat et al. (2008) proposed a structured metamaterial to create artificial anisotropic properties of a fluid, using homogenization

theory to match their theoretical model with simulations in a water wave cloaking example.

Iida and Kashiwagi (2018) proposed a design formula for a small water channel network that can attain water wave cloaking, derived from an analogy between waves in a water channel and electric waves in an LC circuit. Their anisotropic network model provides another explanation for the design of Farhat et al. (2008) to cloak a cylinder. Dupont et al. (2016) also proposed a method to construct metamaterials that can cloak a cylinder in water waves using conformal mapping, reducing the drift force applied to the cylinder.

Park et al. (2019) studied viscous forces with coordinate transformation of fluidic space in a metamaterial design around a cylinder, demonstrating that a cloaking metamaterial can achieve drag-free conditions with anisotropic mapping of viscosity.

3.1.3 Scattering Cancellation Method

A third approach in developing water wave metamaterials is to use the scattering cancellation method. Wave interference is used here instead of changing the water depth, which is particularly important in deep water where variations in water depth have little impact on wave propagation. Newman (2014) found that multiple cylinders arranged in a circle can cloak one cylinder at the centre. Zhang et al. (2020) demonstrated that as few as eight cylinders can manipulate scattered waves to achieve concentrating and invisibility effects in water waves.
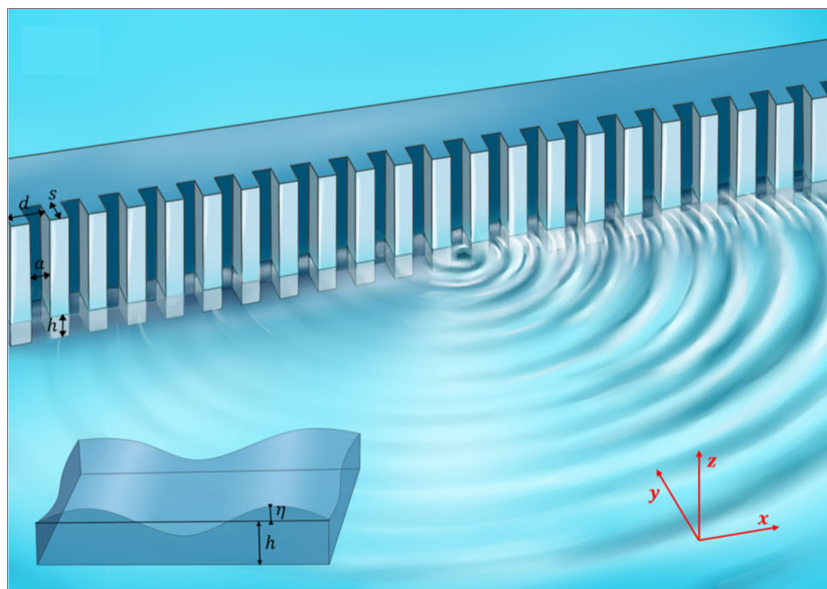
Figure 3.3: An illustration of a metamateiral design based on Scattering Cancellation Method to achieve water polariton where the structure change the propagation of surface water waves Han et al. (2022).

Using elastic plate rings floating on the water surface around a cylinder, Iida et al. (2023) presented the cloaking of a bottom-mounted cylinder from water waves. Their cloaking structure,

consisting of four or more rings with a diameter greater than three times that of the cylinder, significantly reduced the wave drift force with appropriate ring rigidity.

Han et al. (2022) discovered that a one-dimensional groove array can direct water waves in one direction by exciting unidirectional surface polaritons on the water surface. Porter (2021) explored a metamaterial design using thin parallel plates that extend above the water surface. The channels between the plates form a waveguide that confines water waves propagating within it, acting as a perfectly transmitting negative-refraction metamaterial. Li et al. (2018) combined this kind of plate waveguide with depth-profiled bathymetry to develop annular concentrators that manipulate water waves with concentrating and invisibility effects.

3.1.4 Challenges and Opportunities

These approaches demonstrate the potential of water wave metamaterials in controlling wave propagation for applications such as cloaking, drag reduction, and wave scattering. They form the foundation for various applications, including harbour and coastal asset protection and ocean wave energy harvesting in harsh environments. Other techniques on wave manipulation, such as the wave-passing effect observed in ducklings' swimming (Yuan et al., 2021), may also be incorporated into future metamaterial designs.

In existing metamaterial studies, the focus is mainly on the design of water wave metamaterials. Experimental validations are primarily based on optical shadowing techniques, methods that project light into the water and record brightness changes due to the curvature of the water surface. While these methods can provide qualitative results about wave propagation, they cannot measure the absolute wave height in experiments. Another method uses multiple wave probes in a wave tank to measure wave heights at limited positions.

The currently stages of experimental demonstrations presents a unique opportunities to provide an novel all-in-one experimental apparatus that addresses the pain-points while remaining cost-effective and relatively easy to implement.

3.2 Experimental setup and data processing

The desktop water wave metamaterial demonstration system includes both the experimental setup and data processing. The experimental setup allows for a quickly building of water wave metamaterials and testing their performance in waves, while the data processing provides precise results from the experimental data. The combination of these two components makes it possible to rapidly test and refine their designs, ensuring the designs of the water wave metamaterials are effective and efficient in water wave manipulations. Given that the desktop wave flume has been

extensively discussed in the previous chapter, the following description will focus on the fast prototyping system and the experimental procedure.

3.2.1 Fast Prototyping System

An integral component of our experiment apparatus is the FDM 3D printer (Anycubic Kobra Plus). It allows us to quickly bring designed models into a physical model for testing and allows for a hands-on iterative development cycle that involves fabrication. Our setup shortened the iteration window from weeks with even experienced technicians to hours in the prototyping of the metamaterial structures.

The rapid prototyping system significantly streamlines the metamaterial development process. It enables us to quickly evaluate the hydrodynamic responses of different designs without the lengthy lead times typically associated with traditional manufacturing methods. This agility is vital for testing multiple design iterations, studying the effects of subtle geometric changes on the wave manipulation capabilities of the metamaterials.

Moreover, the use of 3D printing opens up the possibility of exploring complex structures that would be challenging, if not impossible, to fabricate using conventional methods. This feature is particularly beneficial when testing theoretical models that require precise geometrical features at a scale that traditional tools cannot achieve. Consequently, the fast prototyping feature has become an indispensable tool in our metamaterial design and testing workflow, fostering innovation and enabling a deeper understanding of the interaction between water waves and metamaterial structures.

3.2.2 Experimental Procedure

In our study, we followed the following procedure to carry out experiments:

The first step is to place every device in position. The projector can leave a bright reflection of its lens on the water surface. The positions of two cameras need to be well adjusted to avoid recording the lens' reflection in the main measurement regions. At the same time, the distance between two cameras needs to be large enough to increase the accuracy of the triangulation measurement. Increasing the depth of field by reducing the lens' aperture or using tilt-shift lenses can further improve the performance of the system.

The second step is to calibrate the cameras in the measurement system. With this step, the intrinsic and extrinsic parameters of the cameras are calculated from multiple photos of a chequerboard captured by both cameras. Intrinsic parameters of a camera refer to the internal characteristics of the camera, such as the focal length and lens distortion. Extrinsic parameters refer to the relative position and orientation of the two cameras in relation to each other. They

are essential in determining the 3D coordinates of the water surface.

The third step in our study is to validate the setup's precision by capturing the two-level 3D calibration plate from LaVison and the still water surface. In this step, the water remains calm. The surface is a perfect flat surface. And the reconstructed water surface should be flat too. The result is used to build a horizontal reference level for the wave measurements.

In this step, the measurement region is also identified with the photos taken by two cameras. Image masks are generated to filter out those area without useful information. We use the 500 frames of still surface to estimate the error of the reconstruction algorithm which will be discussed in further detail in the result section.

The fourth step is to put a metamaterial model in water, fixed at the bottom of the tank. Use the wavemaker to generate certain frequencies and amplitudes of waves to test the performance of the metamaterial design. In our test, we repeat each parameter set five times to ensure the repeatability of the system.

For wave generation, we selected the amplitude and frequency based on the requirement of shallow water waves, the capability of the stepper motors and the visibility of the wave-structure interactions. The torque of step motors determine the maximum frequency and amplitude of the waves we can generate. With a NEMA23 at a maximum torque 0.6 N·m, it moves the paddle at a pace of 2Hz at 1mm amplitude or higher amplitude at a lower frequency. With a NEMA23 stepper motor with a maximum torque of 2.0 N·m , it is capable of generating waves up to 3 mm amplitude at a frequency equal or under 2 Hz. To ensure both accuracy and consistency, active feedback is also enabled with the motor's motion control.

$$f_{tone} = 2\pi A f \frac{P}{S} \sin(2\pi f t), \tag{3.1}$$

where P is the micro-step counts per rotation for the stepper motor, S is the step length for the rail, t is time. It's also noticed that the travelling distance of the paddle does not directly translates to wave amplitude. In our study, the water wave heights were around half of the paddle's travelling distance depending on the water depth.

In our study, we tested wave absorption with a beach made of plastic sheets. The result shows that at a desktop size water tank, the wave absorber cannot cancel the reflective wave effectively, resulting in standing waves propagating in the tank. And the absorber also took the valuable space. Thus, we decided to take the beach out, extending the wave travel length by another 30 cm and generate a limited number of waves at each testing session. We disregard the effect of wave reflection since image capture would be done before the waves hit the glass wall at the end.

The image data captured by stereo cameras was transferred to system RAM first instead of writing directly to hard drives, to ensure accurate time steps between frames with the side benefit of ensuring the synchronisation of two cameras.

3.2.3 Results Presentation

Given that the previous chapter (Ch.2) has extensively discussed the data processing and analysis steps, this subsection focuses on explaining the approach taken to illustrating the wave-structure interactions using the derived experimental outcomes.

The results are communicated through a combination of advanced visualization tools, quantitative assessments, and comparative interpretations to capture the multi-faceted interactions between waves and metamaterial structures. The stereo-based surface reconstruction data are central to this methodology, as they supply high-resolution snapshots and spatio-temporal measurements of wave evolution.

Instantaneous snapshots (e.g., Figure 3.4(b)) highlight localized effects at particular instants, such as peak formations and sloshing, revealing how the submerged structure influences the free surface. These snapshots are augmented by time-history plots (e.g., Figure 3.4(c)), which depict the wave elevation at multiple grid points over a range of time steps. Such temporal analyses allow for the identification of critical phenomena, including shifts in wave velocity, emergence of dispersion, and changes in wavefront curvature when encountering the metamaterial.

The Wave-Surface Response Amplitude Operator (Wave Surface RAO) extends the classical manoeuvring RAO which is defined as the ratio of the incident wave to the vessel's response to characterise the spatial variation of free-surface elevation affected by an underwater structure.

$$\text{Wave Surface RAO} = \frac{\text{Surface Elevation With Underwater Structure}}{\text{Surface Elevation Without Underwater Structure}} \qquad (3.2)$$

Wave Surface RAO analyses (e.g., Figure 3.5(a–c)) provide valuable quantitative insights, particularly regarding the relative amplification and attenuation of wave heights near the metamaterial, independent of the variations in input wave amplitude due to potential mechanical inconsistency. The results highlight concentrated regions of elevated wave amplitude and areas of reduced amplitude, emphasizing spatial variations in energy redistribution. These Wave Surface RAO findings are critical for assessing the characteristics and capability of metamaterial design.

Phase contour plots (e.g., Figure 3.5(d–f)) further illustrate alterations in wavefront geometry that arise from varying water depths. These contour lines demonstrate how a linear, undisturbed wavefront transitions to a bow-shaped form upon traversing the metamaterial region. They also highlight how wave velocity correlates with the topography of the submerged structure.
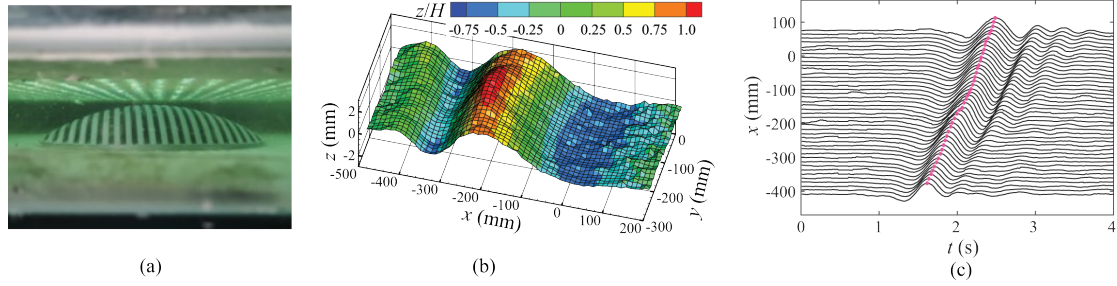
Figure 3.4: (a) The fabricated channelled spherical cut metamaterial, (b) a snapshot of reconstructed water surface under a single 2 Hz Wave at 2.0 s, (c) time history of wave elevations along the centre-line in *y* direction of the 15*th* row of the scatter grid with the red dots indicating the wave front.

By integrating these diverse visualization and analysis techniques—stereo reconstructions, time-history data, phase contour plots, and Wave Surface RAO mappings—this study captures both localized effects and broader wave propagation trends. The combined approach provides an in-depth perspective on how the metamaterial modifies wave behaviour, ensuring that the interplay between wave evolution, submerged geometry, and water depth is fully addressed.

3.3   Case I: Reconstruction of a single wave propagation

For the first two cases, a typical metamaterial design is selected to test our rapid demonstration system for metamaterial with our desktop-scale wave measurement system. The structure is shown in Figure 3.4 (a). It is a channelled spherical cut with a radius of 90 mm, height of 35 mm and each channel width is 5 mm.

The spherical cut is one of the simplest and effective structure when it comes to metamaterial, especially in the filed of electromagnetic and acoustic wave in the form of various alternated Luneburg lens designs. The channelled spherical cut design we selected here is a combination of both the lossless wave bent channel proposed by Berraquero et al. (2013) and the plate array design proposed by Porter (2021).

The purpose of this test is to study the transient response of the wave towards a metamaterial structure by measuring the wave evolution along time. The structure is tested with waves at a frequency of 2.0 Hz and an amplitude of 1.49 mm. The desktop flume water depth is at 40.0 mm.

Figure 3.4 (b) shows the reconstructed water surface. It is the instantaneous water surface at time 2.0 s, when the wave reaches the region with the submerged metamateiral structure. In this study, we operated the plunger only one cycle, generated only one period of wave. As we can see from the figure, the highest place is marked as red. The position is on the top of the centre of the channelled spherical cut. This is cause by the sloshing effect, due the water depth decreases as a result of the existence of the spherical cut.

As the snapshot of the water wave surface cannot exhibit the evolution of the wave, the wave surface is sliced with a cut in its centre. Figure 3.4(c) shows the result of one row (the 15th) out of the 35 rows with its 60 points and plots the time history of each point elevation. The wave elevation is amplified for a clear view of the wave propagation. The lower part of this plot is the region preceding the metamaterial structure. The middle part is the place where the channelled spherical cut is located. And the upper part shows the wave propagation after encountering the spherical cut. The red dots mark the peak of the wavefront at different positions along the centre line. The dots at the lower part of the plot show linear trends as time advances, and then a bend appears, followed by a recovery to a linear trend later in time. The change at the centre is due to the existence of the metamaterial structure. As the wave interacts with the structure, the drastically increasing and decreasing water depth in the metamaterial region leads to a sudden decrease in the wave's velocity at around 2.0 s, which is also the time as shown in Figure 3.4(b) as a demonstration for instantaneous water surface reconstruction where the peak of the wave surface coincides with the location of the top of the metamaterial.

In Figure 3.4 (c), the phenomenon of wave dispersion can be observed within the testing region. The input wave, conforming to shallow water wave conditions, exhibits distinct characteristics before and after encountering a metamaterial structure. Initially, in the region preceding the metamaterial structure, the wave displays minimal dispersion, as only one peak appears. This part of the wave's journey is marked by relatively stable propagation, aligning with what one might expect in a linear, undisturbed wave environment.

However, upon interacting with the metamaterial structure, a significant transformation in wave behaviour is noted. Post this interaction, there is a marked emergence of obvious wave troughs and peaks, indicative of pronounced wave dispersion. This change is a clear departure from the previously observed linear wave conditions, highlighting the metamaterial's influential role in altering wave dynamics.

3.4 Case II: Reconstruction of wave under different water depth with underwater structure

In this case study, we further examined the performance of the structure under the same wave parameters that were used in Case I at different water depths. The aim of this case is to study the amplitude and phase responses of waves towards a metamaterial structure.

The results, shown in Figure 3.5, offer a comprehensive illustration of how the subaquatic metamaterial structure influences water waves at varying depths. Specifically, Figure 3.5 (a, b, c) provides a detailed representation of the Response Amplitude Operator (Wave Surface RAO) for
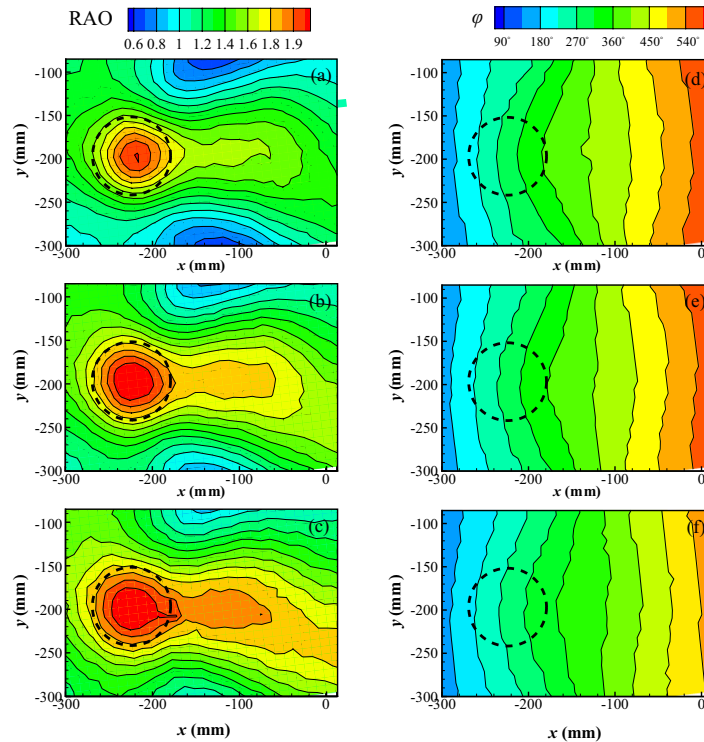
Figure 3.5: Response Amplitude Operator (Wave Surface RAO) at different water depths along with their corresponding wave phase contours: (a,d) 37 mm, (b,e) 43 mm, (c,f) 47 mm. The Positions of the metamaterial structure is illustrated with dashed line circles.

water waves at three distinct water depths: 37 mm, 43 mm, and 47 mm. Figure 3.5 (d, e, f) shows the phase plots of waves that pass the structure.

At all these different depths, a notable concentration of elevated water levels can be observed in close proximity to the pinnacle of the submerged metamaterial structure. This concentration phenomenon is most conspicuous at the greatest depth of 47 mm, where a substantial and localised elevation increase is particularly pronounced in comparison to the initial wave excitation. As the water depth increases, the concentration effect remains centred around the apex of the underwater metamaterial.

Furthermore, alongside this concentration around the structure, there is an observable 'cliff' of high Wave Surface RAO regions, which becomes more prominent and widens as the water depth increases. Simultaneously, the water surface exhibits areas of low Wave Surface RAO, depicted as a spectrum ranging from light to dark blue in Figure 3.5 (a, b, c), due to the conservation of energy water waves carried.

Considering potential applications in ocean engineering, it is worth noting that the regions of high Wave Surface RAO created by the metamaterial could serve as an ideal location for deploying wave energy converters. This strategic placement has the potential to significantly enhance the

energy output, while the areas of low Wave Surface RAO can be used for protection from the damage of large waves, offering shelters for valuable assets within the marine environment.

The Figure 3.5 (d,e,f) presents the wave phase contours (ϕ) at varying depths. The lines in the plots represents the motion of the wave front during its traverse across the tank. Initially, as the wave originates from the wavemaker, it is a straight line. While it approaches to the metamaterial structure, as show on the left-hand side of the plots, the metamaterial starts to alter the propagation of the water wave. Upon entering the metamaterial region, the wave front forms a bow-shaped distribution, a consequence of the gradual reduction in velocity resulting from the diminishing water depth induced by the metamaterial. Subsequently, as the wave progresses across the metamaterial zone, it gradually regains its original configuration, returning to a straight and uniform propagation pattern.

In Figure 3.5 (d), situated at a depth of 37 mm, the contours densely populate the diagram, indicating a rapid phase change. Conversely, at the deepest water depths of 43 mm as shown in Figure 3.5(f), the contours adopt a smoother and more widely dispersed appearance. The difference in the gaps between lines is the result of different wave travelling speeds, which correspond to the water depth.

These results serve to demonstrate the metamaterial's ability to alter and control the elevation and phase of water waves. It also provides empirical evidence that the metamaterial's effectiveness is influenced by the depth of the water.

3.5 Case III: Influence of Fundamental Geometric Shapes

This section investigates the focusing or diffraction effects of three basic shapes (diamond-shaped cube, elliptical cylinder, and cylinder) in the wave tank. The objective is to identify the focus position and the amplitude ratio at that location. Water depths vary from 50 mm to 80 mm in steps of 10 mm to accommodate the required wavelength range. Each testing structure is 40 mm tall, with a total length of 250 mm for covering both sub- and super-wavelength conditions, and a width of 200 mm (300 mm for cylinders) to fit within the 610 mm tank width. Wave frequencies range from 2 Hz to 3 Hz in increments of 0.25 Hz, as outlined in Table 3.1.

The plan combines two different shapes, each with two orientation, four depths, five frequencies, and three wave amplitudes (totalling 540 tests), with each condition repeated three times. Structures are fixed at the tank bottom using $60 \times 10 \times 5$ mm neodymium magnetic strips, attached below each model, coupled with a $40 \times 40 \times 20$ mm magnet outside the glass tank to ensure stability under wave loading. Figure 3.6 shows sketches of the three shapes.

Table 3.1: Frequency (Hz), d/λ (structure length-to-wavelength ratio), and Depth (mm) under Various Conditions

Frequency (Hz)	Depth (mm)		
	50.00	60.00	70.00
		d/λ	
2.00	0.967	0.919	0.886
2.25	1.126	1.081	1.052
2.50	1.306	1.265	1.242
2.75	1.508	1.475	1.458
3.00	0.302	0.354	0.408
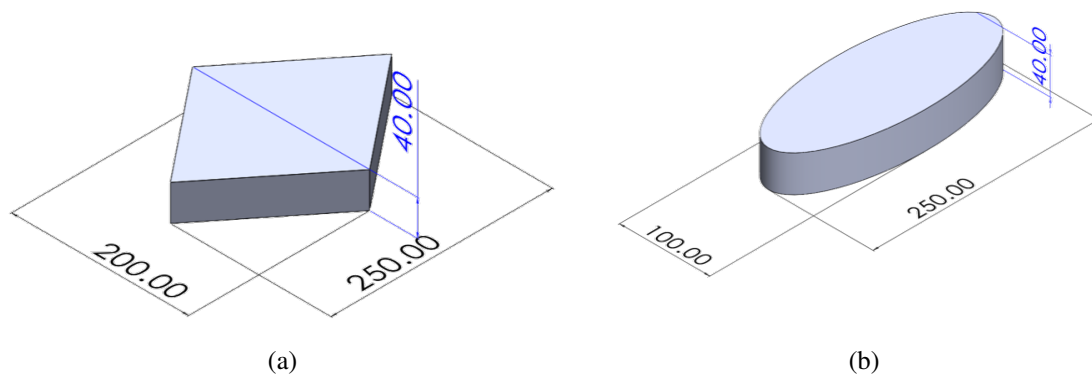
Figure 3.6: Sketches of the three geometric shapes, (a) the diamond-shape cube and (b) the elliptical cylinder

The results are divided into the following categories:

- Category I: Single geometry examined across multiple wave frequencies while water depth and amplitude remain constant. The key parameter affecting the wave distribution on the water surface is wave frequency.

- Category II: Multiple geometries examined under a uniform wave frequency, depth, and amplitude, emphasizing the influence of shape on surface characteristics.

- Category III: A single geometry assessed at a fixed wave frequency and depth, with amplitude varied, showcasing the significance of wave amplitude.

- Category IV: A single geometry subjected to the same wave frequency and amplitude while altering water depth, illustrating the effect of water depth on wave behaviour.

3.5.1 Condition I: Constant Shape & Variable Frequency

Fig.3.7 is the a demonstration of the effect of changing frequency on the wave distribution on the water surface for three selected examples. The selected conditions involve a diamond-shaped cube positioned horizontally, with a water depth of 50,mm, a wave input amplitude at the lowest value of 4,mm, and a frequency range of 2 to 3,Hz. These examples were chosen to clearly showcase the observed effects while minimizing distractions from the other tested conditions. At 2 Hz, (Fig.3.7a) the relatively long wavelength with the least $\frac{d}{\lambda}$ ratio results in smoother, more gradual interactions with the submerged structure. The wave field surrounding the structure exhibits modest amplitude variations and mild contour deformation. In particular, the wave crests and troughs remain broad in extent, showing only subtle evidence of reflection and diffraction. The observed peaks around the structure suggest localized energy accumulation where the water depth is perturbed, but these effects dissipate over a broader spatial range. Consequently, the structure's influence is discernible yet not pronounced, as the wave energy is spread over a relatively large wavelength.

At 2.5 Hz (Fig.3.7b), the shorter wavelength interacts more strongly with the structure, giving rise to sharper amplitude gradients in the vicinity of the submerged region. This is reflected in the contour plots, where isolated peaks and troughs appear closer to the structure's boundary. The increased frequency heightens wave scattering and partial reflection, since the wavelength is now more comparable to the horizontal dimensions of the feature. Moreover, the water surface experiences more distinct variations in both elevation and slope, indicating intensified interference patterns. This trend confirms that moderate frequencies elicit stronger local transformations in wave amplitude and phase.

At 3 Hz (Fig.3.7c), the wavelength has the highest $\frac{d}{\lambda}$ ratio , causing an even more localized and pronounced response around the submerged feature. The wave crests and troughs are tightly spaced, enhancing reflection and refraction at the structure edges. The contour plots show confined but distinct zones of elevated amplitude, revealing that a significant portion of the wave energy is scattered or reflected within a relatively small area around the structure. However, because each wave crest advances quickly, the spatial footprint of the structure's influence is narrower. The net effect is a more intense but spatially limited wave deformation, as successive crests do not linger to amplify reflections in the same way longer waves might. This behaviour can be especially relevant for applications involving wave energy or coastal protection, since higher-frequency waves may yield local hotspots of elevated amplitude near submerged obstacles while rapidly diminishing away from the structure.
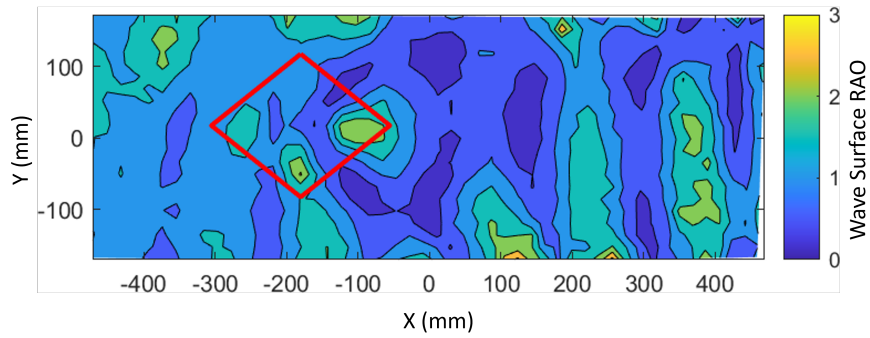
(a)
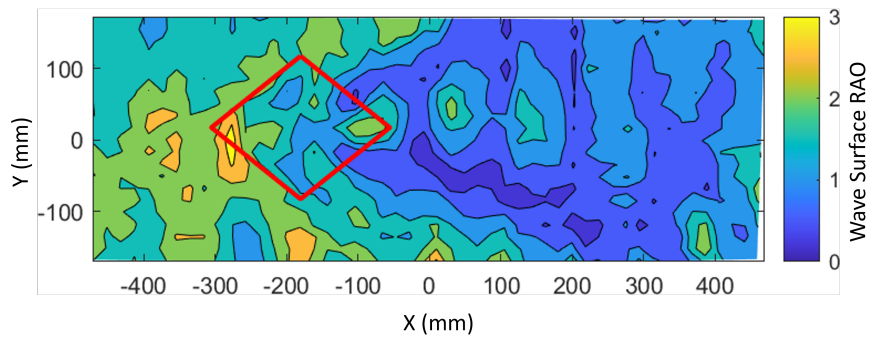
(b)
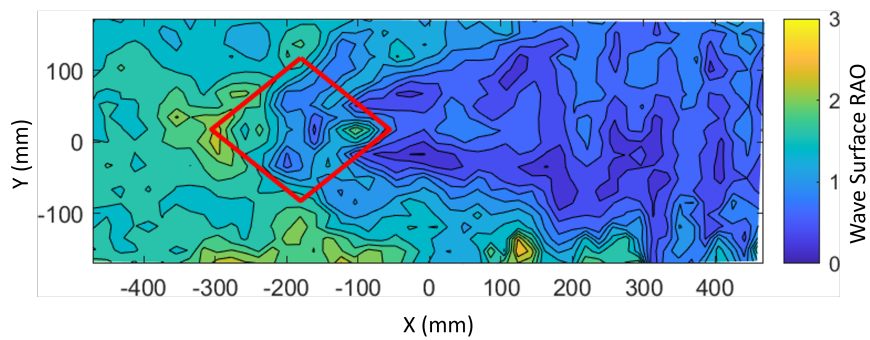
(c)

Figure 3.7: Wave Surface RAO contour of the free surface with a submerged diamond-shaped cube against structureless wave condition, the structure is represented by the red solid line. (a) for 2 Hz Wave, (b) for 2.5 Hz Wave and (c) for 3 Hz wave.

Apart from directly addressing the influence of wave frequency, it is also worth examining the broader impact of the submerged structure itself on the water surface. A submerged structure modifies local bathymetry by effectively creating a sharp decrease in water depth, which alters the balance between wave momentum and buoyancy forces. This change leads to partial wave reflection, refraction, and scattering. As a result, the edge of the structure along the wave propagation direction exhibits higher wave elevations with an observable diminishing effect as the wave becomes shorter.

A key reason behind these observations lies in the shallow-water wave celerity, which is proportional to $\sqrt{gd}$. When waves transition from deeper to shallower regions, the local phase speed decreases. This velocity difference induces partial reflection at the boundary of the submerged structure and causes the wavefront to bend or focus above and around it. Moreover, because the structure forces a sudden reduction in water depth, the wavefront experiences a localized deceleration that momentarily increases wave height above the structure's edges. As wave frequency increases and wavelength decreases, the spatial extent of such localized interactions decreases, leading to a more abrupt but less far-reaching elevation change. Consequently, the interplay between reduced depth and wave frequency governs the extent of reflection, scattering, and amplitude modulation around the submerged structure.

3.5.2   Condition II: Diverse Shapes & Constant Condition

Fig 3.8 shows the impact of different submerged structures on the free-surface wave distribution for three representative examples. Each setup is tested with a 50,mm water depth, a 4,mm wave input amplitude, and a fixed wave frequency. The illustrated configurations include a diamond-shaped cube placed in both horizontal and vertical orientations, as well as an ellipsoidal cylinder. These examples were selected to highlight how structural shape alters wave propagation, while minimizing confounding effects from variations in other experimental parameters.

A frequency of 2.5 Hz was selected to balance the need for clear visualization with the requirement of maintaining a suitable wavelength. At lower frequencies (e.g., 2 Hz), the wave patterns tend to be broader and less distinct near the submerged structure, making detailed observations of local interference or scattering more difficult. Conversely, at higher frequencies (e.g., 3 Hz), the resulting shorter wavelength can compress the wave field and obscure complex interactions around the structure. The intermediate 2.5 Hz frequency preserves sufficient spatial resolution while still providing an observable wave distribution, thereby facilitating the identification of partial reflections, amplitude gradients, and other subtle effects induced by the structure. Under identical wave conditions (2.5 Hz wave frequency, 5 mm plunger amplitude), four configurations

(a)

(b)

(c)

(d)
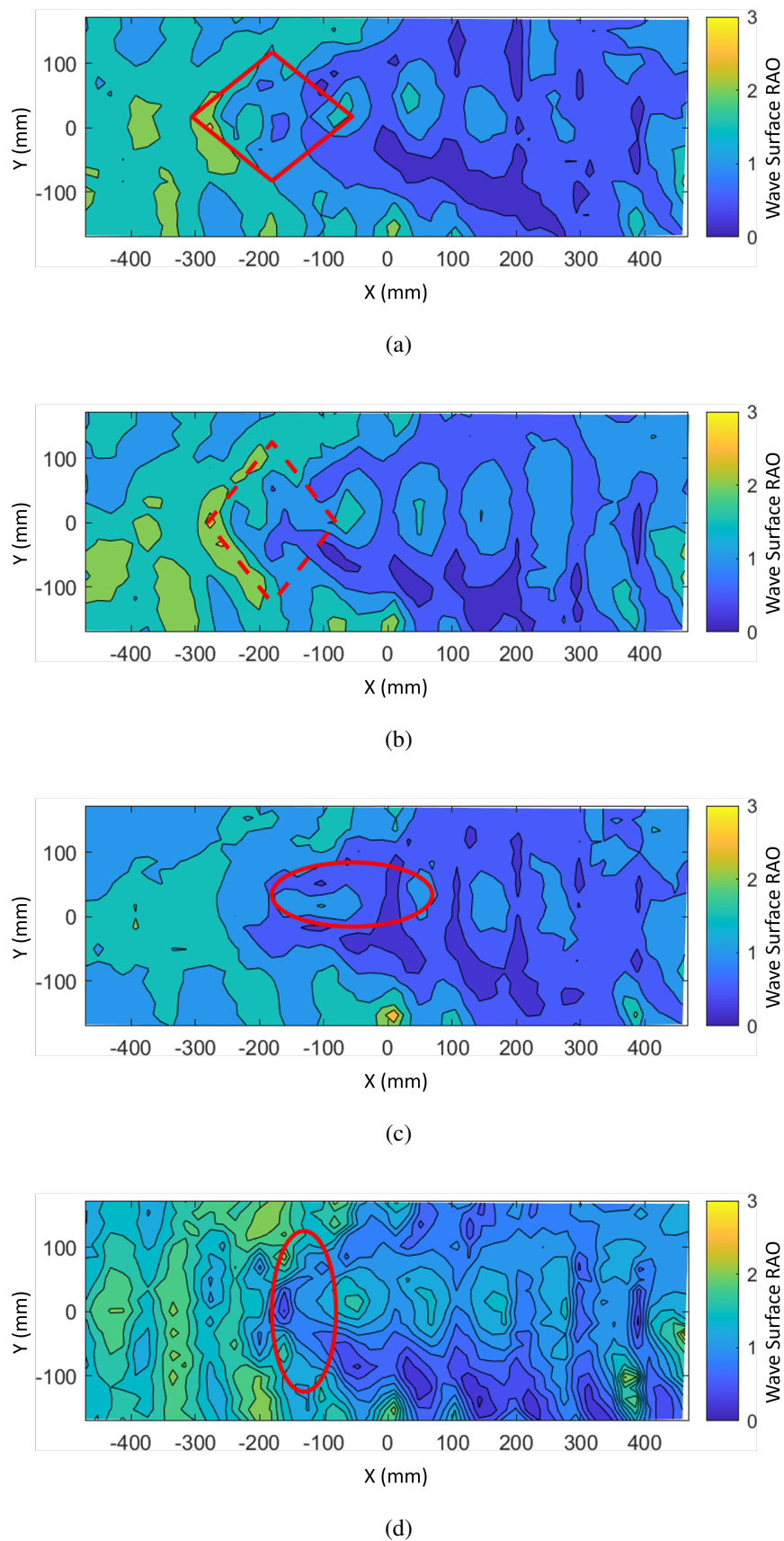
Figure 3.8: Wave Surface RAO contour of the free surface with a constant 2.5 Hz wave, 5 mm plunger amplitude and a water depth of 50 mm; (a) Horizontally placed diamond-shape cube; (b) Vertically placed diamond-shape cube;(c) Horizontally placed ellipsoidal cylinder; (d) Vertical placed ellipsoidal cylinder.

83

of a submerged structure were tested, including cases where the same design was oriented horizontally in one test and vertically in another. The contour plots highlight substantial differences in wave deformation patterns, indicating that both the structure's geometry and its orientation relative to the incoming wave significantly affect wave propagation and amplitude distribution.

When the structure is placed horizontally (Fig.3.8a,3.8c), the wavefront tends to interact with a broader cross-section along the direction of flow. This often translates into more gradual, yet spatially extensive, changes in wave elevation, as the wave encounters a lengthier region of reduced water depth. Localized hotspots of higher amplitude may still emerge at distinct edges or corners, but they are commonly less concentrated because the wave energy is distributed more evenly across the wider face of the structure.

By contrast, when the same structure is oriented vertically, a narrower but more abrupt barrier is formed in the path of the wave. The sudden transition in water depth around the structure's edges can cause sharper and more localized peaks, since the wave energy is focused into a smaller horizontal span. This often leads to more pronounced partial reflections, elevated amplitude zones immediately downstream of the structure, and potentially stronger diffraction around corners.

In both orientations, the geometric features themselves play a noticeable role in shaping the resulting wave patterns. Structures with pronounced corners, ridges, or protrusions frequently generate strong localized scattering, clearly visible as distinct amplitude gradients or high-amplitude "lobes" in the contour plots. Smoother or more gently sloping surfaces tend to disperse wave energy over a broader region, reducing the peak-to-trough contrasts in wave elevation. Subtle differences in geometry—such as rounded edges versus sharp angles—can significantly alter the spatial distribution of wave energy around the submerged object.

Overall, the orientation of a submerged structure influences how wave energy is redistributed in its vicinity, while specific geometric features determine the intensity and reach of localized amplitude changes. Comparing horizontally and vertically aligned structures under identical test conditions illustrates that even when the overall shape and size are kept the same, turning that shape by 90 degrees can create markedly different wave interactions.

An interesting notion is that In shallow-water conditions, the dominant factor governing wave interactions is the effective cross-sectional area that intercepts the oncoming wave. This prominence arises because shallow-water wave speed depends strongly on local depth rather than on the wave's inherent frequency or amplitude, making the wavefront comparatively uniform laterally. When a structure presents a large face to the incoming wave, it interrupts a greater portion of the wave crest, creating a stronger reflection, enhanced run-up, and pronounced flow redirection around the obstacle.

Minor geometric details—such as tapering or edges—tend to exert less influence under these circumstances, because the wavefront lacks sufficient depth to undergo significant three-dimensional diffraction or to expose smaller-scale structural features for any extended time. The flow around such details remains secondary to the broader interruption caused by the primary frontal area. Consequently, two structures with similarly large forward-facing areas but distinct shapes often produce comparable wave scattering and run-up, underscoring how cross-sectional blockage dominates wave-structure interactions in shallow water.

3.5.3   Condition III: Constant Geometry & Varying Wave Amplitude

Fig 3.9 shows the impact of different wave amplitude on the free-surface wave distribution for three representative examples (4 mm, 5 mm and 6 mm). Each setup is tested with a 50 mm water depth, a fixed wave frequency of 2.5 Hz and a vertically placed ellipsoidal cylinder. These examples were selected to highlight how structural shape alters wave propagation, while minimizing confounding effects from variations in other experimental parameters.

The ellipsoidal cylinder was selected as the submerged structure for demonstration in this condition given its pronounced effect on the incoming waves. Unlike geometries that feature sharp edges or abrupt corners, the ellipsoidal form provides a smoothly varying cross-section that can accentuate wave focusing in shallow-water conditions. The continuous curvature of its boundary imposes spatial gradients in wave celerity, which can promote constructive interference and local amplification above the structure. This effect is especially noticeable at moderate water depths, where the ratio of the ellipsoid's height to the overall water column remains significant, yet the fluid still retains enough depth for partial diffraction around the curved surfaces. At 4,mm amplitude (Figure 3.9a), the contour plot reveals a clear region of localised amplitude increase surrounding the cylinder. When the amplitude is raised to 5,mm (Figure 3.9b) and then to 6,mm (Figure 3.9c), these high-amplitude zones become somewhat more pronounced. However, the overall wave structure—characterised by local reflection, mild focusing and downstream scattering—remains largely consistent.

This observation suggests that, under the chosen test conditions, amplitude variations between 4,mm and 6,mm exert only a limited influence on how the submerged cylinder modifies the wave field. Although higher amplitudes do produce discernible increases in local wave height, the spatial distribution of wave activity remains similar across the three tests. Consequently, compared with the more substantial impact of water depth or structural geometry, changes in wave amplitude in this range appear to have a more moderate effect on the observed wave patterns.

(a)

(b)

(c)

Figure 3.9: Wave Surface RAO contour of the free surface with a constant 2.5 Hz wave, a water depth of 50 mm and a vertically placed ellipsoidal cylinder; (a) 4 mm plunger amplitude; (b) 5 mm plunger amplitude;(c) 6 mm plunger amplitude.

A key reason for this relatively modest difference lies in the small ratio of wave amplitude to water depth in these experiments. At 50,mm depth, amplitudes in the 4–6,mm range lie well within a regime where wave behaviour can still be treated as mildly non-linear or even predominantly linear. As a result, the increase in wave energy does not radically alter wave kinematics or generate strong non-linear effects such as substantial steepening or wave breaking. Instead, the submerged cylinder continues to shape the flow in broadly the same way, causing the wave to reflect, focus, and scatter in a spatial pattern that remains similar at each tested amplitude.

3.5.4 Condition IV: Constant Geometry & Varying Depth

Fig 3.10 shows the impact of different water depth on the free-surface wave distribution for three representative examples (50 mm, 60 mm and 70 mm). Each setup is tested with a 4 mm wave input amplitude, a fixed wave frequency of 2.5 Hz and a vertically placed ellipsoidal cylinder. These examples were selected to highlight how structural shape alters wave propagation, while minimizing confounding effects from variations in other experimental parameters.

The influence of water depth is well-illustrated by shallow-water theory, where the local wave celerity c depends on the undisturbed water depth d according to Eq 1.7. In cases where a submerged structure occupies a significant fraction of the water column (e.g. at $d = 50$ mm), the effective depth above the obstacle $(d - h(x))$ is notably reduced, giving rise to a locally decreased wave speed. This deceleration promotes pronounced wave reflection, refraction, and scattering in the immediate vicinity of the obstacle, manifesting in the form of elevated amplitudes or "hotspots".

As the water depth increases (e.g. from 50 mm to 70 mm), the submerged structure occupies a smaller fraction of the total water column, and the quantity $(d - h(x))$ remains relatively large. Consequently, the change in local celerity becomes less significant, diminishing the extent of wave–structure interactions. In contour plots, these deeper scenarios typically exhibit more uniform wave fields with weaker amplitude gradients and fewer distinct high-amplitude zones.

These results underscore the importance of the ratio between structure height and total water depth in determining how effectively submerged obstacles can redirect, focus, or dissipate wave energy. When the water depth substantially exceeds the obstacle's height, the overall wave propagation remains closer to its natural shallow-water speed, leading to more diffuse interactions and reduced wave deformation around the structure.
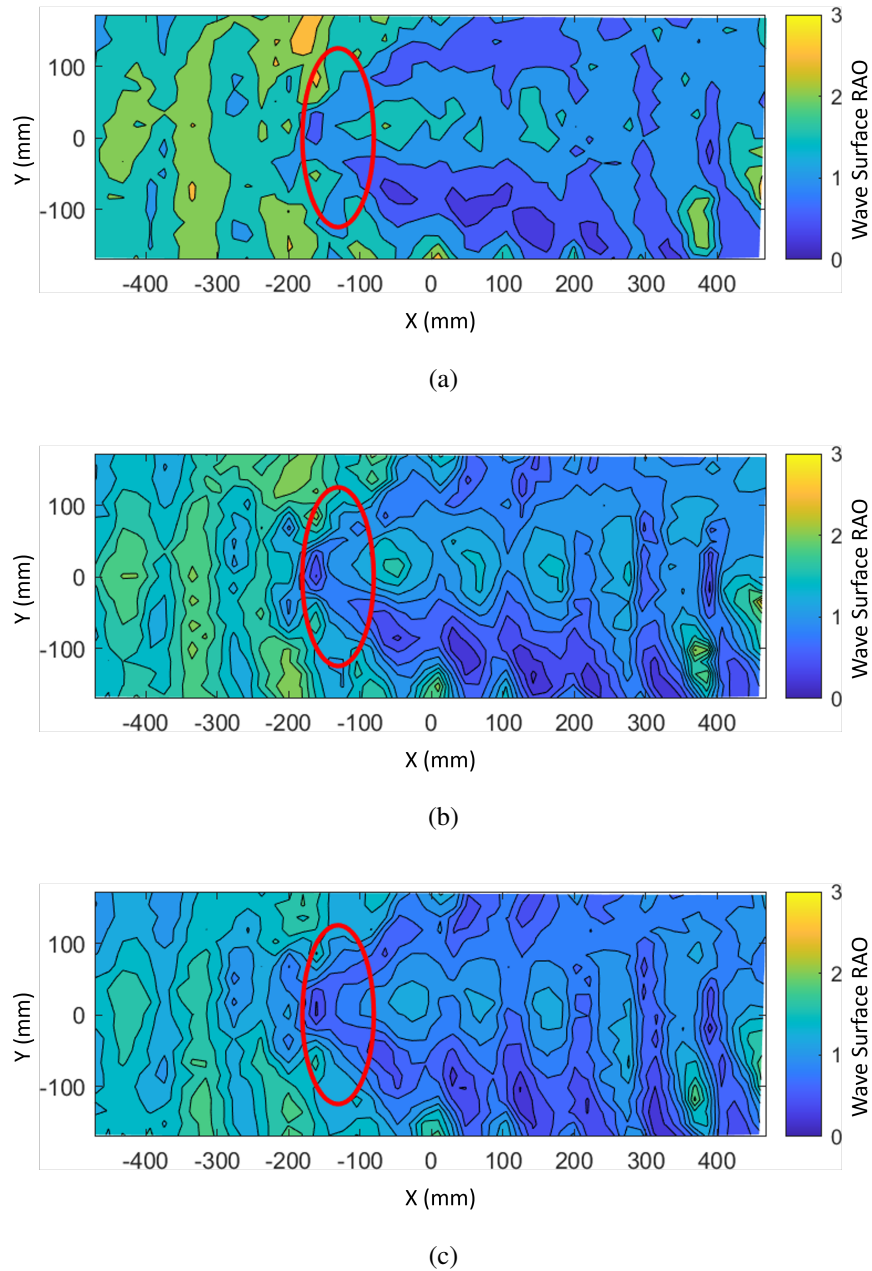
(a)

(b)

(c)
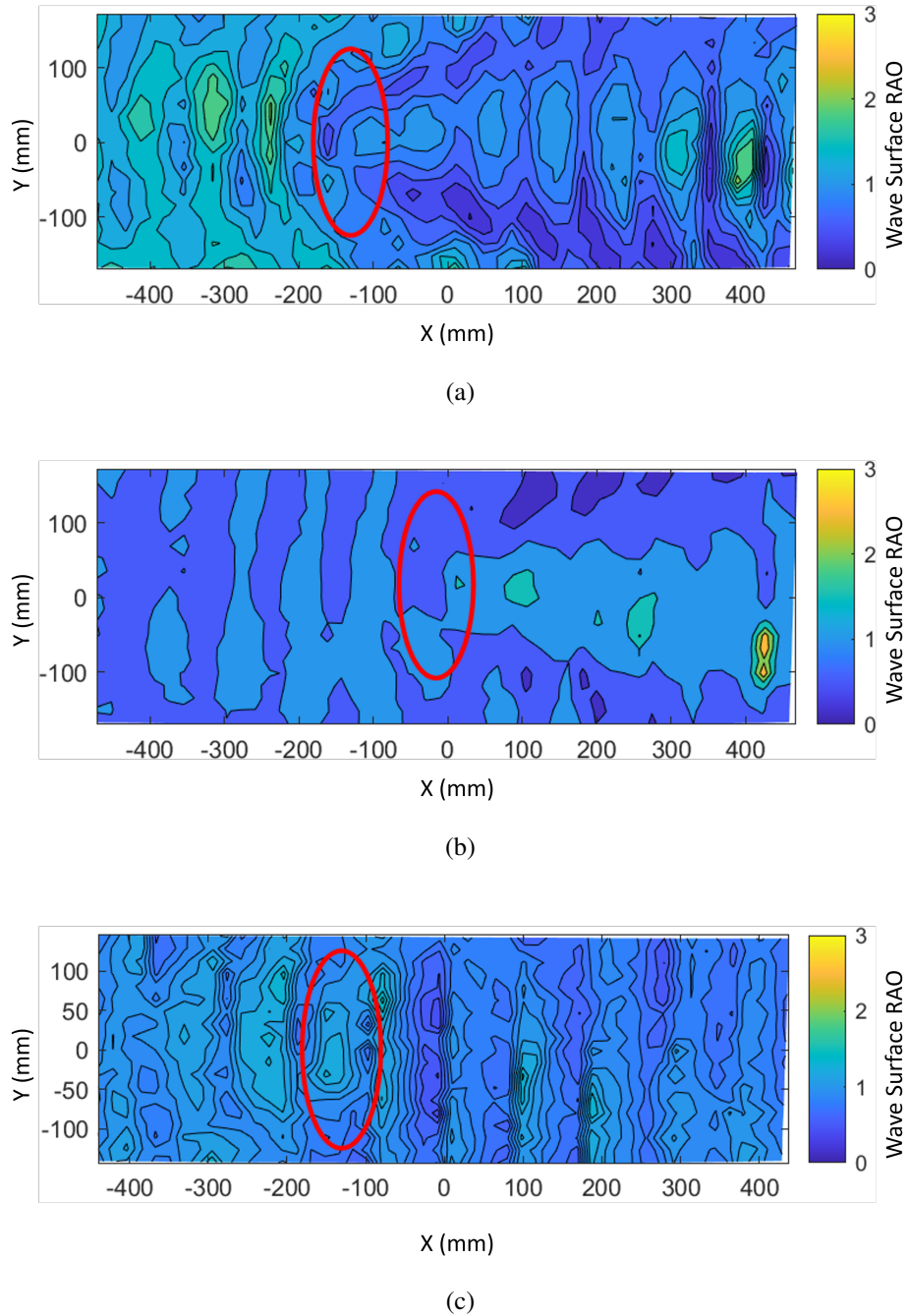
Figure 3.10: Wave Surface RAO contour of the free surface with a constant 2.5 Hz wave, a plunger amplitude of 5 mm and a vertically placed ellipsoidal cylinder; (a) 50 mm water depth; (b) 60 mm water depth; (c) 70 mm water depth.

3.6   Uncertainties and Limitations in the Experiments

While the experimental apparatus and procedures have been rigorously defined and verified it is important to explicitly consider experimental uncertainties and limitations inherent in the current set-up.

Stereo-Vision Measurement Uncertainty

Earlier calibration procedures detailed in Chapter 2 enable an accurate assessment of stereo-vision system uncertainties. Using a precise LaVision 3D calibration plate featuring a known 2 mm vertical step, the system demonstrated an average vertical reconstruction accuracy within ±0.065 mm after averaging multiple frames (Fig. 2.14). Compared to the horizontal accuracy (±0.05 mm), this indicates a slight asymmetry in resolution, specifically highlighting greater vertical uncertainty, largely owing to stereo arrangement geometry and calibration constraints. Consequently, when interpreting Wave Surface RAO and phase measurement data, vertical wave elevations reported here should be cautiously framed within a realistic uncertainty bound of approximately ±0.07 mm under laboratory conditions.

Furthermore, assessment using a still water surface, as shown in Figure 2.23, indicated a relative error of about ±0.02 % of the measurement distance, further validating positional precision under ideal conditions. However, actual dynamic experimental scenarios, particularly in Chapter 3's cases involving complex wave-structure interactions, introduce additional uncertainties. These dynamic test conditions increase measurement noise, due to transient wave reflections, surface turbulence, localised shadow effects, and minor optical distortions, which are difficult to entirely eliminate or quantify ahead of experiments. Thus, it would be prudent to consider a slightly expanded margin of uncertainty—up to approximately ±0.1 mm or roughly within approximately 0.1–0.2 % vertical elevation—when interpreting complex dynamic scenarios with interacting waves and submerged geometries.

Wave Generation Repeatability and Uncertainty

Wave consistency, governed by the plunger-type wavemaker driven by a NEMA stepper motor assembly also inherently contributes to uncertainties, particularly in wave amplitude and frequency repeatability. Nevertheless, small variations (less than ± 1.5 %) in wave amplitude from repeated tests remained measurable. Therefore, across cases studied in Chapter 3, such as waves interacting with channelled spherical-cut structures or various basic geometric shapes—wave elevation amplitude data reported should be interpreted with a realistic amplitude uncertainty roughly within ± 1–2 %.

Additionally, while the programmed wave frequency accuracy within the stepper motor system demonstrated a high degree of stability, minor deviations in realised frequencies (below $\pm$ 0.01 %) can also occasionally influence particularly sensitive resonance conditions (as suggested by the Wave Surface RAO peaks around frequency values of 0.5 to 0.8 Hz). Therefore, slight variations or inconsistencies in the precise resonance responses measured experimentally, as noticed near these resonant frequencies, may be partly attributable to minor wave frequency inconsistencies.

While carefully designed experimental protocols substantially mitigate these uncertainties, acknowledging their existence is essential. Thus, interpreting presented experimental results, particularly quantitative data such as calculated Wave Surface RAO peaks, calculated wavefront deceleration values, and spatial wave profiles, should keep these realistic uncertainty margins explicitly in mind.

Table 3.2: A Summary of Sources of Uncertainty, Typical Magnitude, and Impacted Parameters

Source of Uncertainty	Magnitude	Impacted Parameter
Vertical measurement (stereo camera)	$\pm$0.07 mm (static), $\pm$0.1 mm (dynamic)	Wave elevation, Wave Surface RAO calculation
Horizontal measurement (stereo camera)	$\pm$0.05 mm (static), $\pm$0.1 mm (dynamic)	Phase plot accuracy, wavefront geometries
Wave amplitude repeatability	$\pm$1–2% of nominal amplitude	Wave Surface RAO peak values, local amplitude enhancement
Wave frequency repeatability	$< \pm$0.5% of nominal frequency	Resonance responses, dispersion calculations
3D printing dimensional accuracy	$\pm$0.1–0.2 mm	Local wave–structure interaction (Wave Surface RAO values)
Illumination and residual optics	Unquantifiable	Wave shape detection, local surface gradients

The experimental uncertainties, synthesised in Table 3.2, predominantly stem from stereo-vision measurement constraints and wave generation repeatability. Static stereo-vision vertical accuracy ($\pm$0.065 mm) degrades marginally in dynamic cases ($\pm$0.1 mm) due to optical artefacts and geometric limitations, while wave amplitude variations ($\pm$1–2%) and minor frequency deviations ($<\pm$0.5%) subtly affect resonance and Wave Surface RAO outcomes.

These uncertainties reflect inherent compromises in laboratory-scale hydrodynamic experimentation. While calibration protocols mitigate systematic errors, dynamic interactions (e.g., turbulence, 3D-printed model tolerances) introduce stochastic noise. Quantified bounds, such as $\pm$0.1 mm for dynamic elevation or $\pm$2% wave amplitude, establish confidence intervals for

interpreting results—notably Wave Surface RAO peaks and phase shifts—without undermining their validity. Future refinements in camera resolution or closed-loop wave control could reduce these limitations, but transparency remains central to this work's rigour.

3.7   Conclusion

This chapter presented an overview of water wave metamaterial concepts and introduced a rapid, desktop-scale approach for validating metamaterial designs. By combining a 3D printing system for swift fabrication, a flexible wave flume for controlled testing, and a stereo-camera setup for accurate surface reconstruction, this study has demonstrated a powerful method for efficiently iterating between theoretical design and practical experimentation.

Several key observations emerged from the experiments. First, wave frequency markedly affects local wave–structure interactions, with lower frequencies yielding smoother, more extended patterns, and higher frequencies producing sharper gradients and confined zones of elevated wave energy. Second, moderate changes in wave amplitude (e.g. 4–6,mm) exert a relatively limited influence on the global distribution of wave activity compared with variations in frequency, structure geometry, and water depth. Third, water depth strongly governs the effectiveness of submerged structures: in shallow environments, such structures generate pronounced reflection, scattering, and focal zones, but these effects diminish as the depth increases. Lastly, the effective cross-sectional area facing the incoming wave was found to be a dominant factor in shaping wave propagation. Geometries that present a larger frontal area generally induce stronger local reflections and wave focusing than shapes with smaller effective blockage.

Alongside these hydrodynamic insights, the study validated the capability of the presented experimental setup to capture complex wave–structure interactions. By significantly shortening the prototyping and testing cycle, the system lowers development costs and accelerates research into metamaterial-inspired solutions for coastal protection, wave energy harvesting, and other marine engineering applications.

Looking ahead, the methodology is readily extendable to a wider range of hydrodynamic challenges, including different material compositions, flow conditions, and wave regimes. By refining the experimental accuracy, exploring a broader parameter space, and integrating more complex designs, future investigations may uncover novel applications for water wave metamaterials. Overall, this desktop-scale system marks an important step towards rapid, efficient, and informative experimental research in controlling and utilising surface waves.

Preliminary findings from this work were presented at the 10th PRIMaRE Conference on Marine Renewable Energy (Bath, 2023) and received the award for Best Presentation. An

extended version, highlighting the efficiency of rapid prototyping approaches, has since been published in the inaugural issue of the International Journal of Fluid Engineering (Huang et al., 2024). These recognitions underscore the potential of the system to advance fundamental research on water wave control and expedite innovation in the emerging field of hydrodynamic metamaterials.

Chapter 4

Proof of Concept Study of Innovative Wave Energy Convertor Design with Stereo Camera Motion Capture

In the previous chapters, we demonstrated how our proposed measurement system can capture water surface to study the complex wave–structure interactions. By identifying and transforming projected patterns, typically circles, captured by stereo cameras, we accurately reconstructed the water surface. Building on this wave measurement algorithm, we have also adapted the system to track objects movement.

Although these two applications may seem distinct, both depend fundamentally on accurate pattern identification and subsequent triangulation or direct linear transformation (DLT) techniques. This common methodological foundation enables the system to effectively measure wave dynamics as well as track trajectories of floating objects, facilitating enhanced understanding of phenomena such as the movement of plastic waste in oceanic environments.

The primary focuses of this chapter is the application of a stereo camera motion capture system in a proof-of-concept experiment for an innovative WEC design. Given the challenges associated with measuring power output at a 1:10 scale, our approach emphasizes capturing the WEC's motion to assess its performance.The actual performance of the prototype design would be briefly discussed, but not in great detail.

The chapter aims to validate the effectiveness of the stereo camera system by monitoring the motion of the WEC's PTO mechanism, compare the stereo camera method with conventional motion tracking systems (Qualisys), highlighting its advantages in terms of versatility and direct measurement capabilities and demonstrate the system's reliability and potential for providing detailed motion data essential for optimizing WEC design.

By centering the discussion on the stereo camera system, the chapter effectively addresses limitations inherent in traditional motion tracking methods, offering a practical and versatile

solution for motion analysis in scaled experimental setups for WECs.

4.1 Background

Wave energy converters (WECs) have gained significant attention as a means to harness ocean energy for renewable power generation. Accurate motion tracking of WECs is essential for understanding their dynamic behaviour and optimizing their design for real-world applications.

Building upon the previous section regarding tracking specific targets on or in the fluid surface, we further expand on the application of the stereo camera measurement system to motion capture of a WEC model.

The core idea involves detecting features (markers) on the region of interest of the WEC across frames from two cameras, as well as sequential frames from the same cameras. Unlike the setup for stereo camera wave measurement—where the grid of projected dots is presumed to remain largely unchanged—WEC motion detection and path reconstruction require more manual input due to the dynamic nature of the object. By capturing images from two synchronized cameras, these systems can reconstruct the three-dimensional motion of objects with high precision. This capability is particularly useful in situations where traditional measurement methods are impractical or insufficient.

ZOEX LTD, through the Interface Innovation Voucher scheme, collaborates with the Kelvin Hydrodynamics Laboratory of the University of Strathclyde to investigate the performance of a modular WEC both numerically and experimentally. Figure 4.1 illustrates the design concept, where the main floating unit is made of a commercially available Yokohama Fender and is connected to a base structure. This base structure can be easily integrated with other marine installations, such as breakwaters, aquaculture fish farms, and more.
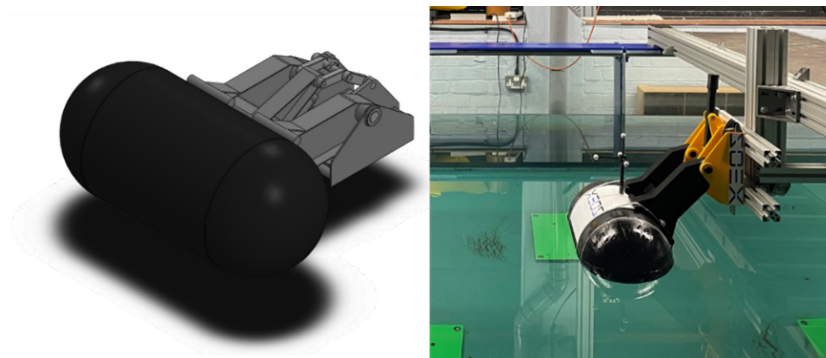

Figure 4.1: ZOEX modular WEC con concept design

ZOEX's primary breakthrough lies in its cost-effectiveness by integrating with an aquaculture feed barge, offering a competitive alternative to diesel. Innovative features of this specific WEC

design include:

- **UMBRA Electro-Mechanical Generator (EMG)**: Provides precise control, high efficiency, and dependability.

- **Hinge Design and Mechanical Intensifier Mechanism**: Prevents end stops and improves performance and utilization rate.

- **Compliant Rubber Yokohama Fender**: Safeguards the host structure against impacts.

ZOEX operates silently and is emission-free, outperforming solar panels in marine settings, which often suffer from poor performance in northern latitudes and degradation due to corrosion and wave impacts. The anticipated outcome of this project is to reduce the aquaculture sector's reliance on diesel generators, contributing to environmental sustainability.

Motion Capture Challenges and Solutions

Given the 1:10 scale of the WEC model, evaluating its performance based on power output is challenging because the power generated at this scale is minimal and cannot be measured reliably. Therefore, monitoring the motion of the WEC becomes essential for assessing its behaviour and validating numerical simulations.

To achieve this, we employed both the stereo camera system and a conventional motion tracking system, Qualisys, to verify the reliability of the stereo camera method. While the Qualisys system requires a tree-shaped tracking target to reliably track the motion of the WEC—which then needs to be interpreted to infer the motion of the power take-off (PTO) mechanism—the stereo camera system can track the motion of the PTO directly using two sticker markers at a rate of 100 frames per seconds. This direct tracking makes the stereo camera system more versatile and suitable for capturing the specific motion of interest without additional interpretation.

Capturing the motion of the WEC model accurately is crucial for validating numerical simulations and refining design parameters. Understanding the dynamic response of the WEC to wave interactions enables engineers to optimize the design for enhanced energy conversion efficiency and structural integrity.

The stereo camera motion capture system allows for precise measurement of the WEC's motion without interfering with its operation or adding any additional structure for tracking which may obstruct the device's movement apart from sticker maker on the above waterline part of the device. By tracking specific markers on the WEC, detailed data on its movement in three dimensions can be obtained, which is essential to assess performance and make necessary design adjustments.

The process begins with the manually matching of the first pair of detected features (points) between the two camera views. This manual step establishes a reference point for subsequent automated processes. The selected features should be distinctive and easily trackable across frames, such as corners or markers on the ship's surface.

Then, attention is turned to the sequential frames from the same camera. Given the high framerate at the ship motion is recorded and the relatively slow and steady movement of the model ship, it's safe to assume that between two sequential frames, the relative location of the detected feature is close; thus it is straightforward to match features by its minimal distance counterpart in the consequential frame. After such a process, the features extracted from pairs of images are matched and ready for triangulation and establish a time history of three-dimensional device movement.

In summary, the stereo camera method offers a more versatile and direct approach by allowing the tracking of specific features on the WEC without the need for elaborate marker setups. By focusing on the motion of the PTO directly, the stereo camera system provides detailed insights into the WEC's operational dynamics, facilitating a more accurate and efficient evaluation process.

4.2 Experimental Setup

The experiment is carried out in the 3D compact wave tank within the Kelvin Hydrodynamic Laboratory, as seen in Fig.4.2. The compact glass-sided 3D tank features 8 x 0.7m hinge depth force feedback absorbing flaps in a glass tank of 5.6 m wide and 9 m long, and the water depth is fixed to 1 m. The tank also features three beach segments to minimise wave reflection. The glass-sided design enables excellent visibility for observing experiments and capturing high-quality motion tracking data, making it ideal for testing wave energy converters.

This proof of concept experiment aims to explore the feasibility of the ZOEX wave energy converter in terms of the integrated design and dynamic response under wave excitation only, with the experiment setup shown in Fig.4.3. As mentioned in the previous section, no attempts of optimizing the power output are made.

Due to the small model scale of the PTO system used in the experiment, accurately representing the PTO characteristics is beyond the scope of this study, and only a rough estimation of the potential power output is attempted.
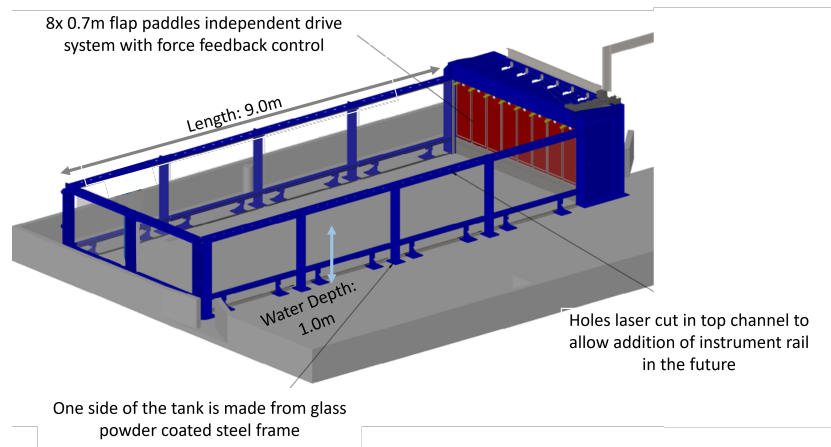
Figure 4.2: CAD illustration of the 3D compact wave tank

The model body is mainly manufactured using the Lab's 3D printer with a scale of 1: 10 and then assembled by experienced technicians based in the lab.

A ballast weight of 11.5 kg calculated based on the Froude scale was installed inside the Yokohama fender to achieve a neutral buoyancy draft line at the middle of the Yokohama fender. By aligning the draft line with the centre of the fender, the model simulates the intended immersion depth and hydrodynamic behaviour, allowing for more precise experimental observations of the WEC.

Due to the relatively small full-scale dimension of the ZOEX concept, even a 1:10th scale made it practically challenge to include a realistic PTO system in the experiment. To mimic the effect of the PTO in the full-scale design, a 3D printed UMBRA linear generator was adopted. The PTO consists of a hollow chamber shaped as a cylinder and a piston which is able to slide into the hollow chamber. The pressure inside the chamber changes depending on the sliding speed of the piston. At the top of the air chamber, there are 6 holes. By changing the number of holes open to the air, different levels of pressure can be achieved, hence different level of damping can be simulated. Note that the range of damping factors achieved are not equal to the true level of the UMBRA PTO.
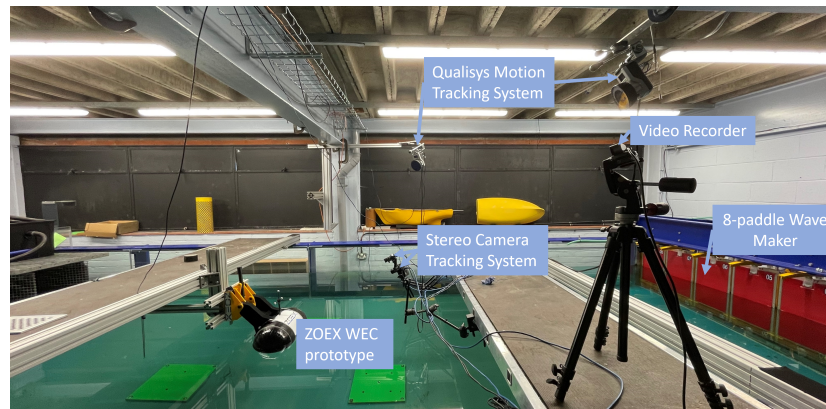
Figure 4.3: Measurement arrangement with clear indication of the both motion tracking system, the WEC prototype, a video recorder for documentation and the 8-paddle Wave Maker at the end of the tank

During the tests, two conductive wave probes were installed in the tank, one in front of the fender to monitor the incoming wave and one behind the fender for the outgoing wave as well as the reflection.

The wave probes were calibrated by incremental water level adjustment. The probes were fitted to a 45x45 aluminium extrusion bar, which itself was attached to a linear rail driven by a stepper motor. The stepper motor was controlled by the script described in chapter 2, where 53 data points were produced and used to calibrate the wave probes.

Both raw data and the processed results of wave probe 1 (measuring the incoming wave) are presented as an example.

The calibration results seen in Fig.4.4 clearly demonstrated that the wave probes shows a good linearity for the test range and thus was suitable for monitoring the incoming waves. The second wave probes monitoring the outgoing wave (and reflection) yielded a similar results.

For Qualisys system, a set of propitiatory cameras are deployed around the model and 4 reflective tracking targets forming a body co-ordinate system are fitted to the Yokohama fender. During the test, the Qualisys cameras tracks the trajectories of the body co-ordinate system and 6 degrees of freedom (DOF) motion of the fender can thus be measured and recorded. Two additional reflective markers are fixed onto the PTO, one on the slide and the other on the PTO external shell, the relative motion between the two (and hence the velocity) can then be measured by the stereo camera system for validation and comparison.

The Qualisys system relies on a precise calibration process to ensure accurate motion capture and dependable data acquisition. This process encompasses both intrinsic and extrinsic calibration. The calibration involves an L-frame to define the global coordinate system and a T-shaped wand with reflective markers. The L-frame establishes the X, Y, and Z axes, while the wand is moved
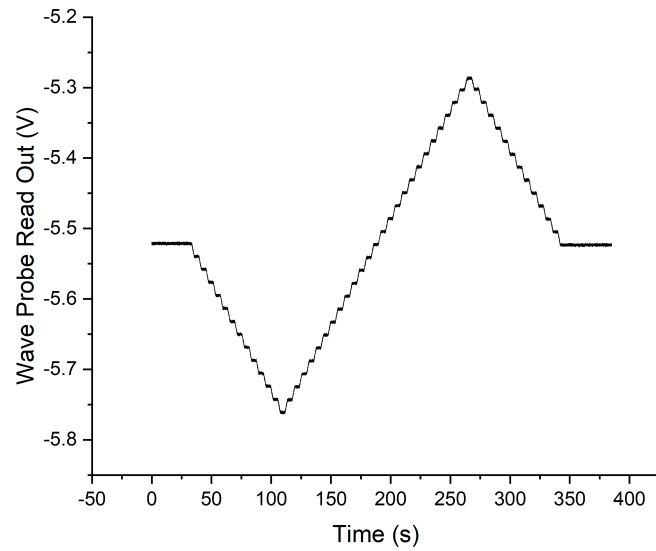
(a)
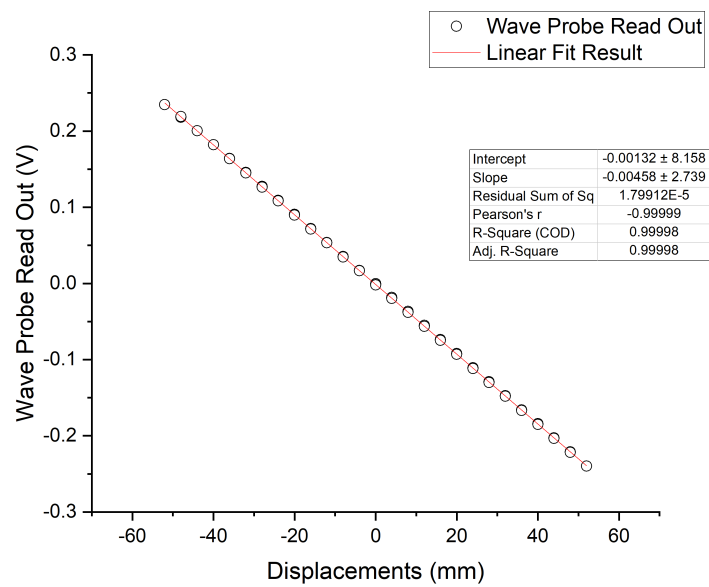
(b)

Figure 4.4: Wave probe calibration process data and results: (a) the time history of wave probe reading during calibration process (b) the extracted data points and the linear fit results.

through the capture area to ensure all cameras align accurately. Following calibration, the system evaluates accuracy by examining metrics such as average residuals and consistency of wand length measurements, with residuals of under 1 mm, it's considered satisfactory for use.

The stereo vision cameras were calibrated using the same procedure described in earlier chapters. This entailed moving the aluminium calibration target throughout the capture region, with particular emphasis on the WEC deployment area, while including rotations around all three axes.

Prior to its deployment in water, the device is checked in dry condition to assess the manufacturing quality which may affect the maximum rotation range of the WEC's piston. These checks confirmed that it can freely rotate up to 180 degrees about the pivot point with minimal mechanical resistance. This rotational freedom is crucial for ensuring robust performance during operation, allowing the device to adapt to varying loads and fluid dynamics without encountering excessive strain or friction.

An interesting observation during the test is that the fender can rotate about the pivot point from 0 to 180 degrees with no obvious resistance. This suggests that during extreme wave conditions, the fender can either be lifted out of the sea or fully submerged to avoid excessive loads.

4.3   Experiment Methodology

The experimental programme focuses on assessing the ZOEX Wave Energy Converter's (WEC) performance under controlled conditions. It comprises three test phases: free-decay tests to identify natural frequencies and damping characteristics, regular wave tests to examine dynamic responses across a range of wave frequencies, and irregular wave tests to evaluate performance under realistic sea states. These tests provide critical data for understanding and optimizing the WEC's operation.

4.3.1   Experiment Conditions

Three different sets of tests were performed in the experiment programme to exam the device's characteristics, namely,

- Free-decay test under 8 damping conditions (from no pto at all to all airholes opened) to determine the natural frequencies and damping levels introduced by the PTO.

- Regular wave tests for 64 s each under uniformed wave amplitude (0.35m at full scale) with frequencies ranging from 0.3 to 1.3Hz, which is equivalent to a full scale wave period range from 2.5 to 10.5 seconds. In total, 14 wave frequencies (thirteen standard wave

frequency plus one more test at the natural frequency) and 7 damping conditions, 113 tests are carried out.

- Irregular wave tests for 20 mins each using the optimal conditions from analysis of the regular wave tests results with 11 pairs of significant wave heights and peak periods.

Throughout all tests, the wave direction was kept normal to the ZOEX, and the sea state conditions were chosen to replicate real-life deployment. The wave amplitude also remained constant, so this evaluation of the WEC would focus on how frequency and damping influence the WEC's performance. The measured wave amplitude from the incoming wave probe was nondimensionalized using the response amplitude operator (RAO) which enabling us to describe and process the experiment results with a dimensionless number which can be directly compared regardless of scale or conditions.

For the regular wave tests, the wave amplitude is fixed at 0.35m in full scale. Such moderate wave amplitude is selected to best represent the deployment condition of the device with consideration of the capacity of the 8-paddle wave generators. Since the Zoex WEC is designed to operate alongside ocean agriculture, its performance in lower wave amplitude would be of more significance. It's also safe to assume that good performance in lower wave amplitude would indicate decent performance in high sea while the opposite may not be true.

4.3.2 Free Decay Test Procedure

During the free decay test, the float is initially displaced from its equilibrium (floating) position, then released with no external force, allowing the float's oscillation to decay naturally while its motion is monitored using the Qualisys system.

The oscillation time history is then plotted to identify the WEC's natural frequency. The test is repeated six times, each with a different number of air holes blocked to simulate varying damping conditions. Next, the PTO is disconnected from the fender, and a free decay test is conducted with no PTO damping to assess the hydrodynamic damping introduced by the fender's motion.

The difference between cases with PTO damping and the case without PTO thus indicates the damping contributed by the PTO. From the free decay test, the natural frequencies under each damping condition can be determined, providing essential information for designing the regular wave test matrix. By selecting wave frequencies that encompass all damped natural frequencies, the regular wave tests will capture peak dynamic responses around each natural frequency under distinct PTO damping conditions.

4.3.3 Regular Wave Tests

For the regular wave tests, the 8-paddles wave generator operates for 64 seconds, during which motion data are recorded by both the Qualisys system and the stereo vision camera, along with measurements of incoming and outgoing waves. Between consecutive tests, a 10-minute interval is allowed for the water surface to settle and for preliminary data processing. Each test, conducted under the same wave amplitude input, is repeated 14 times for each damping condition.

4.3.4 Irregular Waves (Seastate) Tests

After the regular wave tests, a set of seasate experiment is performed with different peak period and significant wave height to assess the performance of the ZOEX wave energy converter under irregular wave loading. The seastaes waves are governed by a JONSWAP spectrum (Hasselmann et al. (1973)).

$$S(\omega) = \beta_J H_s^2 \, \omega_p^{-4} \, \omega^{-5} \, e^{-1.25\left(\frac{\omega}{\omega_p}\right)^{-4}} \gamma^{e^{-\frac{\left(\frac{\omega}{\omega_p}-1\right)^2}{2\sigma^2}}} \tag{4.1}$$

where H_s is the significant wave height, γ is the peak enhancement factor (taken as 3.3), and β_J is a coefficient obtained using the following approximation:

$$\beta_J \approx \frac{0.06238}{0.230 + 0.0336\gamma - 0.185(1.9+\gamma)^{-1}} \times [1.094 - 0.01915\ln\gamma] \tag{4.2}$$

ω_p is the peak angular frequency, which is related to the peak period T_p as:

$$T_p = \frac{T_s}{1 - 0.132(\gamma+0.2)^{-0.559}} \tag{4.3}$$

The coefficient σ is determined based on the relationship between ω and ω_p as:

$$\sigma = \begin{cases} 0.07, & \omega \leq \omega_p \\ 0.09, & \omega > \omega_p \end{cases} \tag{4.4}$$

The seastate matrix is shown in the Table.4.1

Extensive tests in low seastate were conducted while for higher seastate, the focus is on the peak period closest to the damped natural frequency of the fender to observe the changes in power output.

Table 4.1: Wave Conditions in Model and Full Scales

Param	1	2	3	4	5	6	7	8	9	10	11
H_m	0.015	0.015	0.015	0.015	0.015	0.025	0.035	0.045	0.055	0.065	0.075
H_f	0.150	0.150	0.150	0.150	0.150	0.250	0.350	0.450	0.550	0.650	0.750
T_m	1.107	1.423	2.055	2.371	2.688	2.056	2.056	2.056	2.056	2.056	2.687
T_f	3.501	4.500	6.500	7.498	8.500	6.500	6.500	6.500	6.500	6.500	8.498

Note: H_m = model-scale significant wave height (m), H_f = full-scale significant wave height (m), T_m = model-scale peak period (s), T_f = full-scale peak period (s).

4.4 Experimental Results

4.4.1 Comparison Between Stereo Camera and Qualisys Results

A direct comparison was performed between the Qualisys motion capture system and the Stereo Vision system developed in this study. Both systems measured displacements in millimetres
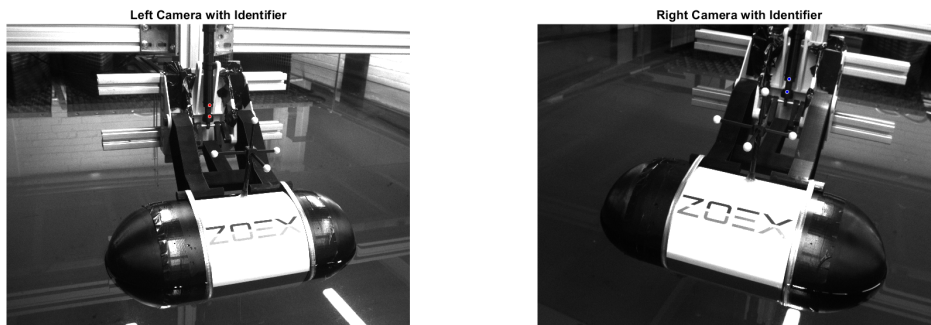
Figure 4.5: Snapshot of from the stereo-camera setup during a regular wave test with the piston tracker identified by the algorithm (red for the left camera and blue for the right camera), since the test goal was to measure directly the piston displacement, the algorithm has been modified to track only the piston tracker while ignoring the main body of the floater

during the same tests. A statistical and visual analysis was conducted to evaluate the agreement between the two methods.

Fig.4.6 is a direct comparison between the stereo vision motion capture and Qualisys system with a 0.3 Hz wave with zero air-hole opened, which is the most suppressed scenario in terms of piston movement. The suppressed piston movement would present the most extreme condition for the stereo vision capture given the relatively small displacement of the piston.

Such comparisons were then extended to cover a whole set of test suite, using the three air-holes opened cases as an example. The results are presented in both absolute value and the differences in mm and percentages, illustrated in Fig.4.7. The percentage differences are
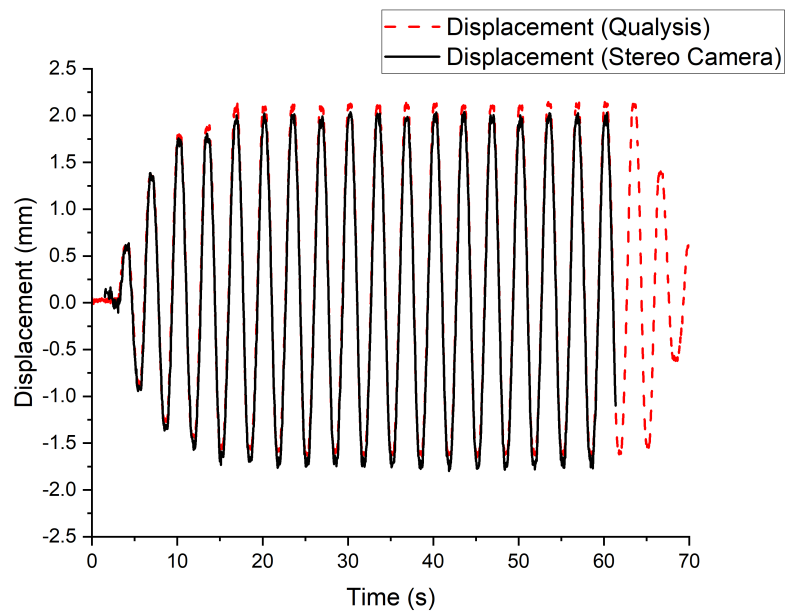
(a)
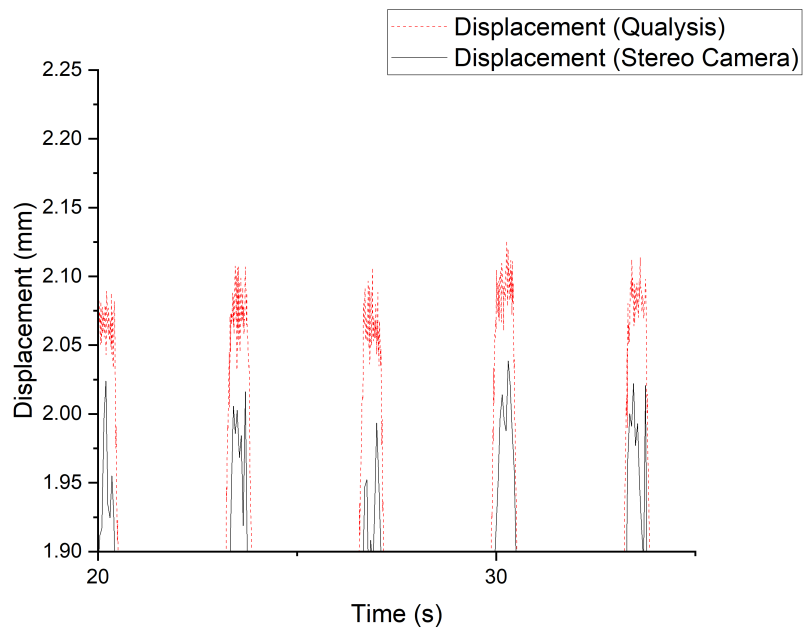
(b)

Figure 4.6: Comparison of Qualisys and stereo camera piston displacement results under the no air-hole opened condition and 0.3 Hz wave, with (a) a full view of the experimental window and (b) the zoomed-in comparison suggested an roughly 0.07-0.9 mm difference between the stereo vision captured data and Qualisys captured data.
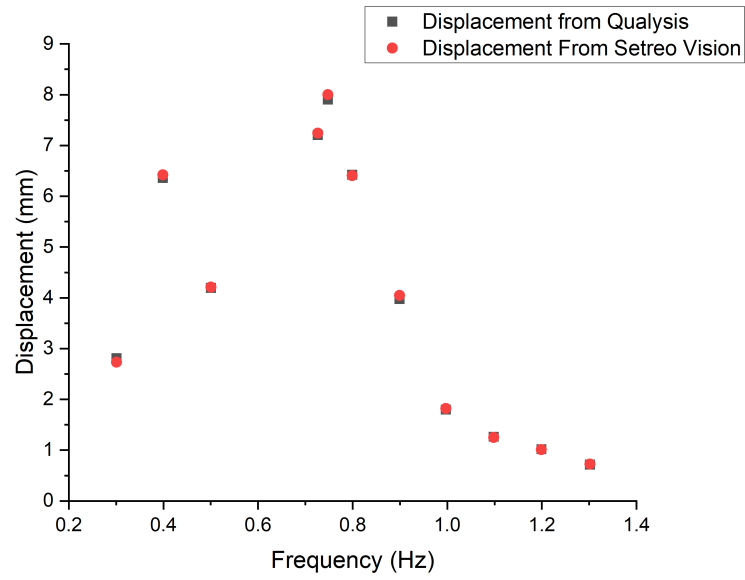
(a)
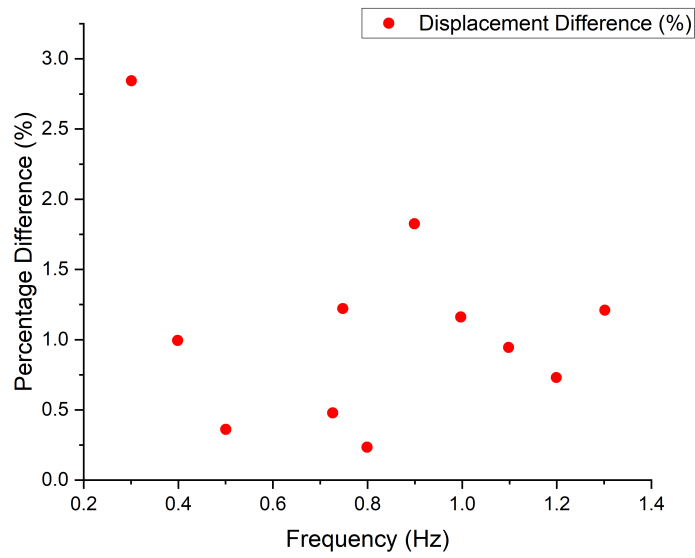
(b)
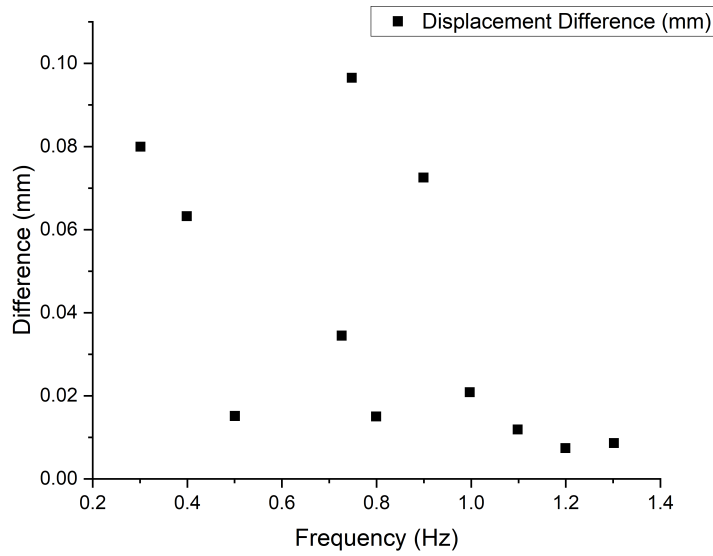
(c)

Figure 4.7: Comparison of Qualisys and stereo camera piston displacement results in (a) direct comparison and (b) percentages and (c) Absolute millimetres.

calculated as:

$$\text{Percentage Difference} = \frac{|Q - S|}{Q} \times 100.$$ (4.5)

where Q is the Qualisys measurement and S is the Stereo Vision value.

The mean percentage difference between the Qualisys and Stereo Vision measurements is computed as follows:

$$\text{Mean Percentage Difference} = \frac{1}{n} \sum_{i=1}^{n} \frac{|Q_i - S_i|}{Q_i} \times 100$$ (4.6)

which is 0.88%, indicating that the two systems are in close agreement.

The standard deviation of the percentage difference was 0.45%, highlighting the consistency of the Stereo Vision system relative to the Qualisys system.

The Root Mean Square Error (RMSE), which is calculated as:

$$\text{RMSE} = \sqrt{\frac{1}{n} \sum_{i=1}^{n} (x_{\text{Qualisys},i} - x_{\text{Stereo},i})^2}$$ (4.7)

was found to be 0.043 mm, confirming that the discrepancies between the two systems are negligible and within acceptable limits for practical applications.

The results demonstrate that the Stereo Vision system provides highly reliable measurements

that closely align with those of the established Qualisys system. The observed differences are minimal, with an average deviation of less than 1 percent, confirming the robustness and reliability of the Stereo Vision method for displacement measurements in dynamic testing scenarios.

This level of agreement underscores the potential of the Stereo Vision system as a cost-effective and accurate alternative to commercially available motion capture systems for similar applications. Further validation under diverse conditions could solidify its applicability across broader experimental settings.

4.4.2 Free Decay Test Results

During the free decay data processing, a MATLAB script is employed to systematically analyse each test file stored in a specified directory. The script extracts the pitch data from the time series and identifies prominent peaks in the signal based on the concept of peak prominence. A peak's prominence quantifies how much the peak stands out due to its intrinsic height and its relative position compared to nearby peaks. Notably, a relatively low yet isolated peak can exhibit greater prominence than a taller peak overshadowed by neighbouring peaks.

In practical terms, the prominence of a peak is determined as follows: the peak in question is marked, and a horizontal line is extended from that peak in both leftward and rightward directions until it encounters a higher peak or the endpoint of the signal. Within each of these two intervals, the minimum value (either a valley or the signal endpoint) is identified. The higher of these two minima serves as the reference level. The difference between the peak height and this reference level is the peak's prominence.

By applying a minimum threshold for peak prominence, the script ensures that only well-defined peaks are considered for analysis. Subsequently, two or more selected peaks are used to calculate the damping ratio, ζ, via the logarithmic decrement method. This approach provides a reliable measure of damping for each free decay test, enabling comparisons across varying conditions or with other experimental datasets.

The damping ratio, ζ, is defined as:

$$\zeta = \frac{c}{c_{\mathrm{c}}},\qquad(4.8)$$

where c is the viscous damping coefficient while c_c is the critical damping coefficient.

The critical damping, D_{critical}, is estimated as:

$$D_{\mathrm{critical}} = 2\sqrt{I \cdot k}\qquad(4.9)$$
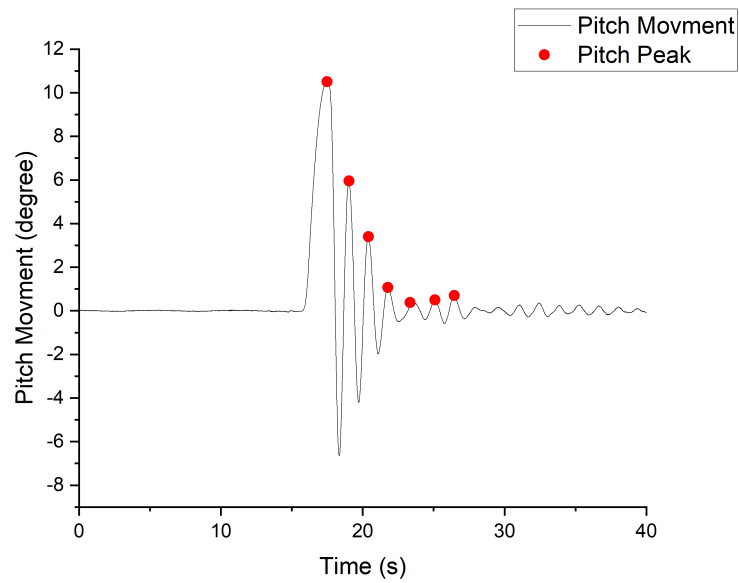
Figure 4.8: One of the Free Decay test results with no PTO installed (free movement)

where I is the rotational inertia about the pivot point, and k is the hydrostatic restoring coefficient in the pitch direction, also relative to the pivot point. The rotational inertia is calculated using the Boundary Element Method (BEM) package NEMOH, and subsequently transferred to the rotation point using the parallel axis theorem. For this experiment, the final inertia at the rotation point is found to be $1.4533\,\mathrm{kgm}^2$, and the hydrostatic restoring stiffness in the pitch direction is determined as $62.4\,\mathrm{N\cdot m/rad}$.

The actual rotational damping applied to the fender can then be calculated based on the above equations. The results are presented in Table 4.2.

Table 4.2: Free Decay Test Results under Eight Damping Conditions

Number of Opened Air Holes	6	5	4	3	2	1	0	No PTO
Natural Frequency (Hz)	0.72	0.72	0.71	0.72	0.68	0.71	0.69	0.70
Total Damping Ratio	0.136	0.128	0.105	0.107	0.098	0.107	0.091	0.089
PTO Damping Ratio	0.046	0.038	0.016	0.018	0.009	0.018	0.001	0.000
PTO Damping (N·m·s/rad)	0.876	0.723	0.305	0.343	0.171	0.343	0.019	0.000

Note: In all figures and tables, the number of holes refers to the opened air holes on the PTO piston, and the PTO damping ratio is calculated by subtracting the total damping ratio with the damping ratio with no PTO system installed.

By using this framework, the damping characteristics of the system can be comprehensively analysed, providing critical insights for validating experimental results and informing conclusions.

4.4.3 Regular Wave Results

In addition to standard 0.1 Hz increment from 0.3 Hz to 1.3 Hz, more steps are added between 0.65 to 0.75 Hz to fully capture the damped natural frequencies informed by the free decay tests results. Regular wave results are presented in the form of Response Amplitude Operation (RAO), defined as the ratio between the response amplitude and the input wave amplitude. In the case of the current tests, the pitch motion RAO is defined as a ratio between the pitch amplitude in degrees and the incoming wave amplitude in m,

$$\text{RAO} = \frac{\text{Pitch Amplitude (degree)}}{\text{Incoming Wave Amplitude (m)}}. \tag{4.10}$$

The incoming wave amplitude was extracted using the front wave probe, and the pitch amplitude was extracted using the Qualisys 6 DOF motion data. The model scale regular waves results across all wave frequencies and damping conditions are shown in the following Figure 4.9a along with the corresponding full scale results (Fig. 4.9b).

The data in both Fig. 4.9a and 4.9b indicate that the maximum pitch amplitude occurs at approximately 0.6 Hz in the model scale, corresponding to a full-scale wave period of around 5.3 seconds. This effect is particularly evident in the region of the damped natural frequency (full-scale: around 6–10 seconds; model-scale: about 0.8–1.2 Hz), where resonance-induced motion is heightened. As the number of airholes increases, the RAO decreases more substantially within this frequency range, confirming that the damping is most effective where resonance-driven motions would otherwise be greatest.

Beyond the resonance region, the RAO values do not vary greatly across different airhole configurations, suggesting that the overall damping introduced may be insufficient to optimise power extraction at frequencies removed from the natural peak. Nevertheless, the consistent trends observed between the full- and model-scale data validate hydrodynamic similarity and highlight the potential for tuning airhole configurations to balance structural stability against energy capture. The ability to adjust damping in this manner provides a valuable means of controlling pitch motion, thereby enabling further exploration of how to enhance power output without compromising the integrity of the device.

Apart from the float movement, piston movements are also tracked, below is the displacement of the piston during regular wave tests:

(a)

(b)
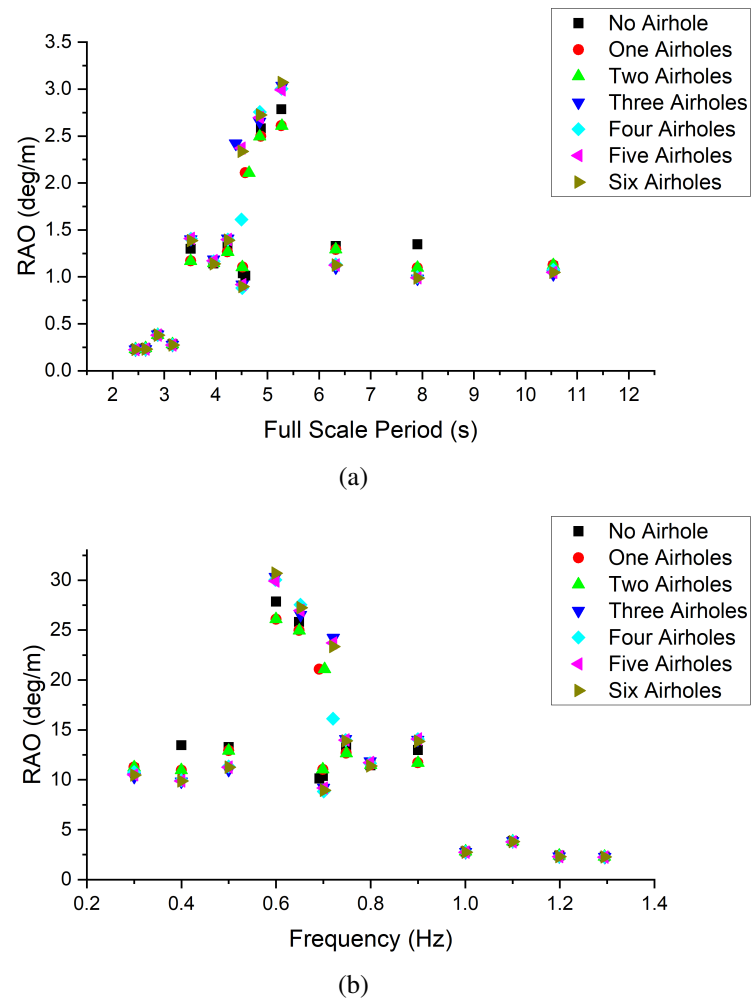
Figure 4.9: Pitch motion Response Amplitude Operator (RAO) of (a) full-scale (wave period: 1.5–12 s) and (b) model-scale (frequency: 0.2–1.4 Hz). RAO magnitudes (deg/m) quantify pitch angular displacement per unit wave height. Each symbol (colour) represents a distinct airhole configuration, which provides varying degrees of hydrodynamic damping.
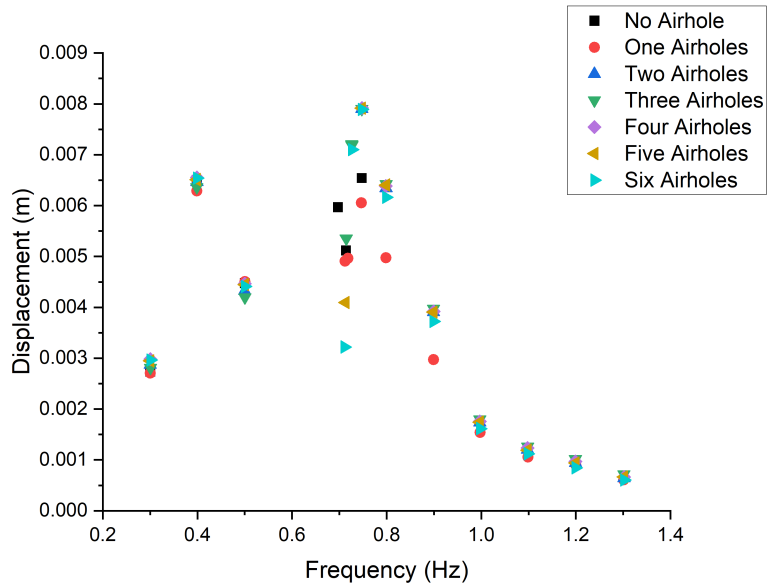
Figure 4.10: PTO piston displacement at model-scale (frequency: 0.2–1.4 Hz). Each symbol (colour) represents a distinct airhole configuration, which provides varying degrees of hydrodynamic damping.

The displacement data suggest the ZOEX concept can successfully drive the PTO and the results align well with the pitch RAO data. It also demonstrates that the influence of damping diminishes as frequency increases beyond 1 Hz, where displacements for all configurations converge. The effect of damping is most evident near the resonance peak (0.6–0.8 Hz), where configurations with more airholes (less damping) achieve greater displacement compared to those with fewer or no airholes opened (higher damping).

Due to the challenge associated with the small scale, force or pressure inside the PTO chamber is not measured. This, however, did not affect the estimation of the hydrodynamics power extracted by the fender.

The results for the fender's **full-scale velocity amplitude** when rotating about the pivot point on the supporting structure show that the similar velocity amplitudes across different damping conditions indicate the fender is underdamped. Given the fender's rotational velocity and the damping introduced by the PTO, the wave energy converter (WEC) behaves like a single-degree-of-freedom rotational system with:

- Damping coefficient c,

- Stiffness coefficient k,

- Angular displacement $\theta(t)$,

111

- Angular velocity $\dot{\theta}(t)$.

The instantaneous torque $\tau(t)$ due to both damping and stiffness can be written as:

$$\tau(t) = c\,\dot{\theta}(t) + k\,\theta(t). \tag{4.11}$$

Because power is the product of torque and angular velocity, the instantaneous power $P(t)$ is:

$$P(t) = \tau(t)\,\dot{\theta}(t) = \left(c\,\dot{\theta}(t) + k\,\theta(t)\right)\dot{\theta}(t), \tag{4.12}$$

which simplifies to:

$$P(t) = c\,\dot{\theta}(t)^2 + k\,\theta(t)\,\dot{\theta}(t). \tag{4.13}$$

The term $c\,\dot{\theta}(t)^2$ represents the *damping power*, often the primary source of energy capture in cases where c corresponds to PTO damping. The term $k\,\theta(t)\,\dot{\theta}(t)$ describes the instantaneous work exchange with the stiffness; although it can affect the instantaneous power, its net contribution over one full cycle is typically zero in an ideal spring.

An **instantaneous power** measurement can then be calculated based on model-scale data and extended to full scale through Froude number scaling. A designated interval of the resulting power profile is used to determine the mean power output.

For all the physical quantities required to calculate the instantaneous power, the damping is obtained through a free decay test, while the model-scale hydrostatic pitch stiffness can be computed by evaluating the change in buoyancy of the float during its motion, divided by the angular displacement.

Since the angular displacement is expressed in radians, for consistency with damping and velocity units, the hydrostatic pitch stiffness of the WEC (determined by the float) is given by

$$k = \frac{\rho g A \Delta h}{\Delta \theta}, \tag{4.14}$$

where k is the hydrostatic pitch stiffness, ρ is the water density, g is the gravitational acceleration , A is the instantaneous waterplane area of the float, Δh is the vertical displacement of the float along the Z-axis, and $\Delta\theta$ is the angular displacement of the float about the pivot in rad.

The mean power output is calculated by selected a roughly 20 seconds window in the middle of the test where the WEC movement was most representative and integrate throughout the time windows and then divided by the time window length. The resulting mean power output is presented in the Fig. 4.11.
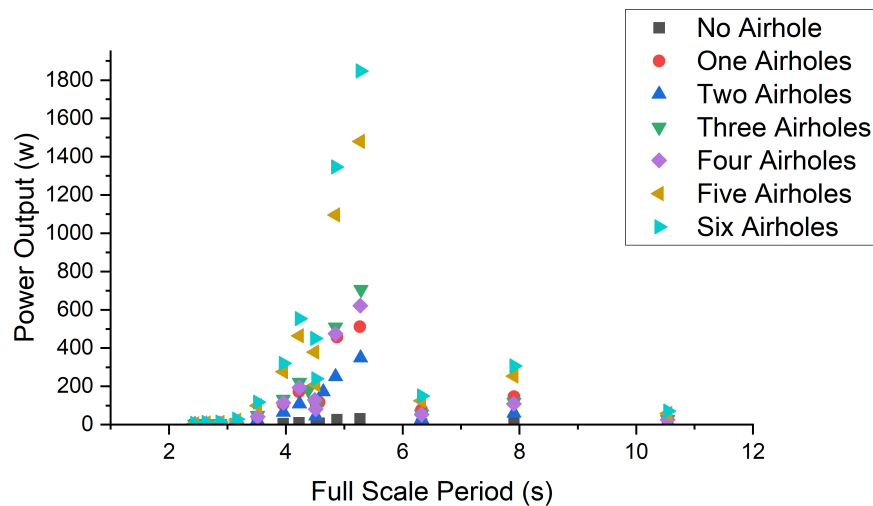
Figure 4.11: Full scale mean power captured by ZOEX, under full scale wave height of 0.35 m. Each data series corresponds to different airhole configurations, illustrating a pronounced power peak near the 5–6 s period, where resonance effects dominate.

The mean power output peaks at approximately 1.85 kW under the strongest damping configuration (six airholes) at a wave period of 5.27 s, closely aligning with the resonance region identified in RAO analyses (5-8 s). However, the peak power remains just below 2 kW, suggesting untapped energy extraction potential. Notably, power output exhibits acute sensitivity to damping adjustments: even minor changes in airhole numbers (e.g., from five to six) trigger sharp fluctuations near resonance, underscoring the delicate balance between motion suppression and energy capture.

A critical limitation arises from the damping coefficient mismatch. The model-scale damping (0.876 Nms/rad) scales to a full-scale equivalent of 2.8×10^4 Nms/rad —over 30 times lower than the designed optimal value (9.41×10^5 Nms/rad). This sub-optimal damping likely restricts energy harvesting efficiency, particularly within the resonance region, where wave excitation forces are strongest. For instance, at 5.27 s, increasing damping towards the target value could amplify power output by better synchronising the converter's response with wave frequencies. Such calibration would not only elevate peak power but also broaden the operational bandwidth, reducing dependency on narrowly tuned wave conditions.

These findings, corroborated by the power output trends in Fig. 4.11, emphasise the need for iterative damping optimisation. Future work could explore adaptive airhole systems or hybrid damping mechanisms to dynamically balance structural stability and energy yield across variable wave climates.

4.4.4 Seastate Test Results

Based on the regular wave results, damping set up with 6 air-holes open for best possible energy output result. Out of the 11 sea states tested, the most extreme case has a significant wave height of 0.75 m and a peak period of 2.56 s. The float pitch response is shown in the figure below:

Based on the pitch response and the damping coefficient calculated from the free decay test, the mean power estimated for each of the seastate is presented in Table.4.3 while Table.4.4 tabulated the maximum instantaneous power.

Table 4.3: Mean power estimated for the seastate tested (W), presented in Full scale.

H_s/T_p	3.5	4.5	6.5	7.5	8.5
0.15	20.39	48.15	37.57	27.61	20.50
0.25	–	–	142.64	–	–
0.35	–	–	332.80	–	–
0.45	–	–	635.26	–	–
0.55	–	–	937.87	–	–
0.65	–	–	1147.90	–	–
0.75	–	–	–	–	1099.85

Table 4.4: Maximum instantaneous peak power output (W) estimated for the seastate tested, presented in Full scale.

H_s/T_p	3.5	4.5	6.5	7.5	8.5
0.15	514.40	1015.53	672.15	603.46	479.71
0.25	–	–	2178.50	–	–
0.35	–	–	5133.51	–	–
0.45	–	–	9279.39	–	–
0.55	–	–	13597.16	–	–
0.65	–	–	15316.81	–	–
0.75	–	–	–	–	24497.50

4.5 Conclusion

Regarding the ZOEX wave energy converter model test

A tenth-scale ZOEX wave energy converter model was evaluated in the 3D compact wave tank at the Kelvin Hydrodynamics Laboratory of the University of Strathclyde. The goal was to assess the feasibility of the concept design by manually moving the fender and performing wave tests. A simplified PTO (Power Take-Off) mechanism was used to estimate rough power outputs.

Under a full-scale significant wave height of 0.65 m and a peak wave period of 6.5 s, the maximum mean hydrodynamic power captured by the device is estimated to be 1.15 kW. The maximum instantaneous power capture, approximately 24.5 kW, occurs at the same significant wave height but with an 8.5 s wave period.

Because the model is relatively small, certain components were simplified. For instance, low-friction bearings joining the base structure to the arm increased frictional forces that might not be present in a full-scale system. Such friction typically leads to an underestimation of power capture in full-scale operations, so actual power output may well exceed the values presented here.

Nonetheless, this proof-of-concept study confirms the viability of the ZOEX design, demonstrating its ability to rotate through angles from 0 to 180 degrees. Under a regular wave height of 0.35 m (full scale) and a 5.3 s wave period, the maximum power output is about 1.8 kW. The mean power at this regular wave condition corresponds to a capture factor of roughly 50%. At about 1.15 kW mean power in a sea state with a significant wave height of 0.65 m and a 6.5 s peak period, the hydrodynamic mean power estimate does not account for PTO efficiency. A 70% PTO efficiency would reduce the capture factor to 35%.

With further optimizations, the ZOEX concept is expected to achieve higher mean power output. For instance, adjusting the initial relative orientation between the fender and the base structure (defining the starting position of the double link arm) may influence power extraction and warrants additional study. To more accurately assess power performance, future work should focus on larger-scale models with a controlled PTO mechanism or use advanced numerical approaches such as CFD.

As of the submission of this thesis, the first 100KW prototype of has been installed in the port of Aberdeen after secured funding from the Seafood Innovation Fund.

Regarding the Two Different Motion Capture System

A direct comparison of two motion capture systems highlights the robustness of the experimental measurements. The Stereo Vision system shows close alignment with the Qualisys system, exhibiting a mean percentage difference of 0.88% and a Root Mean Square Error (RMSE) of 0.043 mm. These results confirm the Stereo Vision system's reliability, reinforcing confidence in its measured displacements and subsequent power estimates.

The Stereo Vision system, mounted on the wave tank's frame, is vulnerable to motion-induced vibration, while the Qualisys system, situated outside the tank, is largely immune to such effects. Frame rate represents another notable difference, with Stereo Vision capturing data

at 50 Hz versus the 100 Hz of the Qualisys system. This reduced rate stems from the large data volume (around 5 GB per run) and a substantial memory footprint (up to 64 GB). Because Stereo Vision records complete video frames (including background), it demands more storage and rigorous post-processing than the Qualisys system, which only tracks 3D marker positions. As a result, Stereo Vision introduces higher computational complexity and potential error during data extraction. Moreover, the Qualisys system's compact file sizes and higher frequency make it especially suitable for extended or large-scale studies, whereas Stereo Vision faces practical constraints in such settings.

Potential improvements include stabilizing the camera mounting in the Stereo Vision system to reduce vibration-induced noise, optimizing frame rates through enhanced storage management, and implementing real-time processing algorithms on GPUs. Transitioning from a record-and-post-process workflow to real-time processing would reduce overall file sizes and possibly align the frame rate more closely with Qualisys performance levels. Introducing advanced data compression and filtering could also help manage memory demands and increase accuracy.

Although the Stereo Vision system presents a cost-effective alternative, it must address certain hardware, temporal resolution, and data management limitations before fully matching the Qualisys system's reliability. Nonetheless, its strong correlation with Qualisys for displacement and power measurements underscores its promise for experimental research, particularly when improvements in mounting stability, real-time processing, and data handling are pursued. A concise side-by-side summary of the primary advantages and limitations of each motion-capture system is given in Table 4.5.

Table 4.5: Comparison of the proposed stereo-vision system and a Qualisys lab system

Aspect	Stereo-vision system	Qualisys optical motion capture
Cost	Relatively low cost.	High cost (£15k).
Markers	Marker-less.	Requires reflective markers; markers can detach or foul.
Versatility	Captures free surface and 6-DoF motion.	Dedicated to motion capture only.
Framerate	50–100 Hz ceiling.	100–1000 Hz.
Capture volume	High accuracy requires a small capture window.	Large capture volume (up to 30 m).
Data handling	Large raw-video files (∼5 GB/min).	Real-time, low-bandwidth data streams.
Environmental robustness	Sensitive to tank vibration and glare.	Cameras isolated from tank motion.

Overall, the chapter demonstrates that the stereo camera motion capture system effectively measures the WEC's motion, with less than 1% deviation from the Qualisys reference. The tests also confirm the viability of the ZOEX device at a 1:10 scale, yielding a peak power output near 1.85 kW under resonant wave conditions. Although this level of damping is suboptimal relative to full-scale targets, the results confirm the concept's promise and highlight the system's adaptability. Future refinements in PTO mechanics, system scaling, and camera hardware are recommended to enhance both measurement accuracy and energy capture efficiency.

Chapter 5

Conclusion and Outlook

This thesis has presented a detailed investigation into enhancing high-resolution water wave measurement techniques to redefine the precision, scope, and practicality of water wave measurement in laboratory settings, with a focus on addressing longstanding challenges in spatial resolution, non-intrusiveness, and real-world applicability. At its core, the work sought to bridge the gap between theoretical modelling and experimental demonstration in ocean engineering, offering a toolkit for researchers to explore wave-structure interactions with unprecedented fidelity. By developing a stereo-vision system grounded in triangulation and Direct Linear Transformation (DLT) principles, the research transcended the limitations of conventional probes—such as resistive wave gauges or single-camera methods—to deliver a robust, high-resolution framework for capturing free-surface dynamics.

5.1 Conclusion

The major contributions of this thesis can be summarised as follows, with explicit reference to how each activity satisfies the research objectives stated in Section 1.

Development and demonstration of a Novel Stereo-Vision Measurement Method: A new stereo-vision system was carefully designed, calibrated, and comprehensively validated, following a detailed literature review of existing water-wave measurement approaches, thereby fulfilling *Objective 1*. Distinct from conventional intrusive methods such as resistance-type gauges or single-point non-intrusive optical probes, the developed system employed high-grade monochrome industrial cameras fitted with advanced tilt–shift lenses. This specialised optical configuration markedly reduced glare, ensured precise focus control, and minimised image distortion, leading to consistent, high-quality capture of evolving water surfaces.

System performance was stringently assessed against a LaVision 3D calibration plate and static water-surface tests. Comparison with the established Qualisys motion-capture system recorded a mean displacement discrepancy of just 0.88 % and an RMSE of 0.043 mm, thereby meeting the metric-accuracy targets set in *Objective 2*. Robust calibration procedures involving

Direct Linear Transformation techniques further confirm the stereo-vision method as a reliable tool for precise three-dimensional wave characterisation.

In addition, the system was integrated into a desktop-scale wave flume fitted with a stepper-motor-driven plunger-type wavemaker, permitting controllable and repeatable wave generation between 0.3 Hz and 3.0 Hz. Extensive laboratory trials under controlled illumination and synchronisation conditions demonstrated operational robustness and delineated system limits, directly addressing *Objective 3*. A quasi-real-time preview mode (10 Hz processing) provided immediate experimental quality assurance.

Advanced bespoke image-processing algorithms were also devised to extract wave-surface elevations from high-speed imagery. Combined with statistical and numerical tools for frequency, amplitude, and phase analyses, these developments form a comprehensive laboratory measurement framework that eclipses existing capabilities.

Application and Rapid demonstration of Water-Wave Metamaterial Design: The measurement framework was subsequently coupled with rapid 3D-printing prototyping to evaluate metamaterial structures—such as a channelled spherical-cut design—thereby extending the research to complex wave–structure interactions and realising *Objective 4*. Experiments revealed localised wave-amplification peaks (RAO 1.8–2.0), discernible phase shifts, dispersion effects, and wave-front decelerations of up to 15 %, supplying empirical data previously unavailable for the refinement of coastal-protection and marine-energy metamaterials. Additional tests on submerged geometric forms across varied water depths, frequencies, and dimensions furnished design guidance for wave-manipulation structures.

Enhanced Motion Tracking of Wave-Energy-Converter Dynamics: Further novelty arose from adapting the stereo-vision system for motion capture of a scaled ZOEX wave-energy converter. Displacement tracking matched Qualisys reference accuracy (0.043 mm RMSE), confirming the method's suitability as a cost-effective alternative. Regular-wave trials identified an optimal six-hole damping configuration that maximised power extraction (1.85 kW, full scale) under resonant conditions, while rotation tracking up to 180° provided critical insights into survivability. These findings underscore the system's practicality and further exemplify fulfilment of *Objective 4*.

Collectively, the work meets all four objectives: framing the need for a new approach (*Objective 1*); delivering and calibrating a high-resolution stereo-vision prototype (*Objective 2*); validating its robustness in controlled laboratory conditions (*Objective 3*); and applying it to advanced metamaterial and wave-energy studies (*Objective 4*). The resultant methodology establishes a new benchmark for non-intrusive, high-fidelity water-wave measurement and

provides a robust platform for future hydrodynamic and marine-energy investigations.

5.2   Limitations of the Study

Despite its successes, the work does not resolve every challenge inherent in wave measurement. The laboratory-focused scope means that translating these findings to real-world environments (such as coastal zones with shifting illumination, turbidity, or large-scale wave actions) remains an open question. Although tilt-shift lenses and careful calibration help mitigate glare, field deployment would likely require adaptive algorithms for changing lighting and water conditions. Additionally, capturing and processing large volumes of image data places significant demands on computational resources, limiting real-time analysis without dedicated hardware. Finally, integrating the measurement system more tightly with advanced numerical models was beyond the scope of the present study; fully closing that loop would allow for dynamic feedback between experiments and simulations, further amplifying the system's utility in design and operational scenarios.

5.3   Future Research

Building upon the research outcomes presented in this thesis, several avenues for potential future research are proposed, particularly to address identified limitations and explore new opportunities arising from technological advancements and methodological refinements.

Building on the established stereo-vision methodology, future studies could pursue a closer integration with theoretical and numerical models, such as computational fluid dynamics (CFD) or potential flow theory. Dynamic integration between experimental measurements and simulations would enable a closed-loop cycle of calibration, validation, and refinement. Where each stereo-vision frame supplies a free-surface map to a data-assimilation step (e.g. an Ensemble Kalman Filter). The model nudges its boundary conditions toward the measured field, advances one time step, then compares the prediction with the next image. Persistent residuals flag camera-calibration drift, while the updated simulation provides an improved forecast, tightening both optics and numerics in real time.

By aligning precise stereo-vision data with model-driven computation, the proposed measurement system can feed back into theoretical development, enabling researchers to systematically explore non-linear wave–structure interactions, optimize wave-energy devices, and validate emerging metamaterial concepts through robust experiment–theory inter-validation. Ultimately, this approach could yield a compact, deployable digital twin system—a versatile platform adaptable to diverse applications, from marine energy innovation to metamaterial testing.

In addition to merging further with theoretical study, extending the laboratory-based stereo-vision system to real-world marine environments is also an essential part of future researches. Given the fact that the current iteration of the capturing and reconstruction hardware and software relies heavily on markers on the water surface and seeding of the water surface, non-trivia amount of alteration would required to the hardware and software implementation. Since markers and artificial seeding are impractical in open water settings, leveraging natural water surface signatures as dynamic fiducial markers becomes critical. Unlike laboratory scenarios, natural water surfaces inherently possess optical textures that facilitate direct image correlation without artificial seeding, potentially improving upon current leading methodologies, such as the Wave Acquisition Stereo System (WASS) (Benetazzo et al., 2016) by implementing more direct direct image correlation. Nevertheless, this approach opens opportunities for scalable, non-invasive oceanographic studies. A field-ready system could monitor wave energy dissipation, microplastic transport (Huang et al., 2020), or coastal erosion autonomously, bridging the gap between laboratory precision and real-world applicability. By aligning computational methods with the self-sustaining optical richness of marine environments, this approach promises both scientific rigour and practical relevance, setting a new standard for optical measurements in open water.

Further improvements in vertical resolution, depth accuracy, and spatio-temporal fidelity demand enhanced data processing strategies in both laboratory and real-world scenarios. Future research should consider refining calibration targets and methods, adopting advanced pattern projection techniques, and exploring multispectral imaging systems for significantly improved depth accuracy. Incorporating machine learning–assisted feature extraction and adaptive algorithmic stability can bolster real-time performance, particularly when handling variable environmental conditions. Furthermore, extending the stereo-vision approach to specialized applications, such as anchor design evaluations in sandy substrates, could yield considerable benefits. Adapting the stereo-camera system established in laboratory flume experiments to sand tank tests would enable precise mapping of sand displacement, morphological evolution, and sediment accumulation patterns, thereby advancing anchor design methodologies and refining the fundamental understanding of sediment–structure interactions.

By following these targeted recommendations, future research can refine the synergy between optical measurement and theoretical modelling, promote robust field deployments, and foster cutting-edge data processing solutions. Such developments stand to advance ocean engineering toward safer, more efficient, and ecologically conscious coastal and offshore infrastructure.

5.4   Concluding Remarks

By fulfilling the principal aims—designing a stereo-vision system, validating its accuracy, and demonstrating its applicability to metamaterial research and wave energy device studies—this thesis advances the state of ocean engineering measurement and has achieved the objectives established in Chapter 1. In doing so, it offers a powerful tool that unifies optical ingenuity with practical lab-scale experimentation, illuminating the subtle wave processes that are central to many marine and coastal engineering challenges. While further steps remain—particularly in large-scale, real-time, or model-integrated deployments—this work establishes a robust blueprint for measuring free-surface dynamics at high spatial and temporal resolutions. Through these innovations, it paves the way for more informed, data-rich decisions in wave research, metamaterial design, and offshore technology.

Bibliography

Y. I. Abdel-Aziz, H. M. Karara, and M. Hauck. Direct linear transformation from comparator coordinates into object space coordinates in close-range photogrammetry*. *Photogrammetric Engineering & Remote Sensing*, 81(2):103–107, 2015. doi: 10.14358/PERS.81.2.103.

A. Benetazzo, F. Bergamasco, and F. Barbariol. Stereo wave imaging from moving vessels: Practical use and applications. *Coastal Engineering*, 109:114–127, 2016.

F. Bergamasco. Wass: an open-source pipeline for 3d stereo reconstruction of ocean waves. *Coastal Engineering*, 2017.

C. Berraquero, A. Maurel, P. Petitjeans, and V. Pagneux. Experimental realization of a water-wave metamaterial shifter. *Physical Review E*, 88(5):051002, 2013.

J. Chandler, R. Wackrow, X. Sun, K. Shiono, and P. Rameshwaran. Measuring a dynamic and flooding river surface by close range digital photogrammetry. *International Archives of the Photogrammetry, Remote Sensing and Spatial Information Sciences*, 37, 2008.

L. Chatellier, S. Jarny, F. Gibouin, and L. David. A parametric piv/dic method for the measurement of free surface flows. *Experiments in Fluids*, 54:1–15, 2013.

C. S. Cox. Measurements of slopes of high-frequency wind waves. *Journal of Marine Research*, 16:199–225, 1958.

G. Dupont, S. Guenneau, O. Kimmoun, B. Molin, and S. Enoch. Cloaking a vertical cylinder via homogenization in the mild-slope equation. *Journal of Fluid Mechanics*, 796, 2016.

M. Farhat, S. Enoch, S. Guenneau, and A. Movchan. Broadband cylindrical acoustic cloak for linear surface waves in a fluid. *Physical Review Letters*, 101(13):134501, 2008.

A. Fouras, D. L. Jacono, G. J. Sheard, and K. Hourigan. Measurement of instantaneous velocity and surface topography in the wake of a cylinder at low reynolds number. *Journal of Fluids and Structures*, 24(8):1271–1277, 2008.

I. Fujita, M. Muste, and A. Kruger. Large-scale particle image velocimetry for flow analysis in hydraulic engineering applications. *Journal of Hydraulic Research*, 36(3):397–414, 1998. doi: 10.1080/00221689809498626.

G. Gomit, L. Chatellier, and L. David. Free-surface flow measurements by non-intrusive methods: a survey. *Experiments in Fluids*, 63(6):94, 2022.

P. V. Guimarães, F. Ardhuin, and M. Accensi. Stereo imaging of ocean waves for high-resolution measurements of wave characteristics. *Journal of Atmospheric and Oceanic Technology*, 37 (12):2239–2253, 2020.

L. Han, S. Chen, and H. Chen. Water wave polaritons. *Physical Review Letters*, 128(20):204501, 2022.

R. Hartley and A. Zisserman. *Multiple View Geometry in Computer Vision*. Cambridge University Press, 2 edition, 2004.

K. Hasselmann, T. Barnett, E. Bouws, H. Carlson, D. Cartwright, K. Enke, J. Ewing, H. Gienapp, D. Hasselmann, P. Kruseman, A. Meerburg, P. Muller, D. Olbers, K. Richter, W. Sell, and H. Walden. Measurements of wind-wave growth and swell decay during the joint north sea wave project (jonswap). *Deut. Hydrogr. Z.*, 8:1–95, 01 1973.

Y. Huang, Z.-M. Yuan, S.-S. Dai, and L.-B. Jia. Plastic debris in waves: An experimental study. *International Ocean and Polar Engineering Conference*, All Days, 10 2020.

Y. Huang, S. Dai, Z.-M. Yuan, and L. Jia. Rapid validation of water wave metamaterials in a desktop-scale wave measurement system. *International Journal of Fluid Engineering*, 1(1), 2024.

T. Iida and M. Kashiwagi. Small water channel network for designing wave fields in shallow water. *Journal of Fluid Mechanics*, 849:90–110, 2018.

T. Iida, A. Zareei, and M.-R. Alam. Water wave cloaking using a floating composite plate. *Journal of Fluid Mechanics*, 954:A4, 2023.

B. Jähne, J. Klinke, and S. Waas. Imaging of short ocean wind waves: a critical theoretical review. *JOSA A*, 11(8):2197–2209, 1994.

W. Keller and B. Gotwols. Two-dimensional optical measurement of wave slope. *Applied Optics*, 22(22):3476–3478, 1983.

P. A. Lange, B. Jähne, J. Tschiersch, and I. Ilmberger. Comparison between an amplitude-measuring wire and a slope-measuring laser water wave gauge. *Review of Scientific Instruments*, 53(5):651–655, 1982. doi: 10.1063/1.1137036.

J. Lawrence. Wave slope optical wave gauges. Technical report, MARINET D2.1 Report, 2012.

U. Leonhardt. Optical conformal mapping. *Science*, 312(5781):1777–1780, 2006.

C. Li, L. Xu, L. Zhu, S. Zou, Q. H. Liu, Z. Wang, and H. Chen. Concentrators for water waves. *Physical Review Letters*, 121(10):104501, 2018.

M. J. Lighthill. Waves in fluids. *Communications on Pure and Applied Mathematics*, 20(2): 267–293, 1967.

C. Marangos and R. Porter. Shallow water theory for structured bathymetry. *Proceedings of the Royal Society A*, 477(2254):20210421, 2021.

S. Masterton and C. Swan. Evaluation of wave height measurements using a resistance-type wave probe. *Ocean Engineering*, 35(8-9):939–951, 2008.

A. Maurel, J. J. Marigo, P. Cobelli, P. Petitjeans, and V. Pagneux. Revisiting the anisotropy of metamaterials for water waves. *Physical Review B*, 96(13):134310, 2017. doi: 10.1103/ PhysRevB.96.134310.

F. Moisy, M. Rabaud, and K. Salsac. A synthetic schlieren method for the measurement of the topography of a liquid interface. *Experiments in Fluids*, 46(6):1021–1036, 2009.

J. Newman. Cloaking a circular cylinder in water waves. *European Journal of Mechanics-B/Fluids*, 47:145–150, 2014.

J. Park, J. R. Youn, and Y. S. Song. Hydrodynamic metamaterial cloak for drag-free flow. *Physical Review Letters*, 123(7):074502, 2019.

J. B. Pendry, D. Schurig, and D. R. Smith. Controlling electromagnetic fields. *Science*, 312 (5781):1780–1782, 2006.

M. Pfister and C. Gisonni. Comparison of ultrasonic and resistive wave gauges for hydraulic model tests. *Flow Measurement and Instrumentation*, 36:41–47, 2014.

R. Porter. Plate arrays as a perfectly-transmitting negative-refraction metamaterial. *Wave Motion*, 100:102673, 2021.

G. Rak, M. Hočevar, S. Kolbl Repinc, L. Novak, and B. Bizjan. A review on methods for measurement of free water surface. *Sensors*, 23(4), 2023. ISSN 1424-8220. doi: 10.3390/ s23041842. URL `https://www.mdpi.com/1424-8220/23/4/1842`.

O. Reynolds. An experimental investigation of the circumstances which determine whether the motion of water shall be direct or sinuous, and of the law of resistance in parallel channels. *Philosophical Transactions of the Royal Society of London*, 174:935–982, 1883.

A. Rodriguez, A. Sanchez-Arcilla, J. Redondo, and C. Mösso. Macroturbulence measurements with electromagnetic and ultrasonic sensors: a comparison under high-turbulent flows. *Experiments in Fluids*, 27(1):31–42, 1999.

R. R. Rosales and G. C. Papanicolaou. Gravity waves in a channel with a rough bottom. *Studies in Applied Mathematics*, 68(2):89–102, 1983. doi: 10.1002/sapm198368289.

D. Schurig, J. J. Mock, B. Justice, S. A. Cummer, J. B. Pendry, A. F. Starr, and D. R. Smith. Metamaterial electromagnetic cloak at microwave frequencies. *Science*, 314(5801):977–980, 2006.

R. A. Shelby, D. R. Smith, and S. Schultz. Experimental verification of a negative index of refraction. *Science*, 292(5514):77–79, 2001.

SNAPSHOT. "what you didn't know about the tilt function on tilt-shift lenses", 2020. URL `https://snapshot.canon-asia.com/article/eng/what-you-didnt-know-about-the-tilt-function-on-tilt-shift-lenses`. Web image, licensed CC-BY-4.0.

S. M. Soloff, R. J. Adrian, and Z. C. Liu. Distortion compensation for generalized stereoscopic particle image velocimetry. *Measurement Science and Technology*, 8(12):1441–1454, 1997. doi: 10.1088/0957-0233/8/12/008.

B. Sun, C. Li, S. Yang, and H. Zhang. A simplified method and numerical simulation for wedge-shaped plunger wavemaker. *Ocean Engineering*, 241:110023, 2021. doi: https://doi.org/10.1016/j.oceaneng.2021.110023.

C. Tropea, A. L. Yarin, and J. F. Foss. *Springer handbook of experimental fluid mechanics*, volume 1. Springer, 2007.

V. Weitbrecht, G. Kühn, and G. H. Jirka. Large scale piv-measurements at the surface of shallow water flows. *Flow Measurement and Instrumentation*, 13(5):237–245, 2002. doi: https://doi.org/10.1016/S0955-5986(02)00059-6.

Z.-M. Yuan, M. Chen, L. Jia, C. Ji, and A. Incecik. Wave-riding and wave-passing by ducklings in formation swimming. *Journal of Fluid Mechanics*, 928, 2021.

Bibliography

A. Zareei and M.-R. Alam. Cloaking in shallow-water waves via nonlinear medium transformation. *Journal of Fluid Mechanics*, 778:273–287, 2015.

G. Zhang, D. Valero, D. B. Bung, and H. Chanson. On the estimation of free-surface turbulence using ultrasonic sensors. *Flow Measurement and Instrumentation*, 60:171–184, 2018. doi: https://doi.org/10.1016/j.flowmeasinst.2018.02.009.

X. Zhang and C. S. Cox. Measuring the two-dimensional structure of a wavy water surface optically: A surface gradient detector. *Experiments in Fluids*, 17:225–237, 1994.

Z. Zhang, S. Liu, Z. Luan, Z. Wang, and G. He. Invisibility concentrator for water waves. *Physics of Fluids*, 32(8):081701, 2020.

G. Zhao. *Three-dimensional wave measurement by image processing*. Phd thesis, University of Strathclyde, 2024. URL `https://strathprints.strath.ac.uk/82347/`.

S. Zou, Y. Xu, R. Zatianina, C. Li, X. Liang, L. Zhu, Y. Zhang, G. Liu, Q. H. Liu, H. Chen, et al. Broadband waveguide cloak for water waves. *Physical Review Letters*, 123(7):074501, 2019.